



## Deep learning in pore scale imaging and modeling

Ying Da Wang <sup>a</sup>, Martin J. Blunt <sup>b</sup>, Ryan T. Armstrong <sup>a</sup>, Peyman Mostaghimi <sup>a,\*</sup>

<sup>a</sup> School of Minerals and Energy Resources Engineering, University of New South Wales, Australia

<sup>b</sup> Department of Earth Science and Engineering, Imperial College London, United Kingdom



### ARTICLE INFO

#### Keywords:

Pore-scale  
Deep learning  
Permeability  
Super resolution  
Segmentation  
Reconstruction

### ABSTRACT

Pore-scale imaging and modeling has advanced greatly through the integration of Deep Learning into the workflow, from image processing to simulating physical processes. In Digital Core Analysis, a common tool in Earth Sciences, imaging the nano- and micro-scale structure of the pore space of rocks can be enhanced past hardware limitations, while identification of minerals and phases can be automated, with reduced bias and high physical accuracy. Traditional numerical methods for estimating petrophysical parameters and simulating flow and transport can be accelerated or replaced by neural networks. Techniques and common neural network architectures used in Digital Core Analysis are described with a review of recent studies to illustrate the wide range of tasks that benefit from Deep Learning. Focus is placed on the use of Convolutional Neural Networks (CNNs) for segmentation in pore-scale imaging, the use of CNNs and Generative Adversarial Networks (GANs) in image quality enhancement and generation, and the use of Artificial Neural Networks (ANNs) and CNNs for pore-scale physics modeling. Current limitations and challenges are discussed, including advances in network implementations, applications to unconventional resources, dataset acquisition and synthetic training, extrapolative potential, accuracy loss from soft computing, and the computational cost of 3D Deep Learning. Future directions of research are also discussed, focusing on the standardization of datasets and performance metrics, integrated workflow solutions, and further studies in multiphase flow predictions, such as CO<sub>2</sub> trapping. The use of Deep Learning at the pore-scale will likely continue becoming increasingly pervasive, as potential exists to improve all aspects of the data-driven workflow, with higher image quality, automated processing, and faster simulations.

### 1. Introduction

Digital Core Analysis involves imaging the pore space of rocks, analyzing them digitally, and modeling physics by numerical methods (Blunt et al., 2013; Bultreys et al., 2016). It has matured since its inception in the 1990s into a widely used suite of techniques for rapidly predicting flow behavior and rock physics in petroleum engineering, hydrogeology, as well as other applications from catalysis to drug delivery which involve porous materials. After processing and segmentation (Iassonov et al., 2009), such segmented digital images can be used as-is for compositional characterization (Fandrich et al., 2007), and/or for the analysis of fluid transport properties by numerical simulation of transport phenomena, for example single-phase flow (McClure et al., 2014; Wang et al., 2020b; Chung et al., 2019; Wang et al., 2019b; Mostaghimi et al., 2013; Chung et al., 2020a; Krakowska et al., 2016; Ferrand and Celia, 1992; Mostaghimi et al., 2016; Mostaghimi et al., 2013), particle tracking (Mostaghimi et al., 2012), reactive transport

(Liu and Mostaghimi, 2017a; Liu and Mostaghimi, 2017b; Liu et al., 2017b; Liu et al., 2018; Liu and Mostaghimi, 2017a; Mostaghimi et al., 2016), and multiphase flow (McClure et al., 2014; Wang et al., 2020b; Blunt et al., 2013; Raeini et al., 2014; Raeini et al., 2012; Yang, 2013; Ramstad et al., 2010; Pan et al., 2004). Petrophysical and flow properties such as the permeability, relative permeability, formation factor and pore size distribution can thus be calculated (Lai et al., 2018; Ren et al., 2020), which are critical parameters in phenomena involving flow within porous media, such as groundwater transport, contaminant remediation, oil recovery processes, CO<sub>2</sub> sequestration, environmental waste management (Armstrong et al., 2017; Bijeljic et al., 2011; Bijeljic et al., 2004; Gunde et al., 2010; Iglaue et al., 2011; Mostaghimi et al., 2012; Fenwick and Blunt, 1998; Hilpert and Miller, 2001; Blunt et al., 2002; Culligan et al., 2006; Mostaghimi et al., 2010; Mostaghimi et al., 2016; Blunt, 2017; Blunt et al., 2013), catalysis (Keil and Rieckmann, 1994), natural and biological membranes (Gruber et al., 2011), and medical applications (Khanafer et al., 2012).

\* Corresponding author.

E-mail addresses: [yingda.wang@unsw.edu.au](mailto:yingda.wang@unsw.edu.au) (Y.D. Wang), [m.blunt@imperial.ac.uk](mailto:m.blunt@imperial.ac.uk) (M.J. Blunt), [ryan.armstrong@unsw.edu.au](mailto:ryan.armstrong@unsw.edu.au) (R.T. Armstrong), [peyman@unsw.edu.au](mailto:peyman@unsw.edu.au) (P. Mostaghimi).

The broadening range of applications for pore-scale modeling is supported by both improvements in hardware (imaging devices and computational power), and increasingly efficient and complex models that improve domain size and the scope of physical processes that can be simulated. For example, 3D images obtained from X-ray micro-Computed Tomography ( $\mu$ CT) of a rock core sample of 1 cm in diameter typically span over  $2500 \times 2500 \times 5000$  voxels, with a resolution of a few micrometers ( $\mu\text{m}$ ) (Soulaine et al., 2016; Wang et al., 2019b). This level of detail is able to capture the pore space of sandstone rocks (for example) sufficiently for direct flow simulation to be performed in the pore space using super-computing resources (Liu et al., 2017a; Wang et al., 2019b) and/or for petrophysical properties to be estimated over a representative elementary volume (REV) using simplified models (Delerue et al., 2003; Chung et al., 2019; Chung et al., 2020a; Wang et al., 2019b; Chung et al., 2020b). These limits in imaging detail and modeling capacity will continue to increase naturally with computational performance.

Despite these advances in imaging hardware capabilities and computational power, there remain limiting factors in a wide range of cases. In terms of imaging, a trade-off between the Field of View (FOV) and resolution becomes problematic. For example, in carbonate rocks, where sub-micrometer features need to be resolved but heterogeneity exists at the centimeter-scale and beyond (Menke et al., 2018). Another example is coal, where both sample fragility and sub-micrometer fractures restrict resolution, insufficient to resolve thin fractures (Hao Chen et al., 2014). These examples highlight the demand for higher spatial resolution and FOV that what is achievable with current imaging hardware - thus a limiting factor in imaging capabilities which must trade between high resolution or wide FOV. When segmenting an image to identify pores and minerals, user-biases and the quality of the image itself are shown to dramatically affect the physical accuracy of subsequent flow modeling results (Garfi et al., 2019). In terms of modeling, the scalability of 3D simulation has fallen behind increasing imaging capabilities, as image size has outstripped the memory capacity and/or computational speed of conventional workstations (Blunt et al., 2013; Wang et al., 2019b; Wang et al., 2020b). On a workstation, direct simulation using Lattice Boltzmann Methods (LBM) or Finite Difference/Finite Volume/Finite Element Methods are typically restricted to  $300^3$  (Yang, 2013; Alpak et al., 2018; Raeini et al., 2014), while simplified methods such as Laplace Semi-Analytical Solvers (SAS) are typically capped at  $1000^3$  (Chung et al., 2019; Wang et al., 2019b; Chung et al., 2020a; Delerue et al., 2003), while Pore Network Models (PNM) can reach beyond  $2000^3$  (Rabbani et al., 2019) if domain decomposition and other distributed computing methods are used. It generally takes parallelization on clusters to reach the simulation domain available from imaging, which as stated above, is generally larger than  $2000^3$ . While it is expected that simulations on workstations will continue to increase in size from these current levels, the trend of imaging size outpacing modeling size will likely remain an issue as imaging size also grows.

It is here, at the edge of what is technically achievable with traditional pore-scale imaging and modeling, where Deep Learning can surpass these limitations. As a subset of artificial intelligence, Deep Learning is a potentially breakthrough technology in this field, as the proliferation of Deep Learning techniques in data-driven and image-based tasks is supported by improvements in GPU computing, optimization methods, and neural network architectures. These techniques have found success in augmenting and accelerating imaging and modeling beyond previous limitations for photographic and physical modeling (Goodfellow et al., 2016). Given the image-based nature of digital rock and pore-scale analysis, it can be expected that similar breakthroughs from technological limits are available. As such, this paper serves as a follow-up on previous reviews of traditional imaging and modeling techniques (Blunt et al., 2013; Bultreys et al., 2016). In the overarching scope of geo- and environmental sciences, the reader is directed to a broader review covering the larger scale (m to km) applications of Machine Learning and Deep Learning in porous media

(Tahmasebi et al., 2020).

This paper will first outline common concepts and methods in Deep Learning that are relevant to the pore-scale. Artificial Neural Networks (ANN), Convolutional Neural Networks (CNN), and Generative Adversarial Networks (GAN) are discussed with examples of usage and how they relate to the pore-scale imaging and modeling workflow. This is followed by a review of Deep Learning techniques for pore-scale imaging, which involves semantic binary/multimineral segmentation with CNNs, image quality interpolation with super resolution CNNs and GANs, and image generation/extrapolation by GANs. Then a discussion on deep learning in pore-scale modeling follows, which involves petrophysical predictions using ANNs and CNNs, and flow field modeling methods using CNNs. A depiction of the workflow and the Deep Learning tools used in Digital Core Analysis is shown in Fig. 1. From a gray-scale image obtained from a scanner, segmentation and/or image processing with super resolution (image interpolation) can be performed with CNNs, while synthetic image reconstruction (image extrapolation) can be performed with GANs from latent information or from 2D to 3D slices (or 3D to 3D volumes). Pore-scale modeling can be enhanced with ANNs and CNNs designed to predict petrophysical properties such as permeability and relative permeability, predict flow fields, or predict the distribution of fluid phases, though the authors note that as of the time of this review, work on Deep Learning-based estimation of fluid phase distributions in porous media has not yet been published.

It is important to stress that the results achieved with Deep Learning in pore-scale imaging and modeling to date represent the early stages of research and implementation. Deep Learning is itself relatively young in its implementation in practical applications, and in the context of Digital Core Analysis, difficulties and challenges remain. Further advances in network implementations, applications to unconventional resources, dataset representation and synthetic training, extrapolative potential, accuracy loss from soft computing, and the computational cost of 3D Deep Learning are some relevant major issues that are focal points in future studies. Furthermore, some examples of key areas of future studies are briefly discussed, such as integrated workflow solutions and predictions of multiphase flow (such as CO<sub>2</sub> trapping) with Deep Learning.

## 2. Deep learning concepts and techniques

Deep Learning can be thought of as an optimization (minimization) problem, in many ways analogous to the more familiar and simple root finding problem solved with 2nd order Newton-Raphson iteration. The major difference here being the number of parameters that require tuning, which typically range in the millions as opposed to just a few. Naturally, more complex techniques are required to “train” (read: optimize) a neural network to perform a specific task, primarily back propagation (Goodfellow et al., 2016) to determine derivatives, and stochastic adaptive momentum gradient descent algorithms (Goodfellow et al., 2016; Kingma and Ba, 2017) to identify local minima. The “trainable” parameters of a neural network take the form of “layers”, which are specific sets of operations performed on the data. It is important to note here that Deep Learning is a subset of Machine Learning, which is itself a subset of Artificial Intelligence. Deep Learning specifically concerns itself with the use of Neural Networks, while machine learning covers topics such as random forest, support vector machines, genetic learning, reinforcement learning, etc.

### 2.1. Artificial neural networks

ANNs are comprised of dense neural network blocks. These dense blocks are defined as containing a number  $n$  of output neurons  $y_n$ . For a number  $m$  of inputs  $x_m$ , there exists an array of weights  $w_{n,m}$  and biases  $b_m$ , and an activation function  $f$  (i.e. ReLU, see Section 2.2) that acts on each input such that  $y_n = \sum_{i=1}^m f(w_{n,i}x_i + b)$ . This output  $y_n$  is then passed as input into another dense layer, and so on in a series of “hidden

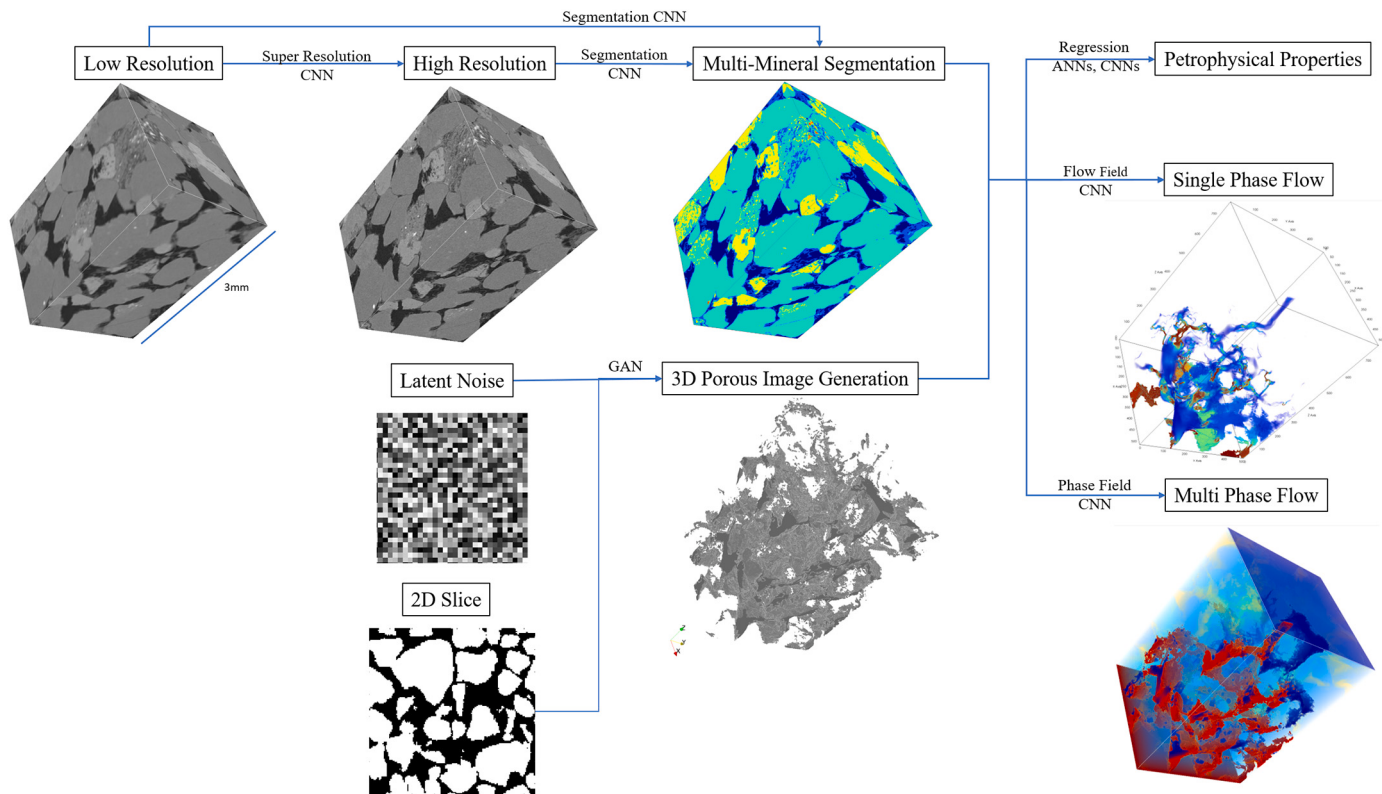


**Fig. 1.** Example illustration of the workflow in pore-scale imaging and modeling using Deep Learning. Imaging can be processed with CNNs for super resolution and segmentation or synthetically reconstructed with GANs. Modeling can be performed with CNNs and CNNs that predict petrophysical properties or predict flow and the pore-scale configuration of fluid phases.

layers". An ANN thus will take in a number  $m$  of initial input data points  $x_m$ , and pass these through several layers of dense blocks before outputting a number  $n$  of outputs  $y_n$ . As such it can be used for example, to correlate porosity, surface area, throat radius, and other parameters to another set of parameters, such as the permeability, as outlined in Section 4.1. A schematic is shown in Fig. 2.

## 2.2. Convolutional neural networks

Convolutional Neural Networks, as their name implies, utilize the convolution operation on data unlike an ANN which learns the weighted sum of all inputs. For example, in 2D image-based applications of Deep Learning, the Convolutional Neural Network consists of the following non-exhaustive list of operations.

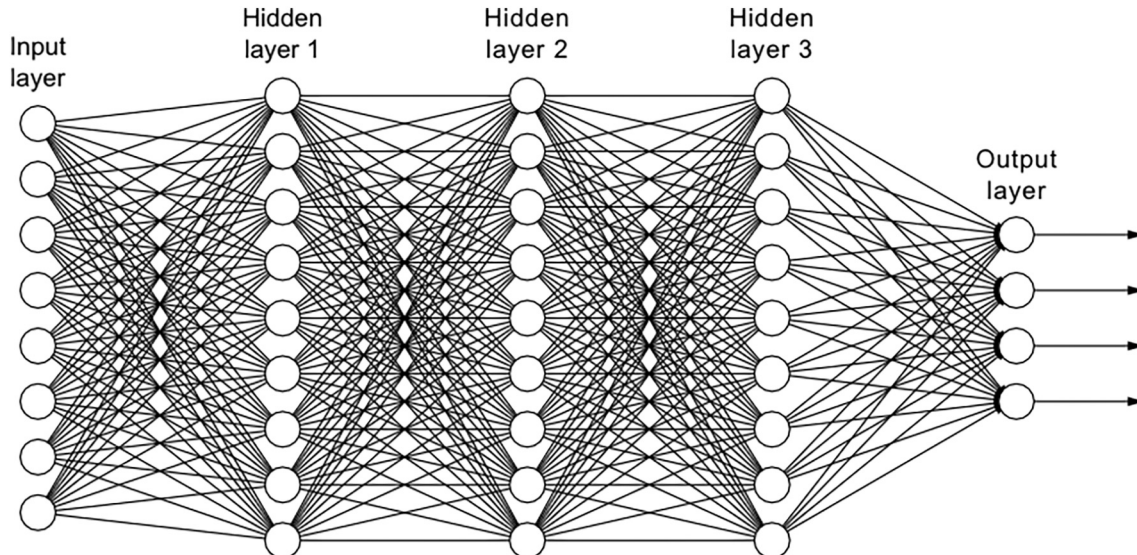


**Fig. 2.** Schematic of an ANN, comprised of a series of dense layers. Input values are transformed in this cross-weighting process to provide outputs. In this depiction, 8 inputs are cross correlated to 4 outputs.

- **Input:** the input to a 2D CNN takes the form of a batch of  $n_b$  images of shape  $(n_x, n_y, n_c)$  where  $n_c$  is the number of color channels (RGB). During the training phase of a CNN, batches of different examples (both input and output) from the available training data ( $n_b > 1$ ) are passed to the CNN over many iterations for the CNN to learn how to transform input to output. During the testing phase, single input examples are passed into the trained CNN for it to “infer” an output.
- **Convolution and Activation:** An input array  $\mathbf{X}$  of shape  $(n_b, n_x, n_y, n_c)$  is convolved against a set of convolutional filters  $\mathbf{W}$  which has a shape of  $(n_f, k_x, k_y)$  where  $n_f$  is the number of filters and  $k$  is the size of each filter (kernel size), and shifted by biases  $b_f$ . The operation sweeps across the input with a stride of  $s$ , allowing downsampling operations to be embedded within the convolution. The output  $\mathbf{Y} = \mathbf{W}[\mathbf{X}] + b_f$  is passed through a Rectified Linear Unit (ReLU) activation function that takes the form  $Y_{rectified} = \max(0, Y) - \alpha \max(0, -Y)$  where  $\alpha$  is equal to 0 (ReLU), a constant (Leaky ReLU [LReLU]), or a learnable variable (Parametric ReLU [PReLU]) (He et al., 2015a). A CNN in its most basic form consists of several of these activated convolutional layers.
- **Batch Normalization:** By calculating and normalizing an input array  $\mathbf{X}$  by the mean and standard deviation, variations in the representability of input data are reduced, allowing the network to more effectively optimize to the training data.
- **Pooling/Downsampling:** These operations are used to transform data into a smaller set, by pooling/downsampling values together and outputting the max, mean, median etc. A convolution of stride 2 or higher performs a similar task.
- **Residual Blocks:** More advanced CNN architectures use the residual block (He et al., 2015b) with skip connection. An input tensor  $\mathbf{X}_{input}$  of shape  $(n_b, n_x, n_y, n_c)$  is passed through a series (usually a pair) of activated convolutional layers (the residual block) to give an output tensor  $\mathbf{Y}_{output}$  of shape  $(n_b, n_x, n_y, n_c)$ . The input and output of the residual block are then added together in elementwise addition to give  $\mathbf{Y} = \mathbf{Y}_{output} + \mathbf{X}_{input}$ . This operation can be interpreted as a “residual” since the output  $\mathbf{Y}_{output}$  acts to incrementally change the input  $\mathbf{X}_{input}$ . These residual blocks can be repeated to form the “depth” of the model, and greatly improves the scalability of deep CNNs, since progressive residual blocks provide progressively smaller improvements to the network performance, which avoids instability issues that can arise in ordinary CNNs.

- **Upsampling/Deconvolve/Subpixel convolution:** These operations are used to transform data into a larger set, by either performing upsampling in all directions, by transposed convolution (commonly referred to as deconvolution), or by subpixel convolution.
- **Dense blocks:** analogous to the layers in an ANN, these operations are used after data from a CNN layer is first “flattened” from its multidimensional shape into 1D vectors. These ANN layers are appended to the end of a CNN to return classification labels or regression values.
- **Output**

During training, the output obtained from passing an input through the network is compared to a reference training image and the difference as measured most commonly by the mean squared error between matching pixels is used as the objective to minimize by the optimizer.

These architectures allow a diverse array of tasks to be performed by CNNs. By maintaining equal downsampling and upsampling layers, image translation is performed - useful for segmentation (see Section 3.1) and flow field prediction (see Section 4.2). By having more upsampling layers, super resolution is performed - useful for image interpolation and quality enhancement (see Section 3.2.1). By having dense layers in the end, image-based regression is performed - useful for petrophysical property prediction (see Section 4.1). A simple depiction of basic architectures is shown in Fig. 3.

### 2.3. Generative adversarial networks

Generative Adversarial Networks (GANs) (Goodfellow et al., 2014) are comprised of a pair of neural networks, a generator and a discriminator, being participants in a zero-sum game. The discriminator learns to classify inputs as either real or fake, while the generator attempts to generate fake inputs to the discriminator that are good enough for it to classify as real. In its simplest form, random noise is fed into a generator that is trained to transform the input noise into data that closely resembles the real data from the training set. The discriminator is trained alongside the generator to distinguish between the real training set data, and the generated data. As the neural networks are trained, the discriminator becomes better at identifying fake data, while the generator becomes better at generating data that fools the discriminator.

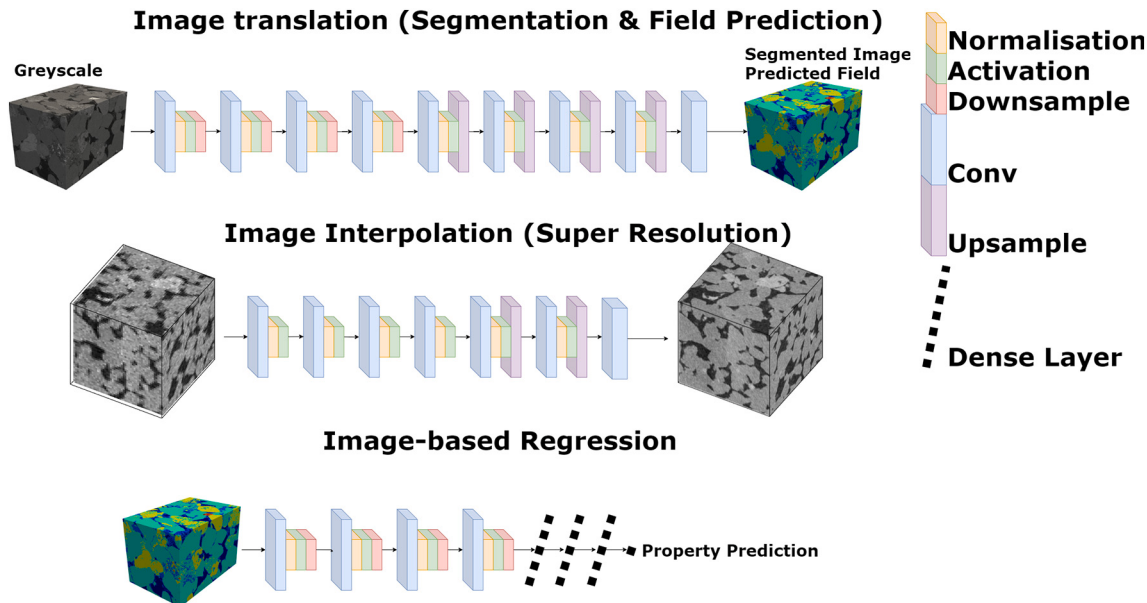


Fig. 3. Simple CNN models constructed to perform the types of tasks common in pore-scale imaging and modeling.

### 2.3.1. Generating images

Notationally, a GAN trains a CNN network  $G$  (the generator) to convert an input  $A$  to an output  $B$  and minimized with a loss function  $f_{gloss}$  as  $G \rightarrow \min(f_{gloss}(G(A), B))$ . This generator loss function  $f_{gloss}$  is partially (or fully) comprised of an adversarial loss  $f_{advloss}$  which is obtained from training another CNN network  $D$  (the discriminator) to accurately distinguish whether an input into  $D$  is real or fake:  $D \rightarrow \min(f_{dloss}(D(B), D(G(A))))$ . The adversarial loss  $f_{advloss}$  increases as the discriminator loss  $f_{dloss}$  decreases, and vice versa. As training progresses,  $G$  becomes increasingly good at creating outputs that would fool  $D$  into classifying as real (by attempting to minimize  $f_{advloss}$ ), while  $D$  becomes increasingly better at distinguishing whether the images from  $G$  are fake (by minimizing  $f_{dloss}$ ). This interplay between  $G$  and  $D$  forms the GAN, and is what allows the generation of “realistic” and statistically representative images. GANs can be used in super resolution as to regenerate texture (see Section 3.2.1) also for synthetic image generation mentioned in Section 3.2.2. A simple depiction is shown in Fig. 4.

### 2.3.2. Unpaired image translation

Cycle Consistent GANs (cycleGANs) (Zhu et al., 2017) have been used as a method for generating/translating images from one type to another without the need for said images to be paired pixelwise. They are effective in translating one image with common features into another, with the most common example being the translation of images of horses ( $X$ ) into images of zebras ( $Y$ ) and vice versa, without the need for registered images of either. On the other hand, paired image translation - a common example being segmentation (but also flow field prediction), can be performed with CNNs only (see Section 3.1), but can

also perform better with GANs (Isola et al., 2016).

Essentially, a cycleGAN consists of 2 generators  $G_{XY}$  and  $G_{YX}$  and 2 discriminators  $D_X$  and  $D_Y$ . During training, images  $X$  and  $Y$  (e.g. horses and zebras) are passed through the network in a cycle  $X \rightarrow G_{XY}(X) \rightarrow G_{YX}(G_{XY}(X))$  and  $Y \rightarrow G_{YX}(Y) \rightarrow G_{XY}(G_{YX}(Y))$  and trained to produce cycle outputs that are as close to the original input as possible:  $G_{XY} \rightarrow \min(f_{gloss}(X, G_{XY}(G_{YX}(X))))$  and  $G_{YX} \rightarrow \min(f_{gloss}(Y, G_{YX}(G_{XY}(Y))))$ . The discriminators are trained to ensure that the half-cycle outputs  $G_{XY}(X)$  and  $G_{YX}(Y)$  are featurewise consistent (as opposed to pixelwise consistent):  $D_Y \rightarrow \min(f_{dloss}(D_Y(Y), D_Y(G_{XY}(X))))$  and  $D_X \rightarrow \min(f_{dloss}(D_X(X), D_X(G_{YX}(Y))))$ . Adversarial loss (which can be thought of as  $1 - f_{dloss}$ ) is passed from discriminator to generator to couple the GAN together (Goodfellow et al., 2014). This structure and featurewise focus allow images that are unpaired (unregistered) to be transformed between each other. Briefly, the terms “featurewise”, “perceptual”, “categorical” and similar terms referencing human perception in Deep Learning refer to the outputs of CNNs that assign a numerical value to how similar inputs are in terms of morphology (i.e. edge shape, texture, gray-scale intensity, mean spatial distributions, surface area, etc) rather than relying on paired images for comparison. This unregistered capability is especially useful in learning how to convert low resolution images to high resolution images, as these images may not be directly registered (one-to-one pixel matching) to each other (see Section 3.2.1). It is also very useful for transforming between images of the same sample or rock type with different histograms/image features due to hardware imaging differences - which is a potential partial solution to Deep Learning segmentation dataset limitations (discussed in detail in Sections 3.1, 6.1, and 6.3). A simple depiction is shown in Fig. 4.

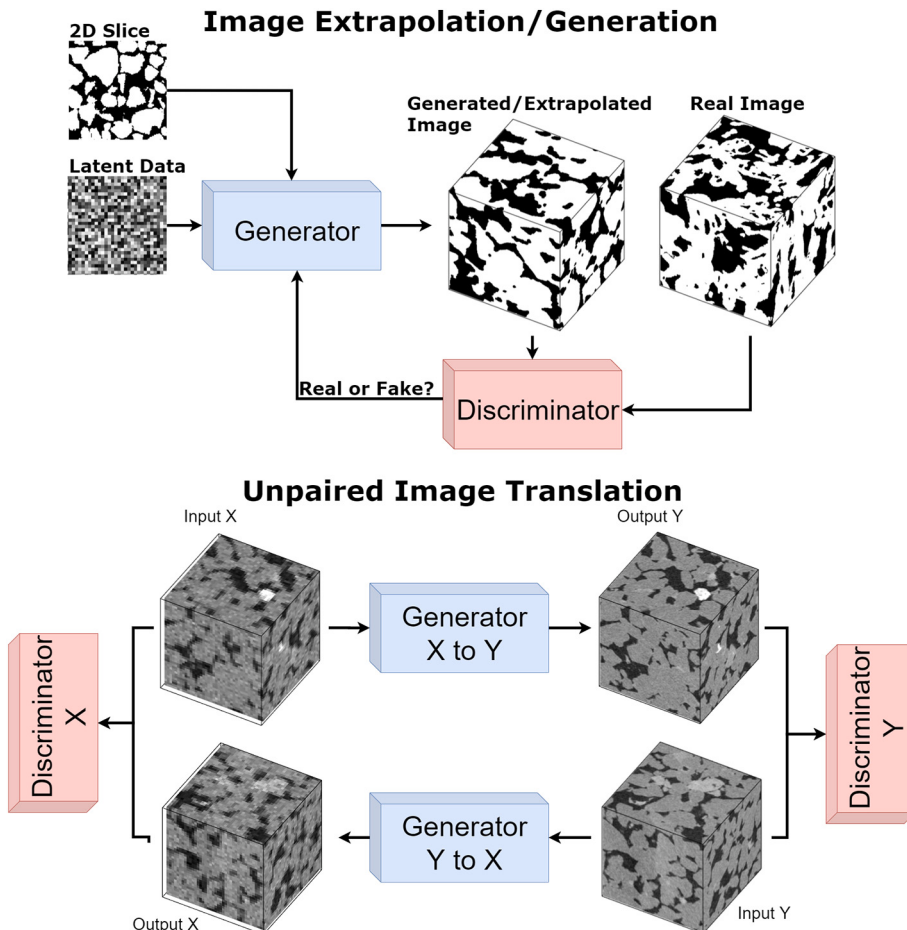


**Fig. 4.** Simple GAN models constructed to perform the types of task common in pore-scale imaging and modeling. Unpaired image translation in particular is a useful tool for cases where registered imaging data is unavailable (for example low resolution and high resolution 3D images).

### 3. Deep learning in pore-scale imaging and processing

Obtaining a 3D image of the pore space of a rock or any porous material can be done either by imaging a physical sample or by generating a synthetic sample. In both these cases, Deep Learning has contributed towards a higher degree of image detail and physical accuracy.

A digital 3D image of the pore-scale structure of a rock is typically obtained from X-ray micro-CT (Blunt et al., 2013) by reconstructing the 3D image from 2D projections taken from different angles, although any 3D imaging technique can be used. This image is then processed to better identify the phases of interest, usually the grains and pore space, through noise-reduction (Berg et al., 2016). At this point, segmentation can be performed by semi-automatic techniques requiring some degree of initial user identification (Iassonov et al., 2009; Niu et al., 2019). This ensures a degree of physical accuracy in representation, but bias/error associated with the segmentation result in high sensitivity of simulated physical parameters in the pore space (Niu et al., 2019) depending on the segmentation. These biases can affect the error in intractable ways since they are inconsistent each time, which provides unreliable information. As such the imaging quality and detail are potential limitations, and interpolation techniques can be applied to “super-resolve” the image to a higher quality.

Synthetic samples can be generated from scratch with basic algorithms and/or extrapolated from smaller data, usually already processed and segmented. In this process, physical representation and accuracy of the synthetic extrapolation must be carefully tuned, which is not always possible or accurate.

Aside from 3D micro-CT images, very fine 2D detail in the sub-micrometer range can be captured with Scanning Electron Microscopes (SEM), and 3D images can even be obtained with Focused Ion Beams (FIB-SEM) by destructively taking sequential SEM slices. The detail and sharpness achieved far surpasses the capabilities of micro-CT, but the Field of View (FOV) is naturally smaller, spanning only a few rock grains in 2D. The acquisition of SEM images plays a key role in the quality and scope of available data for Deep Learning, whereby mapping micro-CT images to SEM images provides the potential for significant improvements in the performance of CNN models, surpassing the capabilities of imaging hardware, traditional processing algorithms, and operator tuning.

In the following sections, image segmentation (binary and multi-mineral) and image quality enhancement through interpolation by super resolution and extrapolation by porous media generation are outlined and discussed in the scope of Deep Learning.

#### 3.1. Image segmentation

Automatically identifying and labeling regions in an image based on image features is a highly non-trivial digital task, but is essential for further analysis. Gray-scale images obtained by scanners (Flannery et al., 1987; Coenen et al., 2004; Blunt et al., 2013) can contain sufficient detail of the pore space of conventional rocks for segmentation (Sezgin and Sankur, 2004; Iassonov et al., 2009; Andrä et al., 2013). Image segmentation techniques range from simple thresholding (Sezgin and Sankur, 2004) to multi-step marker based methods (Iassonov et al., 2009; Andrä et al., 2013; Arganda-Carreras et al., 2017), but all such methods require a degree of user judgment and subsequent bias in the manual tuning of each step - though more advanced methods are increasingly leveraging machine learning such as WEKA segmentation (Arganda-Carreras et al., 2017). This method utilises user selected and user categorized collections of 2D image patches to then be filtered and analyzed for mean statistical characteristics. This filtered and averaged data associated with each labeled category is used to train a random forest and applied to the rest of the data. While WEKA is used in pore-scale imaging as a plugin to ImageJ and one of the first applications of AI to reach practical use in such tasks, this review focuses on Deep

Learning methods (Neural Networks) rather than Machine Learning (non-Neural Network methods). Segmentation commonly only considers the pore space and the solid grain space as distinguishable phases, treating all minerals as a singular entity with uniform physical and chemical properties, which is sufficient for single-phase nonreactive flow. Multi-mineral segmentation is a necessity for more detailed modeling, such as mixed wetting flow simulation (Akai et al., 2019), and reactive transport (Liu et al., 2018).

CNNs used for segmentation have been shown to alleviate these issues of a) the inherent bias in segmentation (Niu et al., 2019), b) the high sensitivity to physical modeling (Wang et al., 2021), and c) the increased difficulty in segmenting noisy images (Varfolomeev et al., 2019). In order to accomplish these improvements, most of these works have also focused on the use of SEM images or higher quality images to guide the learning of segmentation as well (Niu et al., 2019; Wang et al., 2021; Varfolomeev et al., 2019), as the higher sharpness and lower noise in such images allows minerals to be more accurately identified with less sensitivity to biases and physical modeling compared to  $\mu$ CT images (Fig. 5) at the cost of more limited data. Once trained on this data, the CNN also provides a consistent way of processing the data rather than semi-automatic traditional methods where each image may be processed with different parameters leading to inconsistent errors. Another critical reason is that SEM can be combined relatively easily with EDS (Energy Dispersive Spectroscopy), which yields elemental identification and thus aids mineral identification (Wang et al., 2021). Equivalent methods for micro-CT (dual energy or multi- and hyper-spectral CT) do not typically provide as broad a set of identified materials (Cnudde and Boone, 2013; Bultreys et al., 2016).

Aside from the ability for CNNs to learn from higher quality ground truth, CNNs perform well in these image-based tasks such as classification or segmentation since the convolution operation combined with the pooling operation over several layers allows the surrounding shape and texture to be accounted for when classifying (segmenting) a given voxel. This is all learned from example without needing a priori explicit description of what to look for. This is also a major difference between CNNs and WEKA/ML-based methods that instead use surrounding information by first compressing said information with user-defined filters and statistical measures.

While CNN segmentation accuracy in 2D multi-mineral (Karimpouli and Tahmasebi, 2019) and 3D binary tasks (Varfolomeev et al., 2019) show high accuracy (over 95%) as measured using pixel counting, physical measures such as connectivity and permeability tend to be highly sensitive to the segmentation result (Niu et al., 2019; Wang et al., 2021). Typical “simple” segmentations combined with standard noise filtering methods are also capable of similarly high accuracy if given clean, sharp images and a binary segmentation problem, but are sensitive to errors at the borders which does not necessarily translate in a significant volumetric error (Leu et al., 2014). Scoring the quality of a segmentation is therefore also an important factor, and these scores could potentially also serve as objective functions for the training (Taha and Hanbury, 2015). One example may be weighing pixelwise accuracy with distance to the ground truth border.

The dataset remains an important aspect in CNN segmentation, as the underlying ground truth must be accurately segmented to generate a reasonable CNN prediction. Various techniques are used for this purpose, including manual segmentation (Varfolomeev et al., 2019), manual segmentation + stochastic generation (Karimpouli and Tahmasebi, 2019), direct SEM-micro-CT registration (Niu et al., 2019), and indirect QEMSCAN-micro-CT registration (Wang et al., 2021). The network implementation then dictates performance, whereby an evolution in segmentation CNN architectures has resulted in significant improvements in accuracy over the original proposed architecture (Wang et al., 2021).

The task of segmentation similarly uses some key reference designs. All studies in segmentation thus far have been with CNN generators, so notationally, a segmentation CNN  $G_{seg}$  will take input images A and

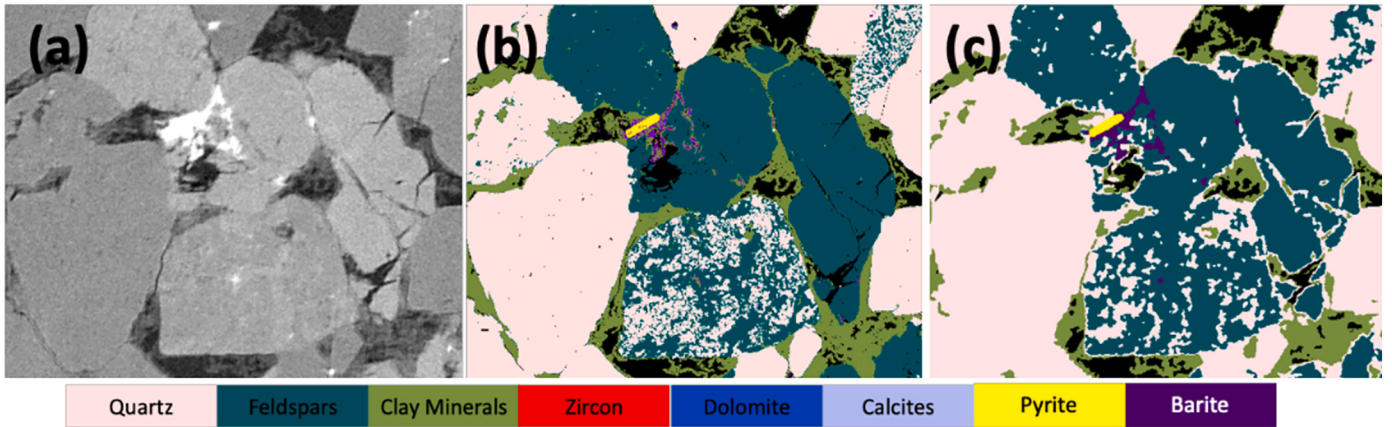


**Fig. 5.** Example of the differences in image quality of a multi-mineral segmentation between a)  $\mu$ CT gray-scale image; b) segmentation from an SEM image; and c) segmentation from a  $\mu$ CT image.

transform them into segmented images  $B$ , and is trained by minimizing the segmentation error:  $G_{\text{seg}} \rightarrow \min(f_{\text{gloss}}(B, G_{\text{seg}}(A)))$ . Specifically, the older SegNet (Badrinarayanan et al., 2015) and newer U-Net (Ronneberger et al., 2015) (Fig. 6). These two networks are used with minor to moderate modifications in the studies presented ahead, and are both designed with the idea of auto-encoder-decoder networks, where one half converts the input data into an encoded space, and the other half of the network decodes it. One point to note is that in the reviewed publications in the following sections on segmentation, sandstone samples are predominant, which tend to possess some relatively clear differences in gray-scale (pore, some clay, quartz, pyrite, etc) such that some minerals and phases can be feasibly segmented by a traditional methods. For these types of mineral/phase, the advantages of using machine learning methods becomes incremental, but there are clear benefits relating to the ease of integrating SEM imaging for high accuracy reduced-biased segmentation (Niu et al., 2019; Wang et al., 2021), which have been shown to outperform traditional watershed segmentation even on relatively simple and intensity-based task of pore-grain binary segmentation (Ar Rushood et al., 2020).

### 3.1.1. Binary segmentation

Binary segmentation involves identifying only the pores and grains within the voxels of a pore-scale image, and this task is well suited for CNNs. A study (Varfolomeev et al., 2019) testing the 2D and 3D segmentation of noisy reconstructed micro-CT images of various sandstones was performed by mapping a dataset of noisy low quality gray-scale reconstructions with binary segmentations obtained from manually segmenting cleaner, higher quality counterparts. Training the progenitor SegNet (Badrinarayanan et al., 2015) and the more modern U-Net

(Ronneberger et al., 2015; Ar Rushood et al., 2020) on this data resulted in a higher accuracy achieved by these CNNs compared to manually segmenting the lower quality images. Accuracy in the range of 80–95% was achieved with SegNet, and accuracy in the range of 90–98% was achieved with U-Net in 2D and 3D implementations, depending on the dataset.

This compared favorably to manual segmentation accuracy over the noisy data achieved by humans, which was impossible for most samples tested, and ranged anywhere from 60% to 95% for the samples that were visually possible. It was noted that segmentation error by CNNs (and humans) occurs predominantly in the microporous regions of rock images, and that the physical accuracy of such segmentation remains uncertain (Fig. 7).

### 3.1.2. Multi-mineral segmentation

Multi-mineral segmentation is significantly more difficult to perform manually, as the gray-levels of some minerals within the solid phase are effectively indiscernible by human vision in a reliable manner. As such, one of the first implementations of segmentation CNNs in Digital Core Analysis was to perform multi-mineral segmentation using the progenitor SegNet architecture (Badrinarayanan et al., 2015). Using a limited number of sandstone images, segmented manually by consideration of both intensity differences (where available) and textural differences, and correcting each pixel error incurred by automatic segmentation, a larger dataset is then generated by a stochastic algorithm (Kamrava et al., 2019a). With this dataset, a basic analysis of pixelwise accuracy was performed, with SegNet achieving around 95% accuracy for the validation/test datasets. Extra emphasis was placed on the accuracy achieved by each individual mineral phase, indicating that sparsely

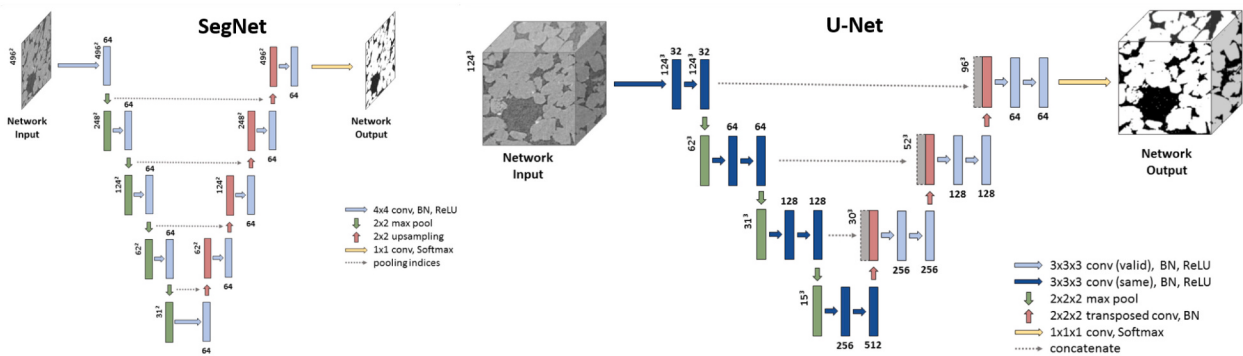


**Fig. 6.** Figure showing the SegNet and U-Net architectures, widely used and modified in segmentation applications. U-Net has generally supplanted SegNet in use, specifically its architecture design with concatenations between the encoder and decoder blocks. Reprinted with permission (Varfolomeev et al., 2019).

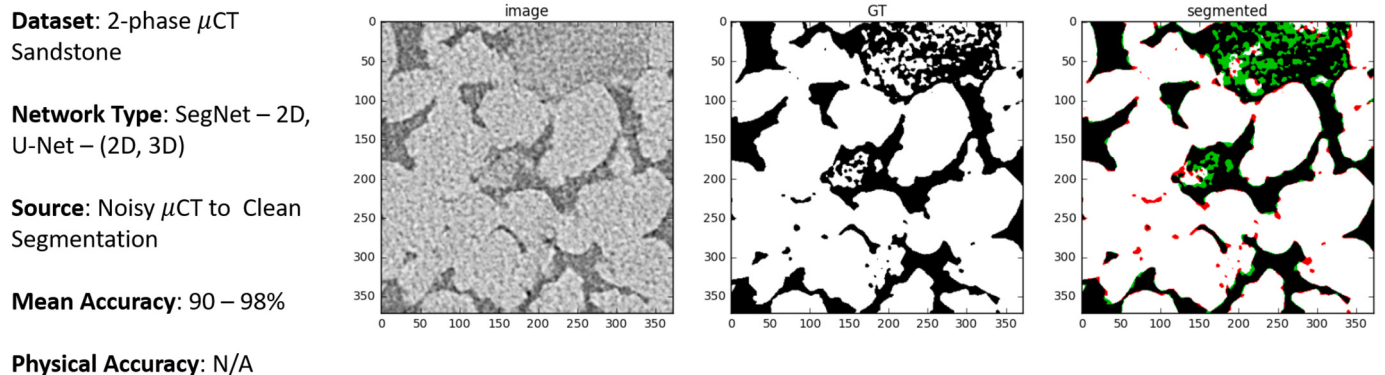


**Fig. 7.** Figure showing the input noisy image, and the resulting best segmentation obtained with a U-Net architecture. Green and red are respectively, false black and false white, showing that the U-Net is unable to recover the segmentation in such difficult regions. Reprinted with permission (Varfolomeev et al., 2019). (For interpretation of the references to color in this figure legend, the reader is referred to the web version of this article.)

occurring phases were inaccurately segmented by the network used, with as low as 60% accuracy in some cases. Visual comparison with automatically segmented images showed that the CNN performed favorably (Fig. 8), as it was trained on a dataset derived from a more careful segmentation approach.

The idea of training segmentation CNNs with data from different sources to maximize accuracy continues with extending this idea into the realm of SEM images (Niu et al., 2019). Training was performed with LeNet-5 (LeCun et al., 1989) on a dataset mapping gray-scale micro-CT images of Mt. Simon sandstone to 3 phase segmentations (pore, high density mineral, low density mineral) obtained by watershed segmentation on sharp SEM images (Fig. 9). Physical accuracy of the CNN segmentation was obtained in 3D images constructed slice-by-slice, with measurements of permeability and pore size distribution. In particular, since segmentation sensitivity (as measured by permeability) was found to be much lower in SEM images compared to micro-CT images, resulting CNN segmentation results showed similar insensitivity to segmentation threshold when trained on the gray-scale micro-CT - segmented SEM dataset compared to segmentation sensitivity when applying watershed segmentation to the  $\mu$ CT image. This reduction in user-bias is evidently achieved through the mapping of low quality gray-scale images to segmentations of higher quality data.

Extending the idea of SEM-based datasets and the importance of

physical accuracy further, a study measuring the physical accuracy achievable by different CNN networks was performed on multi-mineral QEMSCAN segmented  $\mu$ CT images of Mt. Simon Sandstone (Wang et al., 2021). The results showed that pixelwise accuracy poorly correlates with physical accuracy as measured by topological analysis (Euler number) and single/two-phase flow simulation (Fig. 10). SegNet, ResNet, U-Net, and a custom U-ResNet formulation were trained for 2D and 3D cases in 10 configurations over the dataset, and a high voxelwise accuracy (over 99%) was achieved for U-Net and U-ResNet configurations in 2D and 3D. Downstream analysis of the topology of each segmented phase, and the absolute permeability and multiphase flow modeled with direct simulation in single and mixed wetting cases showed high variance and uncertainty, with models that achieved 95% + in voxelwise accuracy possessing permeabilities and connectivity that were in error by orders of magnitude. The 3D implementation of U-ResNet outperformed all other tested models in voxelwise and physical accuracy measures.

It is clear that firstly, segmentation networks should be trained with a micro-CT - SEM segmentation mapping to reduce bias associated with the generation of training data. While this appears to be the most reliable and accurate method of obtaining ground truth, it is also very labor intensive, prone to registration errors, and therefore data set sizes are limited. Secondly, the preservation of topological accuracy and

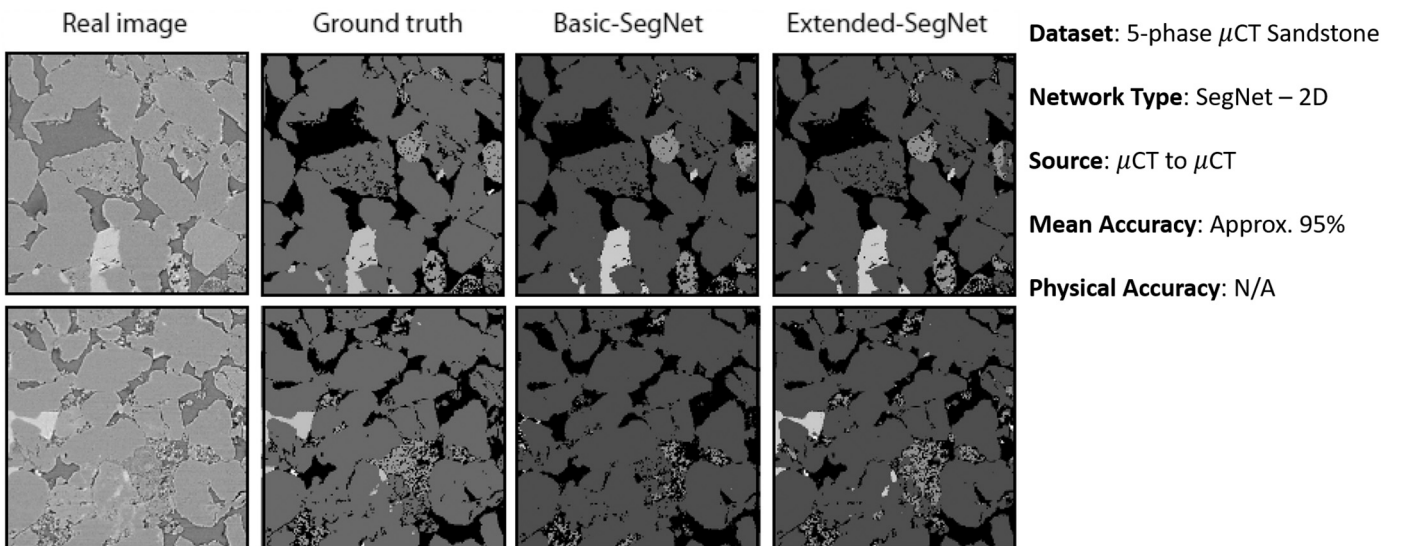
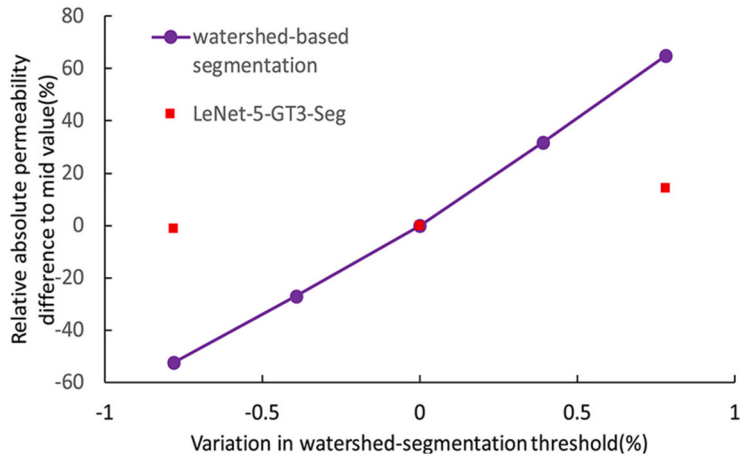
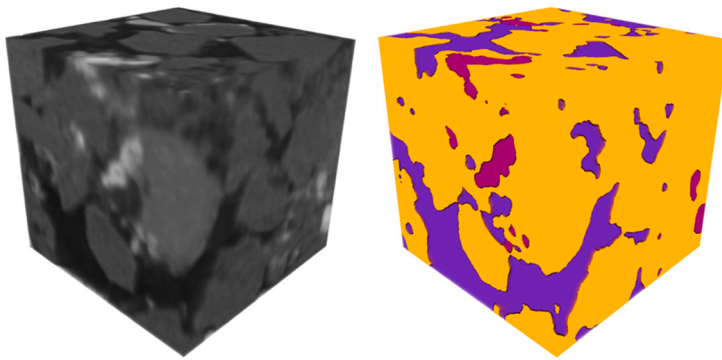


**Fig. 8.** Figure showing the results obtained from multi-mineral segmentation using a SegNet implementation. Visually, segmentation by SegNet is consistent with the ground truth (95% pixel accuracy), and no further analysis was made in this case. Reprinted with permission (Kamrava et al., 2019a).



**Dataset:** 3-phase  $\mu$ CT Sandstone

**Network Type:** Le-Net – 2D

**Source:**  $\mu$ CT to SEM

**Mean Accuracy:** Approx. 95%

**Physical Accuracy:** Permeability

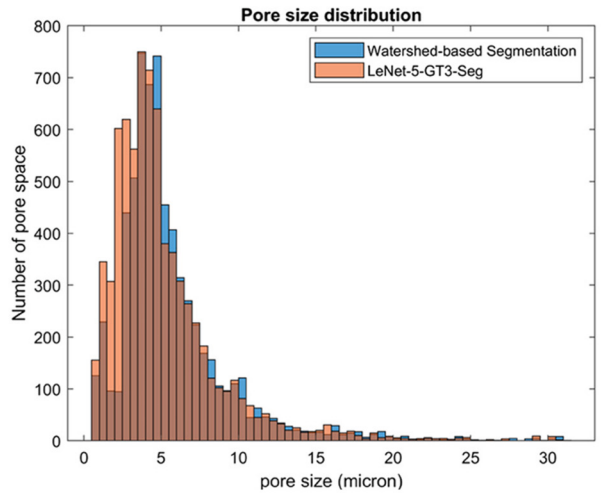


**Fig. 9.** Figure showing three-phase segmentation using a Le-Net implementation, trained on SEM-segmented images. Permeability results obtained on CNN results trained with different segmentation parameters shows minimal sensitivity, since the SEM images are much sharper compared to  $\mu$ CT images. Reprinted with permission (Niu et al., 2019).

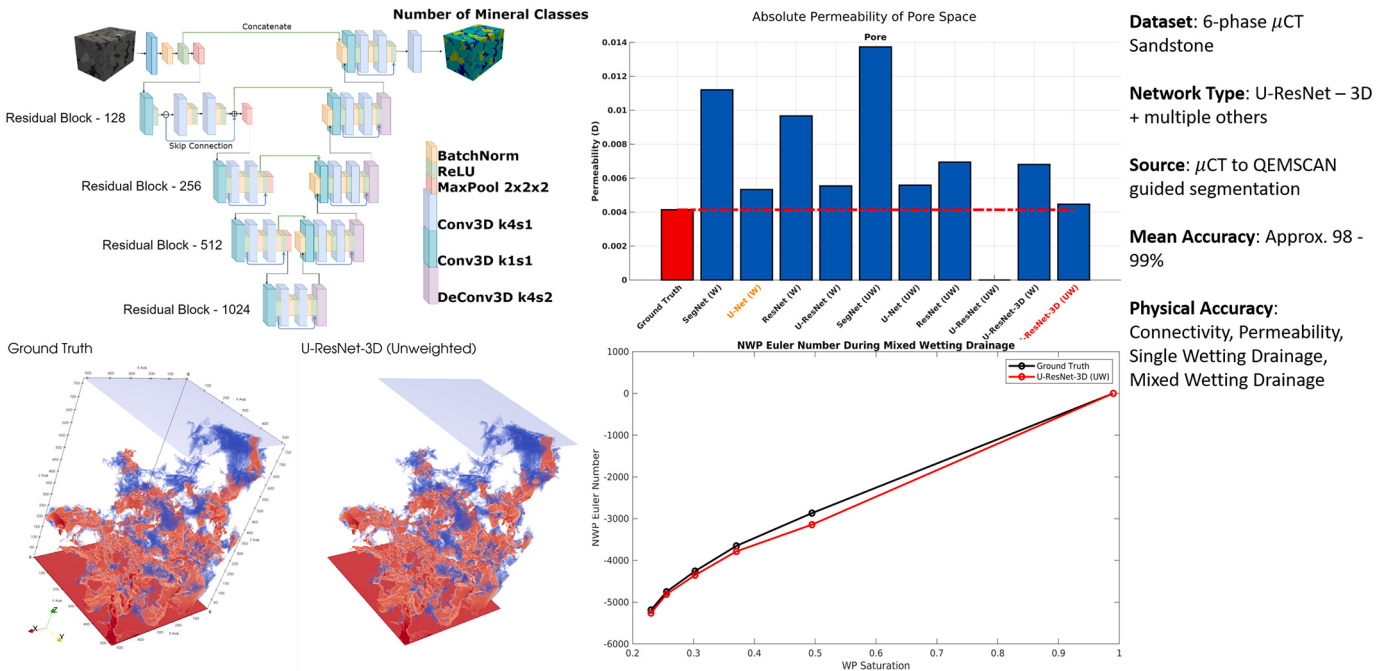


**Fig. 10.** Figures showing the U-ResNet implementation (top left), permeability for segmentation results from a variety of networks (top right), visual comparison of multiphase flow profiles through segmentation results (bottom left), and connectivity during two-phase drainage for U-ResNet vs ground truth. Reprinted with permission (Wang et al., 2021).

petrophysical accuracy should be equally prioritized with pixel/voxel-wise accuracy since network architectures achieving a high accuracy do not necessarily segment a physically accurate result. Much like in biomedical imaging research, the most widely used and accurate network designs are the U-Net and U-ResNet (Wang et al., 2021) variants (there is no consensus on U-ResNet design (Ibtehaz and Rahman, 2020)), and the use of GANs (Isola et al., 2016) may further improve segmentation accuracy. Issues that impede the practical application of CNN segmentation in pore-scale imaging are the availability of training data, and the flexibility of trained CNNs to work well on external samples, which are discussed in the next few paragraphs, as well as in Sections 5 and 6. It is also noteworthy to consider that most research on CNNs for pore-scale image segmentation is performed with 2D CNNs, while 3D studies (Wang et al., 2021) indicate a slight improvement in resulting accuracy. The use of 3D CNNs adds a richer set of information to infer the segmented value of voxels, but are more resource intensive and scale poorly (see Section 6.5).

Thus a major issue that plagues segmentation CNNs in digital rock analysis is the lack of available data over a broad range of samples, and a lack of a benchmark dataset. It is problematic that these studies in segmentation suffer from the use of disparate datasets, making the drawing of conclusions between the results achieved by different studies much harder. For example, physical accuracy measured when comparing CNN segmentation and manual segmentation in the LeNet-5 study (Niu et al., 2019) showed a favorable match, while the U-ResNet study (Wang et al., 2021) showed more variable results. This can be attributed to the use of different training datasets and different objectives in each study, with the LeNet-5 comparing SEM trained CNN segmentations with manual micro-CT segmentation tuned to match the CNN result for the purpose of user-bias sensitivity analysis, while the U-ResNet study compared network performance directly between CNN output and ground truth.

A comprehensive dataset of binary segmentations of digital rocks should be possible to compile without major difficulty using the publicly available binary segmentation data available in the Digital Rocks Portal (Esteva and Hanlon, 2015). This would follow in the same manner as the DeepRock-SR dataset (Wang et al., 2019c), which is a synthetic super resolution dataset compiled from the same source. On the other hand, a similarly comprehensive collection of multi-mineral segmented digital rocks would be a very difficult challenge to compile (though not impossible), leading to the usefulness of stochastic generation algorithms such as the one used for 2D multi-mineral segmentation of sandstone images (Karimouli and Tahmasebi, 2019). An issue with this is that the use of stochastic (and even simulated) images as input represents a bias in itself as the CNN will only learn to identify features it was trained on. Furthermore, the major focus of segmentations with CNNs has been on accurately segmenting lower quality images by training the CNN with segmented realizations from higher quality images (more projections, SEM images, QEMSCAN images, etc.), a task that would otherwise be impossible. This again is limited by data availability.

Approaches to reduce reliance on broad datasets would be to use CycleGANs with synthetic/simulated segmented images or as domain transfer (Ihle et al., 2019). Domain transfer would facilitate more accurate extrapolation of trained CNNs on unseen data images at different conditions. For instance, a CNN trained to perform multi-mineral segmentation of sandstone rocks may have been trained on one particular sandstone image and a set of QEMSCAN slices or synthetic representations, which would limit the accuracy of such a CNN if it attempted to segment a sandstone image obtained under different imaging conditions (the intensity and texture values would shift). A CycleGAN can be trained to perform domain transfer on this new image to shift its image characteristics to the manifold that the original sandstone image used for training exists on, improving extrapolative accuracy. This can also be used in conjunction with simulated micro-CT images to generate a realistic ground truth (Dhaene et al., 2015) specific to their problem.

### 3.2. Image quality enhancement

While segmentation on micro-CT images can be performed with reasonable accuracy for petrophysical analysis (Iassonov et al., 2009) to obtain fine detail and a more representative image of a porous sample for flow simulation or otherwise, higher-resolution micro-images may be required if the features of interest such as grain boundaries are smaller than hardware capabilities. In the typical case of Bentheimer sandstone pore-scale imaging, a resolution in the 5–10 μm range can resolve the quartz grains, but not the clay minerals, which require <2 μm. In other cases such as carbonates, coals, and even just sandstones with a different grain size/clay distribution, these resolution ranges can vary by an order of magnitude (Wang et al., 2020a). It is furthermore important here to explicitly distinguish between the terms “resolution” and “voxel size”, which is typically (and erroneously) used interchangeably in pore-scale research. The voxel size of a scan is not the same as its nominal resolution: a scan can have a small voxel size, but suffer from significant image artefacts that one would like to reduce with filters. Micro-CT images tend to have edge boundaries that blur over 3–5 voxels, which implies that the “resolvable” detail is lower than what the voxel size would suggest (Ketcham and Carlson, 2001).

However, these high resolution images typically have a small FOV leading to nonrepresentative results (Li et al., 2017), or are entirely outside the hardware capabilities of available scanners. For use in flow simulation (Jiang et al., 2013; Jiang et al., 2013; Schlüter et al., 2014) and other numerical methods (Yi et al., 2017), an imaged sample should be sufficiently resolved to capture pore space features and connectivity while also spanning a wide enough FOV to represent bulk rock properties to capture the heterogeneity of the sample (Li et al., 2017). In Digital Core Analysis, this is challenging for certain cases of more unconventional rocks such as carbonates that can have a significant portion of the pore space unresolvable (typically a double digit percentage) under the resolution of the imaging device (Bultreys et al., 2015) if the sample is scanned using the wrong settings, or coal samples with significant micro-scale fractures (Hao Chen et al., 2014). Thus the scanning device hardware and the physical characteristics of the sample itself are limiting factors in capturing high resolution digital rock images, with trade-offs between resolution and FOV. To have an image with high resolution and large field of view, it is possible to apply super resolution algorithms on low resolution data (Fig. 11) as a form of image interpolation.

Aside from obtaining a 3D pore-scale image with hardware and interpolating to obtain high resolution-high FOV images, statistical methods can be used to synthetically reconstruct 3D images intended to be physically similar to their real counter parts - a form of image generation or extrapolation. These methods serve to aid in cases where a wider distribution of examples of the same rock type are required, which is useful in assessing variation in geometry and mineralogy (Mosser et al., 2017a). One note to make regarding synthetic reconstruction is that generating statistically identical samples does not necessarily increase representativity, as there is no guarantee that the natural pore space variability is captured by stochastic reconstruction.

In this section, studies and applications of super resolution as an image interpolation technique, and studies and applications of GANs as an image generation/extrapolation technique are outlined and discussed.

#### 3.2.1. Image interpolation

Interpolating extra pixels/voxels from a low resolution (LR) image can be performed using simple traditional techniques such as nearest neighbor, linear, bicubic interpolation etc. These simple methods are superseded by “super resolution” techniques, which in the scope of Deep Learning, are known as Super Resolution using Convolutional Neural Networks (SRCNNs). These SRCNNs have been applied successfully to micro-CT images of rocks in a number of cases, including some examples with joint noise removal and deblurring (Wang et al., 2019a; Wang

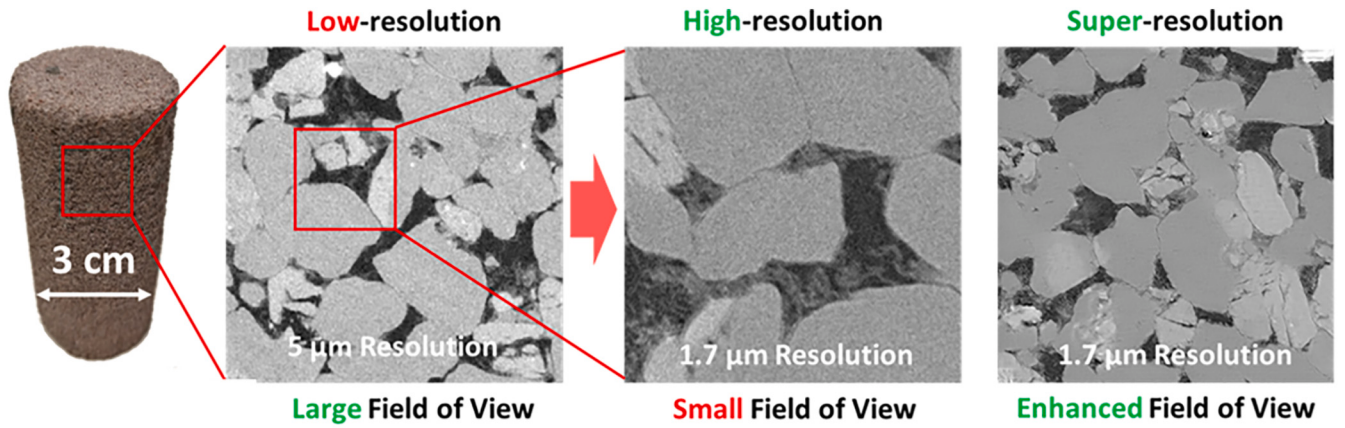


**Fig. 11.** Example of the resolution vs field of view trade-off, and how super resolution can potentially overcome this limitation.

et al., 2020a; Niu et al., 2020), and tend to perform significantly better at recovering edge detail and sharpness - critical in reducing sensitivity to user-bias in segmentation as outlined in the previous section. Advances in the implementation of SRCNNs for pore-scale applications have mirrored the wider scope of research into SRCNNs for photographic use-cases (Dong et al., 2016a; Lim et al., 2017). Since then, SRCNNs have further evolved to Super Resolution Generative Adversarial Networks (SRGANs) to address limitations in texture regeneration (Ledig et al., 2017), and Super Resolution Cyclical Generative Adversarial Networks (SRCycleGANs) to address limitations in synthetic downsampling datasets (You et al., 2018; Zhu et al., 2017). This section will outline the advancements in SRCNNs, their use and performance/limitations in Digital Core Analysis, and recent advances in network architectures that resulted in the implementation of SRGANs and SRCycleGANs in Digital Core Analysis.

**Edge Recovery:** The recovery of edge detail and image features spanning over 3–5 voxels in size from low resolution images is most effectively performed by SRCNNs, which began initially as a network that applied activated convolutional layers (Dong et al., 2016a) to a bicubically upscaled (BC) image to recover the High Resolution (HR) details on a direct mapping. SRCNNs take the form of a series of activated convolutional layers  $G_{SRCNN}$  that take an input image bicubically upscaled such that  $\text{size}(BC) = \text{size}(HR)$ . The network learns to recover the residual difference  $R_{CNN} = G_{SRCNN}(BC)$  between the HR and BC images:  $R_{Real} = |HR - BC|$ , and is trained by minimizing this difference:  $G_{SRCNN} \rightarrow \min(f_{gloss}(R_{Real}, R_{CNN}))$ . The output Super Resolution (SR) image is obtained by adding this residual to the BC image:  $SR = BC + R_{CNN}$ . The lack of skip connections in the SRCNN-type network necessitates this type of residual learning due to the reduction of performance and stability of deep networks past a certain point (see Section 2.2). This problem has largely been addressed by the use of EDSR-type networks, which employ the ResNet skip connection. This allows stable and improved scaling between performance and network depth.

The EDSR-type network is a type of integrated LR to HR network that does not require upsampling as a processing step, as the need for a fully sized input image increases computational cost. The network  $G_{EDSR}$  directly learns to produce an SR image from an LR input:  $SR = G_{EDSR}(LR)$ , and is trained by direct minimization of the SR and HR difference:  $G_{EDSR} \rightarrow \min(f_{gloss}(SR, HR))$ . Deconvolutional layers at the end of the network (Dong et al., 2016b) have been replaced by subpixel convolution to reduce checkerboard artefacts (Shi et al., 2016; Odena et al., 2016). The skip connection (see Section 2.2) that adds outputs from shallow layers to deeper layers to preserve important shallow feature sets and improve gradient scaling (Kim et al., 2016) has been common practice since its inception with ResNet (He et al., 2015b). Batch normalization (Ledig et al., 2017), has been empirically observed to reduce the accuracy of SRCNN methods (Lim et al., 2017), and are no

longer present in more recent formulations (Yu et al., 2018). The L1 (Mean Absolute Error) loss across the image (Zhu et al., 2017) has been found to be more robust against outlying features and improves convergence rates compared to the L2 (Mean Squared Error). One of the most popular architectures resulting from this development is the Enhanced Deep Super Resolution (EDSR) network (Lim et al., 2017), shown in Fig. 12, which forms the current baseline of performance for SRCNNs (Zhang et al., 2020). An advancement of the EDSR network has been gaining popularity, known as the Residual-in-Residual Dense Block (RRDB) (Wang et al., 2018), though the underlying concepts in its design are based on EDSR. Henceforth, the term “SRCNN” can refer to either the general technique of using CNNs for super resolution, or to the progenitor network architecture (Dong et al., 2016a).

SRCNN methods have been applied in 2D and 3D, both in its simple initial form and its more modern EDSR incarnation, to enhance the resolution of micro-CT images of rocks. In the task of image quality enhancement (noise/blur reduction and super resolution), a common measure of accuracy is the Peak Signal to Noise Ratio (PSNR), which is a measurement of pixel accuracy between a generated image and its ground truth. It scales logarithmically to the Mean Squared Error such that a PSNR of 10 dB is 0.1 MSE error, 20 dB is 0.01 MSE, and so on. Analogous to sound level measurement, a gain of 3 dB represents a 2× relative reduction in MSE, 6 dB is 4×, and 10 dB is 10×. The PSNR is calculated using the HR and SR image pixel value range  $I$  ([0, 255] for int8 images) and the pixel/voxelwise MSE:

$$\text{PSNR} = 10 \log_{10} \frac{I^2}{\text{MSE}} \quad (1)$$

In 2D, a 20 layer SRCNN-type network (see Fig. 12) has been successfully implemented on stochastically generated image slices of shale samples (Kamrava et al., 2019a). The scale factor was variable, one of the advantages of the SRCNN-type network, and the network was trained to predict the difference map between an input BC image, and its HR counterpart. Resulting SR images showed an improvement in pixel accuracy of 0.28 dB as measured by the PSNR. Comparisons of physical accuracy through morphological analysis showed a porosity deviation of 0.11% between SR and HR compared to 1.34% between BC and HR, and a near perfect match between SR and HR when comparing Multi-Point Connectivity (MPC) and autocorrelation functions for a sample result. A visual comparison, and plot of MPC is shown in Fig. 13.

Also in 2D, EDSR-type networks (see Fig. 12) of varying configurations have been trained and tested on sandstone and carbonate samples (Wang et al., 2019a). The scale factor in these tests was set to 4×, and the dataset of Bentheimer sandstone and Estallades carbonate (Wang et al., 2019d) was used to train 4 different networks in 14 configurations. Models developed with an “end-to-end” architecture (Wang et al., 2016), known to be superior to the original SRCNN method, including

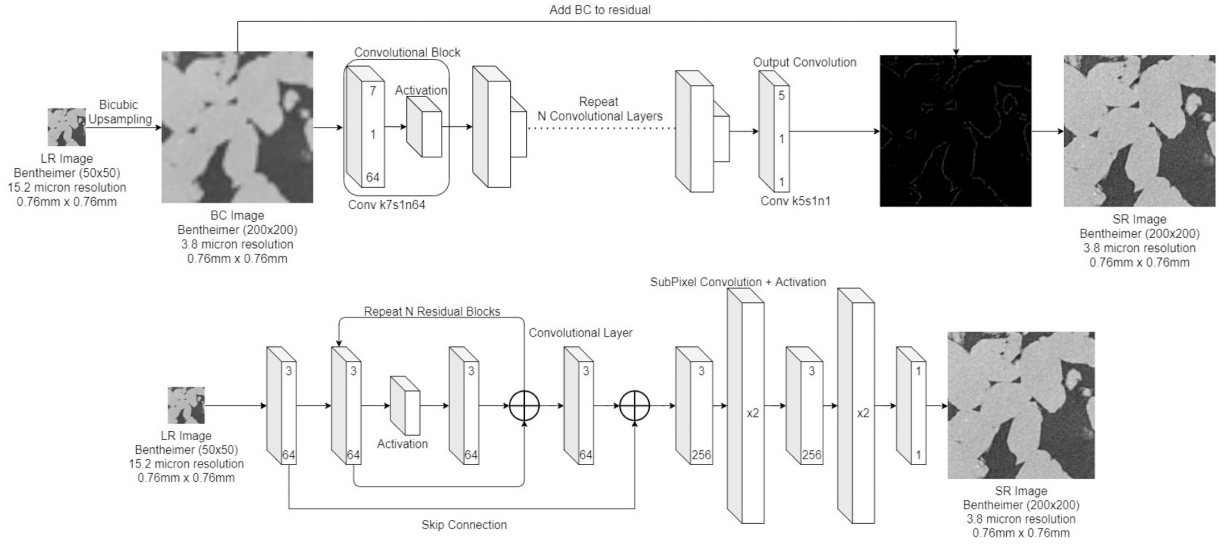


**Fig. 12.** Top: Example architecture of the original Super Resolution CNN (SRCNN), used in some studies (Kamrava et al., 2019a; Wang et al., 2019f). Bottom: Example of the Enhanced Deep Super Resolution (EDSR) architecture, used in some other studies (Wang et al., 2019a; Wang et al., 2020a; Chen et al., 2020; Niu et al., 2020). SRCNN requires first obtaining the bicubic upsample of the low resolution (LR) image, followed by a series of activated convolutions to obtain the residual difference between high resolution (HR) and bicubic interpolation (BC), which is then added to the BC image to obtain the super resolution (SR) image. Contrast this to the EDSR-type networks, which take in an LR image and directly output the SR image using residual skip connections to maintain network stability with depth, and using subpixel convolutions to upsample the data within the network itself.

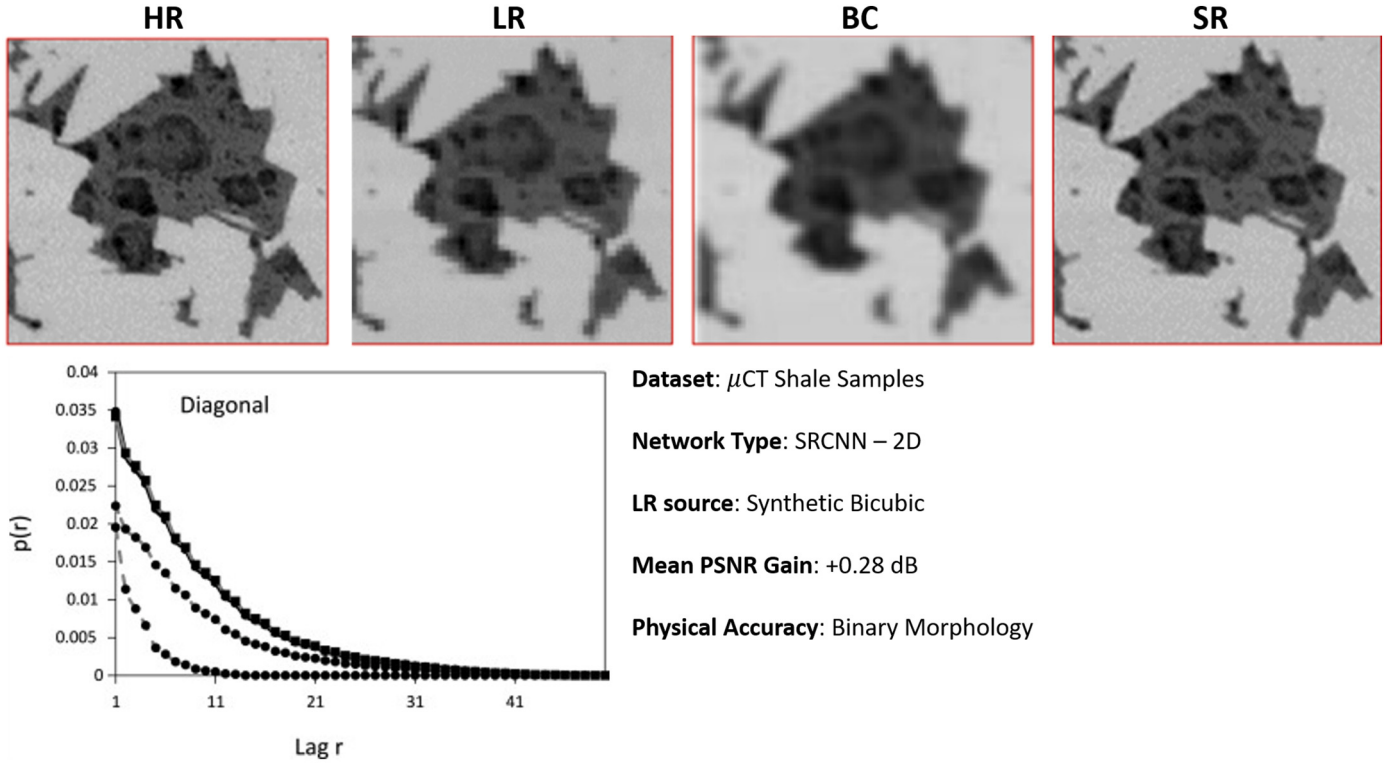


**Fig. 13.** Top: Visualizations of a cropped portion of an input image shows that Super Resolved (SR) results show higher visual clarity than bicubic interpolation (BC) and Low Resolution (LR) images, compared to High Resolution (HR). Bottom: Comparison of the Multi-Point Correlation (MPC)  $p(r)$  function over different lengths (similar to variograms) for HR (Solid black and gray), LR (dotted gray), BC (dashed gray), and SR (solid gray) images. The MPC results for the HR and SR images are nearly identical. Reprinted with permission (Kamrava et al., 2019a).

the SR-ResNet (Ledig et al., 2017), EDSR (Lim et al., 2017), and WDSR (Yu et al., 2018) models were trained on the Digital Rock Super Resolution Dataset (DRSRD) (Wang et al., 2019d). The image PSNR for all models and their variants were compared, showing a 3–5 dB improvement. It was found that there is a minimal difference in the PSNR

achieved per model, but that WDSR models tended to perform slightly better while requiring only a fraction of the required model parameters. The best performing model (WDSR-B w/32 layers) was then used to super resolve unseen digital rock images, posting a 2–3 dB improvement. These included Bentheimer, Berea, and Leopard sandstones, and

Savonnières carbonate to encompass a typical range of common digital rocks. The model was then retrained and tested with noise and blur augmentation on low resolution Bentheimer images with natural noise and blur to investigate the impact of image noise on SR, showing losses in performance, but robust edge recovery. Finally, the network was tested on the original HR data to observe the image characteristics of HR-SR images and the flexibility of the model, visually showing comparable performance despite operating on HR images with much larger and well resolved features (see Fig. 14).

In 3D, a 12 layer SRCNN-type network was trained and tested on sandstone images (Wang et al., 2019f) taking the form of sequential ReLU activated convolutions with a residual learning strategy. The network was tuned with varying numbers of layers, filters, and kernel sizes, with peak performance posting a gain of 3 dB on the testing data with a scale factor of 4 $\times$ . Other scale factors of 2 $\times$  and 3 $\times$  were also tested, showing gains of 4.7 dB and 2.5 dB respectively. A visual depiction of achieved results is shown in Fig. 15.

Overall, processing micro-CT images of sandstone and carbonate rocks using SRCNNs as a part of digital rock imaging has been shown to produce high quality, high resolution images that are optimized for further segmentation and gray-scale analysis. The PSNR compares favorably against typical interpolation methods, and difference maps indicate that edge sharpness is completely recovered in images within the scope of the dataset with only high frequency noise related detail loss. Besides the generation of high-resolution images, a beneficial side effect is the removal of image noise while recovering edgewise sharpness when training on augmented images with noise and blur. Thus the SRCNN method generates representative high-resolution images, and preconditions them for image segmentation due to a fortunate feature with network performance failing to recover texture (which usually manifests as unwanted noise in reasonably well-resolved cases). Image restoration by SRCNN on the rock images is of significantly higher quality than traditional methods and suggests SRCNN methods are a viable processing step in a digital rock workflow.

There are a number of potential issues that arise from the use of SRCNN/EDSR networks. Firstly, the key issue of performance, that is, the loss of texture detail in SR images which can be problematic for under-resolved carbonate rocks for example, where much of the texture represents the micro-porosity. Secondly, the issue of physical accuracy,

whether these SR images are accurate in terms of their flow parameters. Thirdly, the issue of datasets, since these networks are trained and tested on synthetically downsampled LR images, which may not represent the gray-scale characteristics of true LR images, which tend to have different contrast, noise, and blur (especially since synthetic downsampling tends to reduce noise in the LR domain). These main issues with super resolution methods remain open questions, but are partially addressed by the introduction of SRGANs and SRCycleGANs into the workflow of Digital Core Analysis, which are outlined in following sections.

**Texture Regeneration:** Texture within images is difficult to regenerate in a physically accurate manner using SRCNNs. In this case, texture can be defined as image features that are under 35 voxels in diameter, which tend to be smoothed-out by SRCNNs (as can be seen from examples in the previous section). The use and importance of texture in micro-CT images for Digital Core Analysis is a developing field of research. One such application is the characterization of in situ gray-scale phases/minerals in an automated process using the Gray Level Cooccurrence Matrix (GLCM) (Haralick et al., 1973). It has found success in the characterization of texture in medical images (Makaju et al., 2018; Madero Orozco et al., 2015; Sivaramakrishna et al., 2002; Alexander et al., 2015; Liao et al., 2011; Yang et al., 2012) and digital rock images (Singh et al., 2019; Becker et al., 2016; Jardine et al., 2018; Singh et al., 2020). While currently little used in the field of Digital Rocks, texture-based analysis is a common and useful tool in characterising medical CT images within the Radiomics field of study (Singh et al., 2019). Unique rock images possess unique radiomic signatures, providing an unbiased representation of texture, which are not offered in classical segmentation methods.

SRCNN/EDSR methods tend to have high pixelwise accuracy values but a low perceptual quality, with high frequency texture features lost as smearing occurs in order to achieve a high “average” accuracy that represents multiple possible HR realizations (Dosovitskiy and Brox, 2016), a manifestation of the local minima problem in neural network training. While larger scale features that have high contrast edges over multiple pixels are recovered by SRCNN, the overall image fidelity is unsatisfying due to the loss of texture. Efforts to address this problem have resulted in the use of hybrid loss functions that combine a pixelwise L1 or L2 loss with a featurewise loss that is calculated as the L2 loss of features extracted from a convolutional layer in a pretrained model

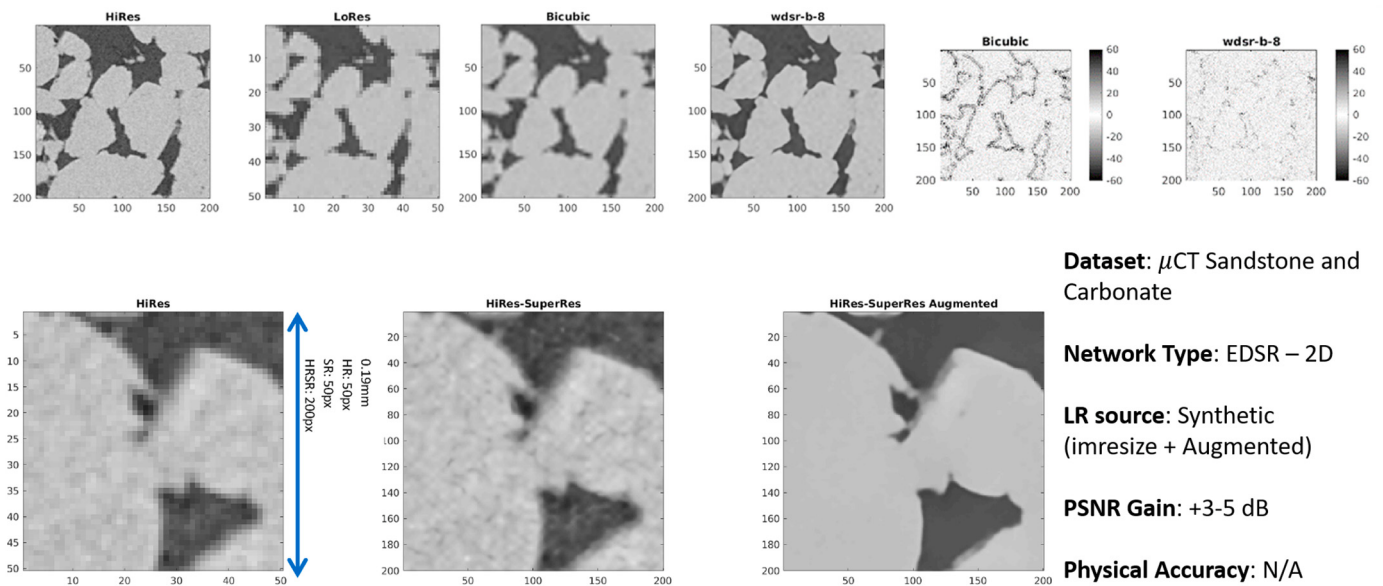


**Fig. 14.** Top: Visualization of a cropped portion of an input image shows that Super Resolved (SR) results show higher visual clarity than Bicubic Upsampled (BC) and Low Resolution (LR) images, compared to High Resolution (HR). Bottom: Further visualization of Super-Resolved-High-Resolution (HR-SR) and Augmented (denoised + deblurred) results, showing high edge accuracy and noise reduction.

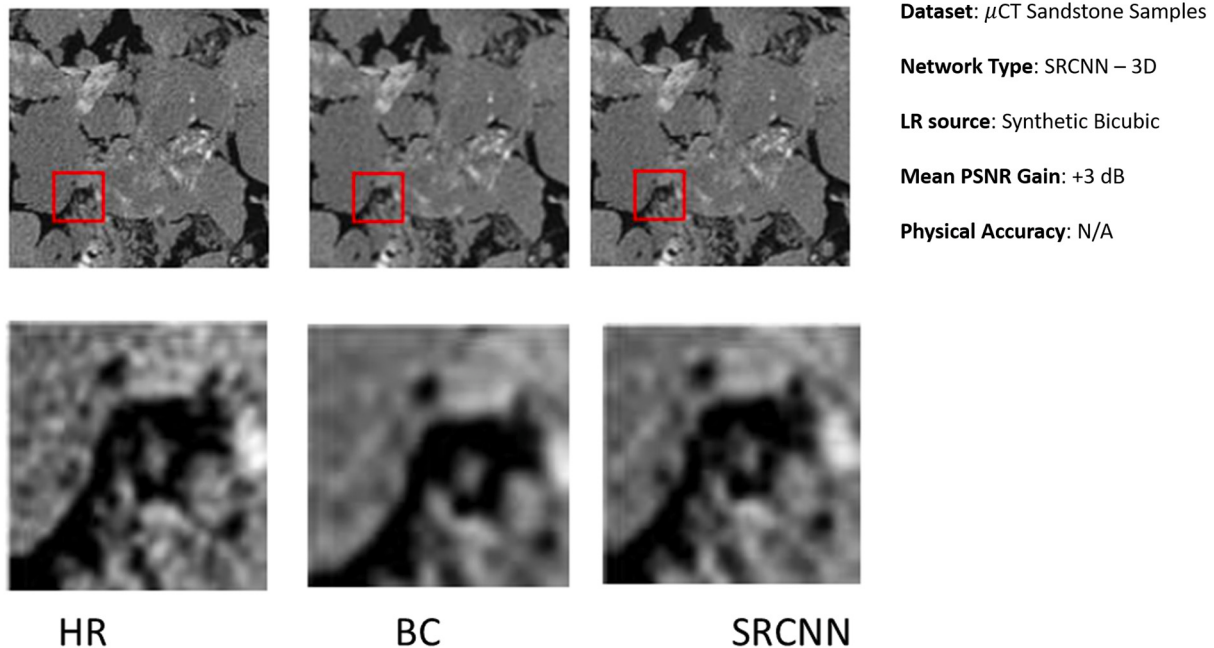


**Fig. 15.** Visualization of a cropped portion of input image shows that Super Resolved (SR) results show higher visual clarity than Bicubic Upsampled (BC) and Low Resolution (LR) images, compared to High Resolution (HR). Reprinted with permission (Wang et al., 2019f).

(Johnson et al., 2016), such as grain boundaries, granular texture, intensity variations, etc. While this has shown superior perceptual results compared to standard loss functions, the problem of texture loss has been most successfully addressed by the introduction of the Super Resolution Generative Adversarial Network (SRGAN). By combining a SRCNN network (the generator) with an image classification network (the discriminator), an SRGAN is formed, whose standard architecture is shown in Fig. 16, using EDSR as the generator.

In this section, the SRGAN predominantly follows the format outlined in section 2.3.1, with some extra features that take into account the input low resolution data. SRGAN attempts to generate SR images from LR images that are as close to HR images as possible.

The generator  $G_{SRGAN}$  takes the same form as the EDSR-type network:  $G_{SRGAN} \equiv G_{EDSR}$ , and the generator loss function is comprised of 1) the pixelwise loss function:  $f_{pixelloss} = (|SR - HR|)^p$  where  $p = 1, 2, 2$  2) the adversarial loss function:  $f_{advloss}$ , and 3) the perceptual loss function obtained from the VGG network (Ledig et al., 2017):  $f_{vggloss} = (VGG(SR) - VGG(HR))^2$ . Together, these form the generator loss  $f_{gloss} = f_{pixelloss} + \alpha f_{vggloss} + \beta f_{advloss}$ , where  $\alpha$  and  $\beta$  are scaling factors. The discriminator  $D$  is trained as a regular GAN:  $D_{SRGAN} \rightarrow \min(f_{dloss}(D_{SRGAN}(SR), D_{SRGAN}(HR)))$ . SRGANs have been applied to the generation of photo-realistic and highly textured images that score highly on human surveys of image quality (Ledig et al., 2017; Dosovitskiy and Brox, 2016). While SRGAN results in features that look to the human eye as realistic when surveyed, the resulting generated SR images are lower in pixelwise accuracy compared to SRCNN due to pixelwise mismatch (You et al., 2018). Since  $\mu$ CT images contain significant amounts of image noise and texture as high frequency features, this is also inadvertently recovered. As image segmentation is common in most Digital Rock workflows (Jassonov et al., 2009), SRCNN tends to suffice as they possess some form of intrinsic noise suppression while maximising edge recovery (Wang et al., 2019a). While sufficient for conventional samples that are resolvable at the 3–5  $\mu$ m resolution scale, the blurring of grain texture is detrimental to images such as carbonate and coal, with significant under-resolution features. Implementation of SRGANs in boosting the resolution and recovering the texture of micro-CT images of pore-scale rock features has been performed on 2D and 3D images of various

rock types. In particular, SRGAN studies have also focused on the physical accuracy achieved by SRCNN and SRGAN networks.

The first such implementation of SRGAN (Wang et al., 2020a) used the DeepRock-SR dataset (Wang et al., 2019e) compiled from the Digital Rocks Portal to train and validate the results from the Super Resolution Generative Adversarial Network, where the generator (acting as the SRCNN) was a modified EDSR (Lim et al., 2017) network and the discriminator was a deep convolutional classifier. Performance achieved was in line with expected improvements in PSNR of +3–5 dB, which translates to a reduction in relative pixelwise error of 50% to 70% respectively. Difference maps of the validation sample images confirmed SRCNN recovery of bulk features, while the SRGAN network was able to regenerate the high resolution texture. Extrapolation of network performance with unseen external images incurred minimal performance loss, and 3D testing of physical accuracy as measured by permeability and connectivity (Euler Number) on consistently segmented images showed SRGAN results achieving the closest match, though the natural denoising of EDSR results reduced connectivity sensitivity during segmentation. Denoising and deblurring was also explored similarly to previous SRCNN findings (Wang et al., 2019a), and HR-SR images were similarly generated and compared. Of note in this case was a direct comparison against SEM images, showing excellent visual regeneration of under-resolution features across a wide range of image resolutions, though the SEM images themselves were not used for training purposes (see Fig. 17).

Aside from physical measures of accuracy using topology and single-phase flow, a more in-depth investigation was performed on the effect of super resolution on the construction of Pore Network Models (PNMs) and subsequent single-phase and two-phase flow simulation in these PNMs (Janssens et al., 2020). Training and testing was performed on a registered internal carbonate dataset, rather than external samples, eliminating extrapolative uncertainty. A U-Net (Ronneberger et al., 2015) generator was used (instead of EDSR-like variants) which takes the BC image as an input and returns an SR image. The same expected trends in physical accuracy were observed, where SR images recovered lost connectivity much better than the LR or BC images, leading to a closer match in permeability calculations. Two-phase flow simulations

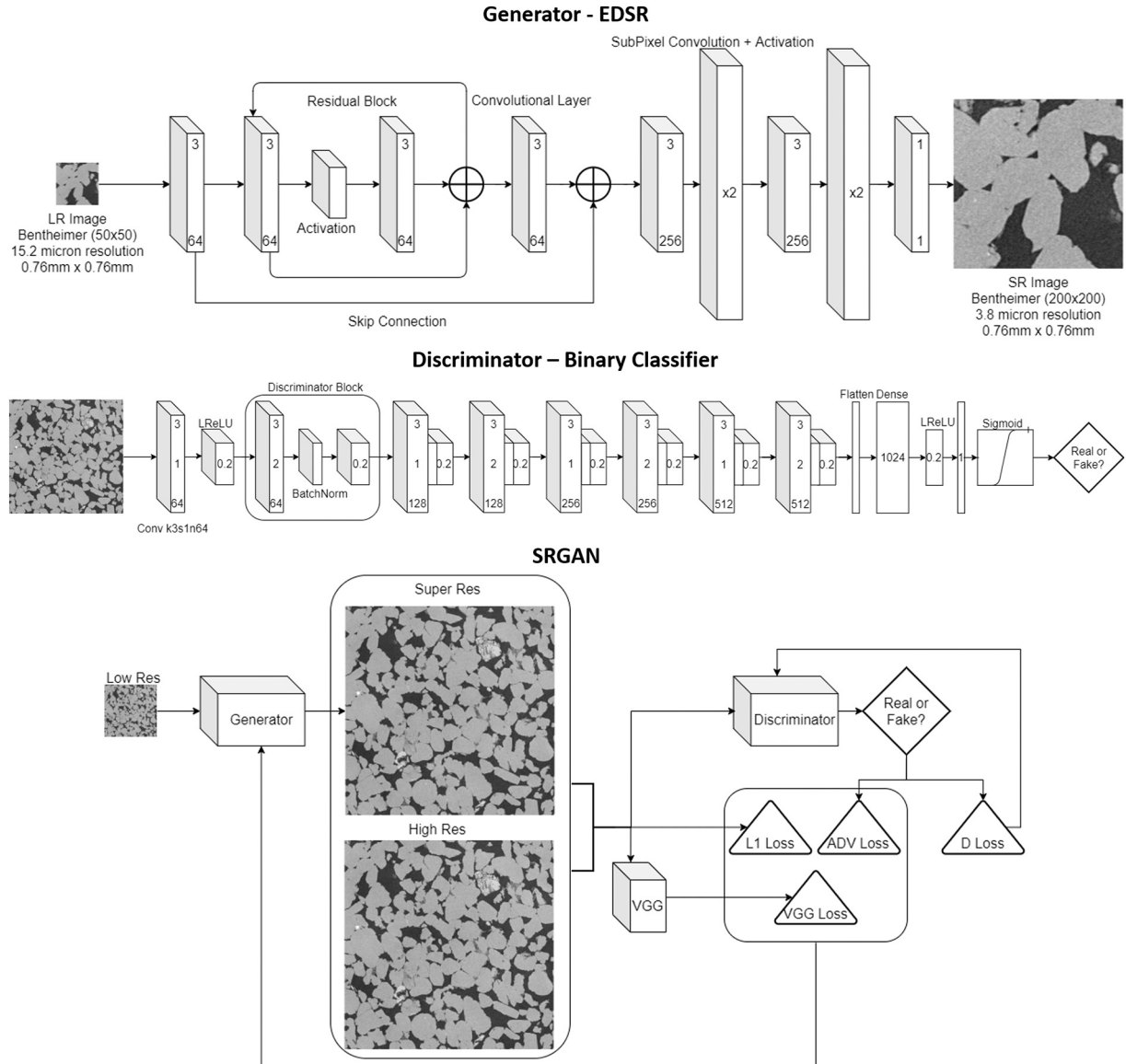


**Fig. 16.** Top: Example of the typical generator network used in Super Resolution Generative Adversarial Networks (SRGANs), the EDSR architecture, which learns to generate increasingly realistic images. Middle: typical architecture used for the discriminator in SRGANs, which learns to identify whether images fed into it are real or fake. Bottom: the coupling between Generator and Discriminator forms the SRGAN. Reprinted with permission (Wang et al., 2020a).

on pore network models constructed on the SR, LR, and SR images showed that SR and HR PNMs are closely matched in structure, naturally leading to similar results in drainage and imbibition simulations (Fig. 18).

The primary limitation of SRCNN/EDSR methods of grain texture loss is addressed effectively by the SRGAN, which is capable of boosting resolution and recovering the texture of 2D and 3D micro-CT images of digital rocks past their hardware limits. Texture recovery by SRGANs shows superior similarity compared to normal SRCNN and other interpolation methods. Furthermore, the issue of physical accuracy has been explored, with analysis of connectivity and permeability of consistently segmented images showing that the boosted resolution and recovered texture in SR images is physically accurate over a range of segmentation realizations. Further physical analysis with PNMs showed similar trends in physical accuracy, indicating that the connectivity of SR-PNMs and HR-PNMs is very similar, leading to similar flow simulation outcomes. Notable is that thus far, a study of direct two-phase flow simulation over a broad range of different rock types with SRCNN/SRGAN applied has not been performed.

The recovery of both features and texture from LR images is beneficial for characterising digital rocks that are dominated by under-resolution micro-porous features such as in carbonate and coal samples. Images can be constrained by the brittle mineralogy of the rock (coal), by lower quality fast transient imaging (waterflooding), or by the energy of the source (micro-porosity). These limitations can be overcome and super resolved accurately for further analysis downstream. One such analysis technique that is an emerging topic is the use of texture analysis in characterization and subsequent segmentation (Singh et al., 2019; Singh et al., 2020), which is a factor that has been mostly absent in traditional segmentation techniques (Iassonov et al., 2009).

With the rapid development of SRCNN models, the models outlined here serve as indications of performance, as incremental improvements in network architecture in the future may further improve upon the results presented and discussed. One major limitation is the issue of synthetic LR datasets. Training for SRCNN and SRGANs are usually done on synthetically generated images, and though augmentation of the synthetic low-resolution images have produced better super resolution outputs, a proper dataset with real low and high resolution micro-CT

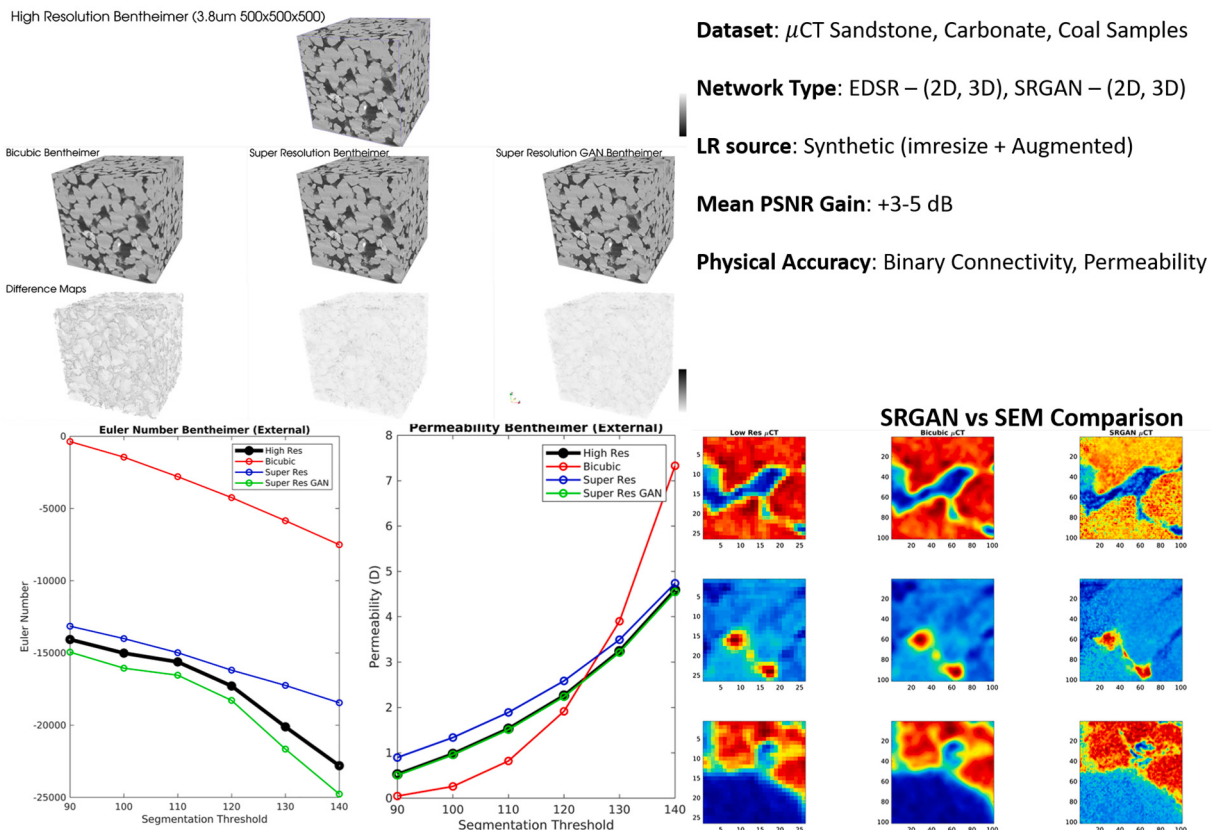
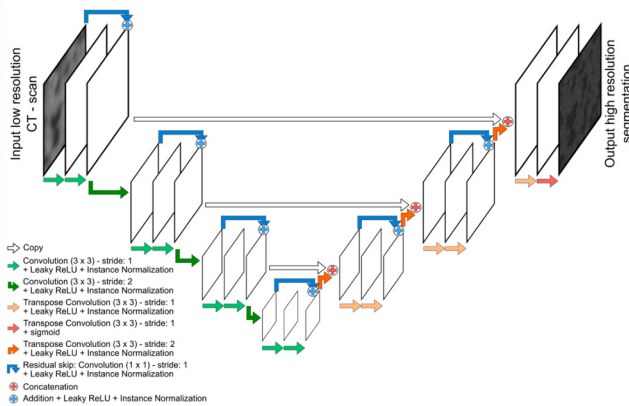


**Fig. 17.** Left: Visual 3D comparison of bicubic interpolation (BC) and super resolved (SR) images using EDSR and SRGAN. Also shown is a comparison of computed physical accuracy as measured by connectivity (Euler Number) and permeability, showing a close match between SR, SRGAN, and HR images. Right: Comparison of visual features between generated HR-SRGAN images, and SEM images. Reprinted with permission (Wang et al., 2020a).

### U-ResNet Architecture



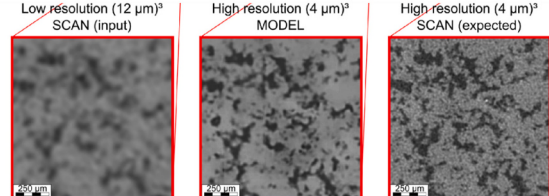
### Dataset: $\mu$ CT Carbonate

**Network Type:** SRGAN – 2D (U-ResNet Generator)

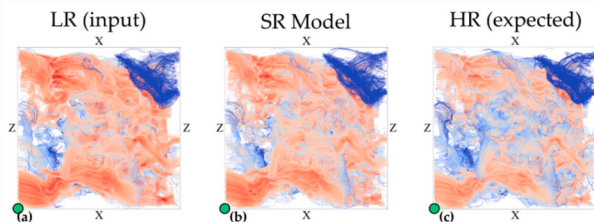
**LR source:** Synthetic Bicubic + Real LR

**Mean PSNR Gain:** N/A

**Physical Accuracy:** LBM Permeability, PNM two-phase



### Velocity Field Comparison



### PNM Relative Permeability Comparison

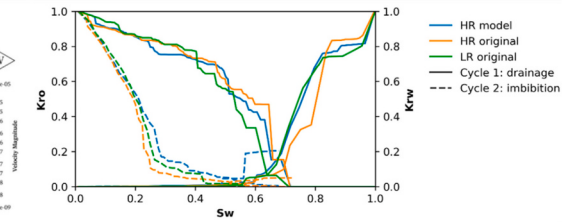


**Fig. 18.** Figures showing the U-Net-like network used in a study of physical flow accuracy of carbonate super resolution. Both single-phase Lattice Boltzmann Method (LBM) and two-phase Pore Network Modeling (PNM) showed a closer match to HR with SR due to improved identification of edges compared to LR and BC images. Reprinted with permission (Janssens et al., 2020).

data would result in a closer mapping between real LR image characteristics and HR images. Such a dataset would either need to be carefully registered so that real LR images and real HR images are a pixelwise match in order to be used in the SRGAN architecture, or be trained and fed into a SRCycleGAN network that is able to learn the LR to HR mapping on unpaired images (albeit with some performance loss).

**Unpaired Multi-Resolution Imaging:** With some minor modifications to the original CycleGAN network (see Section 2.3.2), an SRCycleGAN can be created, which can learn the LR to HR mapping on unregistered images, removing the dependency on synthetic downsampling to generate training data. By passing in a BC image as input instead of a LR image, the structure of CycleGAN is preserved with minimal changes. A visual depiction of this architecture is shown in Fig. 19. One caveat of SRCycleGANS is that, when trained and tested on truly unpaired LR-HR data, the traditional PSNR measure of accuracy and any other measure that relies on registered images becomes invalid unless the dataset was originally paired and cycleGAN training was performed on selected unpaired examples. Other measures based on unpaired statistics are used instead, and physical accuracy of similar regions can be calculated. Initial implementations of SRCycleGANS in unpaired 2D sandstone images showed that SRCycleGAN significantly outperforms BC images, with a closer match to the original HR images. Methods of comparison used include gray-scale measures of entropy, and segmented measures of porosity, porosity distribution, two-point correlation, lineal-path, two-point cluster, chord-length distribution, and pore size distribution (Chen et al., 2020).

A further extension of SRCycleGAN based on the Cycle-in-CycleGAN (CinCGAN) (Yuan et al., 2018) has also been implemented for super resolving real 3D LR micro-CT images (Niu et al., 2020). CinCGAN performs the task of denoising and deblurring in a separate cycle than super resolution, rather than SRCycleGAN, which performs all 3 tasks in the same generator. In this case, the segmented porosity, pore size distribution, Euler number, and permeability was calculated to ascertain accuracy in a physical sense. Resulting analysis of these physical measures as seen in Fig. 20 show similar trends in accuracy to results obtained with SRGAN previously (Wang et al., 2020a).

Since data pairing is not required for SRCycleGANS, the potential datasets that can be used for training and testing become much broader, and the issue of synthetic datasets is mitigated. The network architecture

has performance limits such as loss function sensitivity and a general loss of texture due to both the increased difficulty in network minimization and the use of the total variation loss function (designed to remove transposed convolution artefacts caused by poor minimization). With these issues in mind, one can devise a network wherein the unpaired benefits of cycleGAN can be combined with the higher performance of paired SRGAN/SRCNN. Instead of a single cycle SRCycleGAN (Chen et al., 2020), or a dual cycle CinCGAN (Niu et al., 2020), a hybrid architecture can be used, with a cycleGAN used for unpaired denoising/deblurring, and an SRGAN for super resolution. Such a network is commonly used for “real-world” super resolution (Zhang et al., 2020).

Overall, in the task of super resolution for pore-scale imaging, a focus on micro-CT imaging has led to the implementation of the SRCNN (edge recovery), followed by the SRGAN (edge and texture recovery), and finally the SRCycleGAN (unpaired real datasets). These tools have shown to provide physically accurate digital rock images with a resolution-FOV that surpasses the capabilities of imaging hardware, which allows the generation of a real sample that more closely matches the dimensions of core samples used for petrophysical analyses in the laboratory, particularly important for two-phase flow simulations where the morphology of phases and resulting flow dynamics are driven by non-local forces that extend beyond the length scales typically used in digital rock studies (Armstrong et al., 2016). Heterogeneous rock samples and other multi-scale features where a larger FOV is required at high resolution to achieve a representative elementary volume (Menke et al., 2018) also become more accessible, and the under-resolved features of carbonates and coals for example, become resolvable with future training of SEM-micro-CT datasets.

### 3.2.2. Image generation/extrapolation

Aside from processing real 3D images obtained from scanners, synthetic images can be generated from scratch, or extrapolated out of subsamples in the form of 2D slices or smaller 3D volumes. This is commonly referred to as “synthetic image reconstruction”, and it is important to briefly note that the term “image reconstruction” can refer to either creating a 3D volumetric image from 2D projections of a rotated sample, or generating a “fake” but statistically representative pore-scale image of a certain type of rock or material using 3D training images or otherwise. In this section the latter is referred to from a Deep

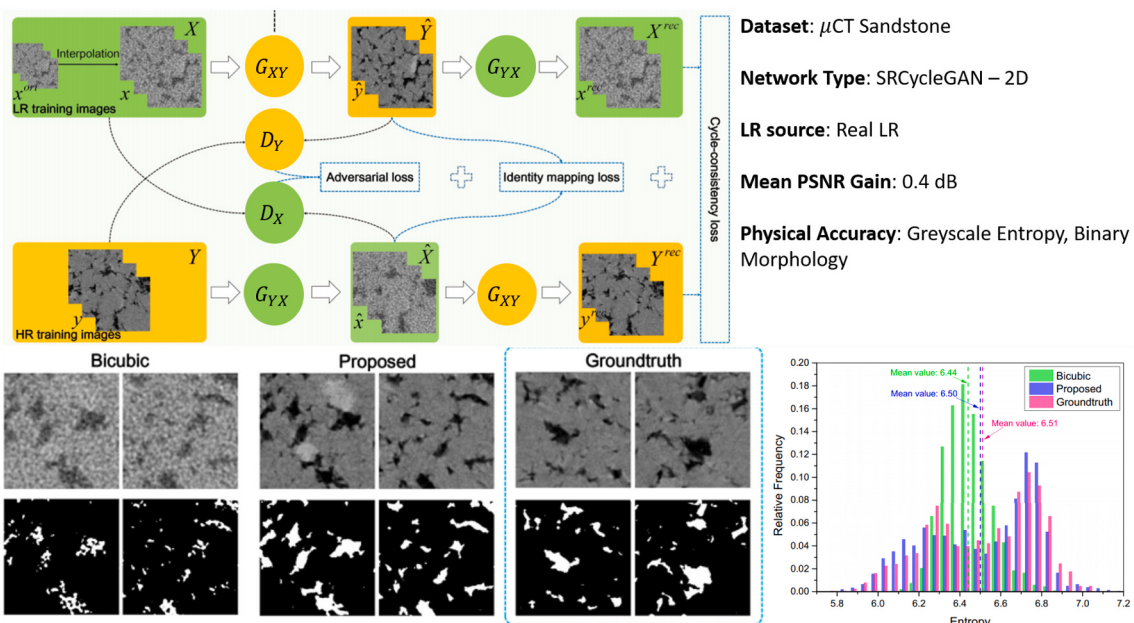


**Fig. 19.** Figures showing the SRCycleGAN network used in a study of super resolution with real unpaired micro-CT images. A moderate PSNR gain of 0.4 dB was measured, and gray-scale entropy measures shows a good visual match. Reprinted with permission (Chen et al., 2020).

**Dataset:**  $\mu$ CT Sandstone

**Network Type:** Cycle-in-CycleGAN – 2D

**LR source:** Real LR

**Mean PSNR Gain:** N/A

**Physical Accuracy:** Binary Connectivity, Permeability

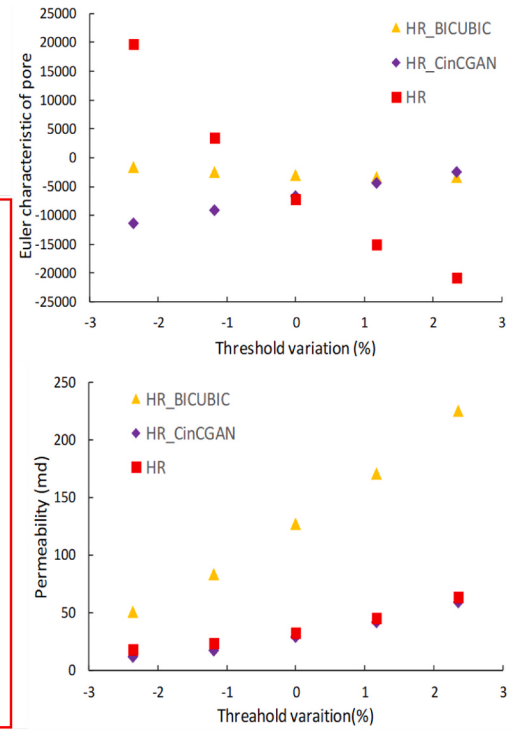
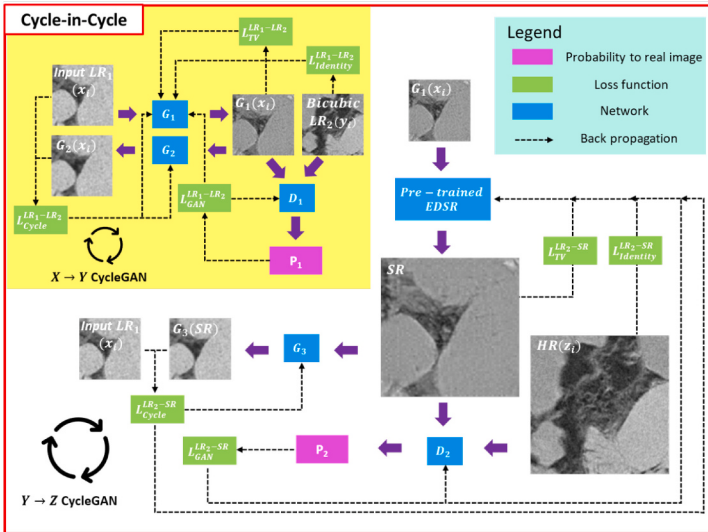


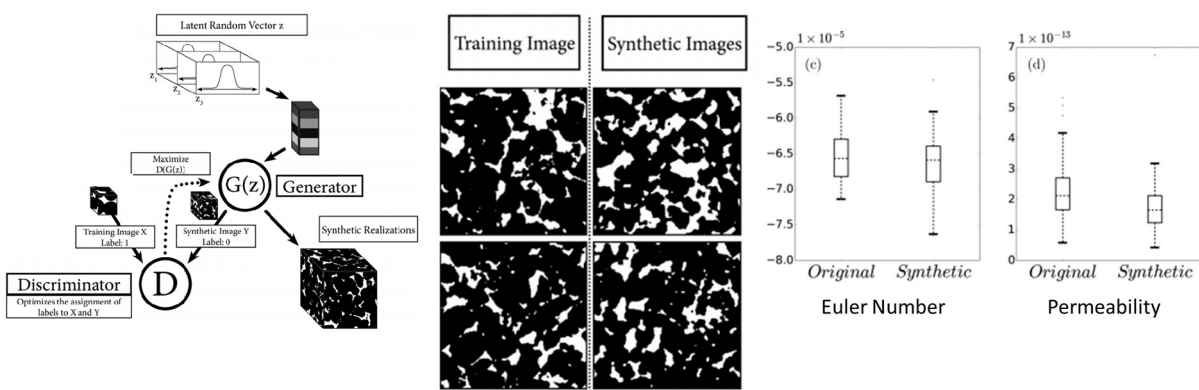
**Fig. 20.** Figures showing the CinCGAN network used in a study of super resolution with real unpaired micro-CT images. In this study, the permeability and connectivity are shown with comparison between high resolution (HR), super resolution (SR) (from CinCGAN), and bicubic interpolation (BC) shows similarly, that SR images possess similar physical characteristics to HR images. Reprinted with permission (Niu et al., 2020).

#### Learning perspective.

There exist numerous fast synthetic techniques that do not aim to necessarily generate a physically accurate sample, such as correlated fields (Wang et al., 2020c; Liu and Mostaghimi, 2017a), morphological transforms (Santos et al., 2020), and interpolation based approaches (Rabbani et al., 2020). Naturally, reconstructing an accurate representation of a rock type requires some form of learning-by-example. Commonly used in pore-scale imaging and geostatistics are higher order multiple point statistics and simulated annealing for example (Okabe and Blunt, 2007; Smith et al., 1983). These learning-based approaches are essentially minimization problems (especially simulated annealing) and as such, the use of Deep Learning for the purpose of

synthetic image generation is a natural evolution of traditional methods. Given the stochastic nature of the methodology, the neural network architecture most commonly used for this purpose is the Generative Adversarial Network (GAN) (Goodfellow et al., 2014) and its variants.

Image generation with GANs is usually guided by either training data only, or input and training data. In the first case (Fig. 21), a latent vector of random numbers was passed into  $G$  (Mosser et al., 2017a; Mosser et al., 2017b) and this random information was then transformed into the solution space occupied by the training examples using a CNN architecture with transpose convolutions to perform the upsampling and decoding. In the second case (see Fig. 22), an input of some sort with added latent noise, such as a 2D slice or set of 2D slices was given to  $G$  to



**Dataset:** Segmented Sandstones, Carbonates

**Network Type:** GAN

**Source:** Random Vector

**Physical Accuracy:** Morphology, Permeability

**Fig. 21.** Left: schematic of a stochastic GAN implementation for generating porous media. Middle: example slices of outputs compared to training data. Right: connectivity and permeability ranges for the training data and the generated data, showing preservation of physical characteristics during GAN synthetic generation. Reprinted with permission (Mosser et al., 2017a).

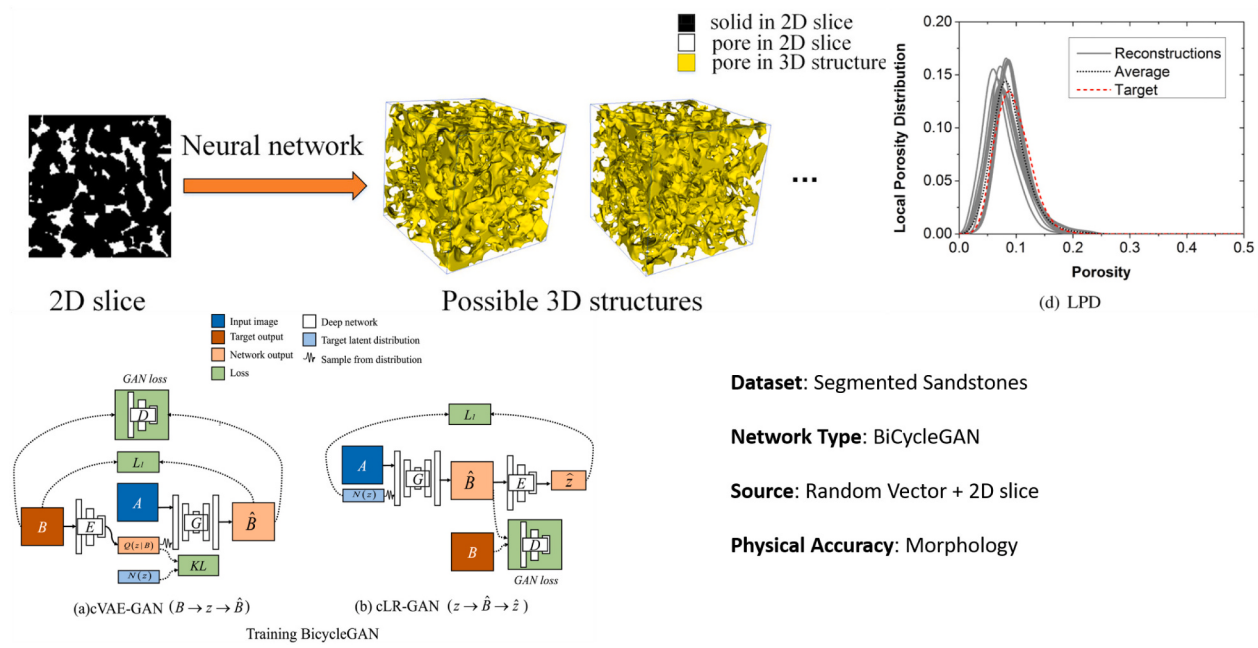


**Fig. 22.** Figures showing the extrapolation of porous media using both a random vector and a 2D slice, implemented with *Bi-CycleGAN*. Reprinted with permission (Feng et al., 2020).

provide a narrower guidance in terms of extrapolation (Feng et al., 2020).

Studies using latent vectors as input into a GAN, trained on segmented examples of Ketton carbonate, Berea sandstone, and bead packs (Mosser et al., 2017a) have shown that this method is capable of generating synthetic images that share the similar ranges for porosity, specific surface area, Euler characteristic, and permeability. This has also been shown to be the case for generating gray-scale realizations (Mosser et al., 2017b) (that are subsequently segmented). In the case of using 2D slices and noise as guiding input, a study using the Bi-CycleGAN network has shown similar (if not better due to increased input information) performance to the case of simply using a latent vector (Feng et al., 2020), which allows a broader range of examples to be used for training.

Generation/extrapolation of synthetic porous media has advanced significantly with the use of GANs, and their accuracy in generating synthetic samples within the scope of the training examples has been shown to be reliable and verifiable with morphology and physical modeling.

#### 4. Deep learning in pore-scale modeling

After obtaining a high resolution, segmented digital image, pore-scale modeling can be performed, which predominantly concerns itself with computations of fluid flow within the pore space. This is then used to compute the permeability and relative permeability by upscaling Stokes flow. (Mostaghimi et al., 2013) (mm to  $\mu\text{m}$ ) to the core-scale (cm) and reservoir-scale (m) using Darcy's Law. This task is applicable to a wide range of fields including petroleum engineering, environmental studies, and hydrology (Fenwick and Blunt, 1998; Hilpert and Miller, 2001; Culligan et al., 2006; Mostaghimi et al., 2010; Mostaghimi et al., 2016; Blunt et al., 2013). Flow simulation in porous media involves either single-phase or multiphase flow, using techniques that typically balance accuracy with speed. The primary techniques used in single-phase flow are, in order of low-accuracy/high-speed to high-accuracy/low-speed; Pore Network Models (PNMs) (Blunt et al., 2002; Dong et al., 2008; Rabbani and Babaei, 2019), Semi-Analytical Laplace Solvers (SASs) (Chung et al., 2019; Wang et al., 2019b; Wang et al., 2020b; Torskaya et al., 2014; Shabro et al., 2012), and Direct Simulation,

usually Lattice Boltzmann Methods (LBM) or Finite Volume Methods to solve the Navier Stokes Equation (NSE) (McClure et al., 2014; Manwart et al., 2002; Spaid and Phelan Jr, 1997; Stewart et al., 2006; Boek and Venturoli, 2010; Chen et al., 2015; Hao and Cheng, 2009; Keehm et al., 2004). The choice of whether to use PNMs, SASs, or LBM/NSE depends on the required accuracy, whether just permeability estimation is required (PNMs and SASs work well), or velocity fields are required, such as is the case in solute transport for example (Wang et al., 2020c) (LBM and NSE work well).

In multiphase flow, PNMs and LBM are similarly commonly used, with the accuracy/speed trade-off even more prominent, as direct LBM simulation is more resource intensive for multiphase than for single-phase flow due to fundamental numerical reasons (numerical stiffness), and in a similar vein to SASs for single-phase flow, a middle ground exists for multiphase flow in terms of speed and accuracy in the form of quasi-static morphological methods (Hilpert and Miller, 2001) that model the movement of phases using simplified physical arguments, but directly on the geometry itself.

The role of Deep Learning in pore-scale modeling has developed with two main branches of thought. On one hand, pore-scale modeling is commonly used to determine upscalable petrophysical properties (Blunt et al., 2013), and as such, many implementations have been based on taking geometrical information (either directly or indirectly) from a pore-scale image and predicting a single or suite of reservoir and petrophysical properties using regression (Sudakov et al., 2019; Erofeev et al., 2019; Alqahtani et al., 2020; Kamrava et al., 2019b; Rabbani and Babaei, 2019; Ahmadi et al., 2013; Alqahtani et al., 2021; Rabbani et al., 2020; Tian et al., 2020; Tembely et al., 2020; Wu et al., 2018; Hong and Liu, 2020), most notably the permeability. On the other hand, CNNs have been used as replacement or in conjunction with flow simulation solvers to predict or accelerate pore-scale modeling, resulting in direct predictions of the velocity fields, which can then be processed into permeability or used for further modeling of transport phenomena (Santos et al., 2020; Wang et al., 2020c; Hennigh, 2017; Ribeiro et al., 2020).

In this paper, focus is placed on methods tested on single-phase flow, as applications of Machine Learning and Deep Learning to multiphase flow in pore-scale modeling are mostly unpublished to date (with one exception (Rabbani et al., 2020) detailed in Section 4.1.2 that predicts

relative permeability curves). Where applicable, commentary is provided on potential methods and uses of deep learning on multiphase flow modeling and prediction. Much like the previous paragraph outlining how Deep Learning in pore-scale single-phase flow has branched to upscaling-focused methods and direct pore-space methods, multiphase flow similarly can potentially be split into methods for predicting upscaled relative permeability (Rabbani et al., 2020), and methods for predicting pore-scale phase distributions. Deep Learning methods can potentially be applied to both of these types of multiphase flow problems.

#### 4.1. Deep learning in petrophysical regression

The main petrophysical property that this paper will focus on is the permeability. In general, implementations of neural networks for the purpose of predicting petrophysical properties will predict either only the permeability, or a suite of properties including the permeability (Rabbani et al., 2020). Many studies have shown the relationship between permeability in pore-scale images and geometric/morphological properties such as the porosity, pore geometry, connectivity, tortuosity, etc. (Kamrava et al., 2019b). From these studies, some correlation models have been proposed for linking these geometric properties to permeability, such as the critical path method (Arns et al., 2005), effective medium approximation (Richesson and Sahimi, 2019), and fractal based methods (Xu and Yu, 2008). In essence, these models act as multi-variate regression solutions, taking in information from a database of examples, and generating a “best-fit” non-linear function. This is mathematically analogous regression by Deep Learning.

Deep Learning techniques for predicting permeability are typically either ANNs taking geometric averages of the image as input, or CNNs taking in the image itself as input. These permeability predictions have been used as-is, or as further input into PNMs for accelerated simulation. In all cases, outlined in this paper, LBM is used as the direct simulation routine of choice for the generation of ground truth flow data, although any other direct simulation approach could be used.

##### 4.1.1. Regression using image features

The link between various geometric properties of porous media and its permeability can be uncovered using an ANN, which essentially acts as a type of non-linear multivariate regressor. This method of permeability prediction offers a more light-weight implementation, as many of the geometric properties of porous media serve to reduce the required neural network complexity to learn the permeability of a sample. Notationally, take an example case of an ANN  $N$  that aims to predict the permeability  $k$  when given an input of several other petrophysical parameters, such as the porosity  $\varphi$ , the mean pore size  $\bar{r}$ , and the standard deviation of the pore size distribution  $\sigma(r)$ . The ANN would be trained to predict values of permeability as  $k_{pred} = N(\varphi, \bar{r}, \sigma(r))$ , and optimized by the minimization of permeability predictions  $N \rightarrow \min(f_{loss}(k, N(\varphi, \bar{r}, \sigma(r))))$ .

One of the first uses of permeability regression with ANNs was in conjunction with Pore Network Models (Rabbani and Babaee, 2019), whereby the permeability of 2D cross sections of pores with arbitrary shape was calculated directly with LBM simulations, and then other geometric properties of these cross sections were then related to the resulting permeability through an ANN. The network used here was the simplest possible type, with only one dense layer. One such implementation tested was with an input of 7 geometric measures, passed through a 6-node dense layer to reach an output ( $R^2 = 0.9996$ ). Another simpler implementation tested was with only the mean distance (found through scatter plots to be the most correlated), passing through a 3-node dense layer ( $R^2 = 0.9982$ ). Ultimately, for an application such as this with relatively simple input geometries, it was finally decided that a quadratic relationship between the mean distance and the permeability could be established with similar accuracy ( $R^2 = 0.9960$ ). These aspects

of PNM-LBM are illustrated in Fig. 23. This study serves as a good simple example of how ANN regression for permeability estimation can be applied as a surrogate (replacement) model (a similar surrogate may be possible on multiphase PNM-LBM methods (Zhao et al., 2020)). In classic PNM, a relationship for accurately estimating the permeability of arbitrary cross-sections is not available (Hagen-Poiseuille flow using an empirical shape factor is usually assumed), and as such, LBM can be used for this purpose. By replacing LBM-PNM with ANN-PNM, or even just the quadratic expression, a significant speed-up is achieved with little loss of accuracy. This is mainly facilitated by the relatively simple problem of small, arbitrary 2D cross-sections. In later implementations of ANNs and CNNs, such predictive accuracy has not been achievable on real 3D pore-scale images.

In applications of ANNs for permeability prediction in 3D rock images, studies have been conducted on both synthetically generated images, and real micro-CT images (Tian et al., 2020). In one case, 1000 3D synthetic samples of size  $100^3$ , with porosity ranging from 0.1 to 0.6 and permeability ranging from 0.3 to 1.2 D were generated, and an ANN was then used to predict the permeability of these 1000 samples by first taking 16 different geometric measures as input. A Genetic Algorithm (GA-ANN) was implemented to optimize the network architecture, finally resulting in a 9-layer dense network with different numbers of nodes (neurons) in each layer (a classically designed network would have similar node numbers in each layer), ranging from 74 to 195 neurons. This implementation on the QSGS dataset results in a testing accuracy of  $R^2 = 0.999$ , mostly due to the relatively uniform distribution of samples, with a narrow range of permeabilities (see Fig. 24).

In a separate study with 1100 3D micro-CT rock sub-samples (400 simple geometries measuring  $152 \times 152 \times 175$ , and 759 samples measuring  $100 \times 100 \times 160$ ) extracted from a complex carbonate core-plug with permeabilities ranging from 100 mD to 400 mD, a variety of Machine Learning (ML), ANN, and even CNN methods were used to predict permeability (Tembely et al., 2020). For ML and ANN methods, the inputs used were the formation factor (similar to the tortuosity), porosity, and permeability calculated by PNM. These 3 inputs were passed through several ML-based regression models, including Linear Regression (LR), Gradient Boosting, Random Forest, and ANN. Finally, preceding a more in-depth review in the next section, this study also tested the performance of a CNN-based regression, using only the raw 3D input, in a shallow 2-layer CNN with 1 dense layer, with and without porosity as an extra input. Overall, the ANN ( $R^2 = 0.91$ ) and CNN ( $R^2 = 0.91$ ) implementations performed slightly better (+0.05 in  $R^2$ ) compared to other ML regression methods also tested in the study (Fig. 25).

Overall, the use of ANNs with geometric features of pore-scale images as input to predict petrophysical properties shows promising levels of accuracy, and has shown usefulness in elucidating the relative importance of various other parameters to the permeability of porous media.

##### 4.1.2. Regression using images directly

Instead of relying on geometric characterization of the pore-scale image as input into ANNs, the image itself can be used as input into a CNN to directly obtain a characterization of the geometry, which is then directly fed into an ANN to use these “hidden features” to obtain an estimate for the permeability. This method of permeability prediction (and petrophysical property prediction in general) offers a more “end-to-end”, flexible implementation that does not rely on any extracted geometric features. An ANN still exists within the architecture as dense layers near the end, and so the structure can be thought of as using the CNN to automatically identify geometric features of interest, and passing this directly into an ANN. By offloading the interpretation of data completely to the network, performance of CNN-based regression models becomes more dependent on the architecture and dataset, and less on the choice of input parameters. Nevertheless, these CNN + ANN type regression networks are simply referred to as CNNs.

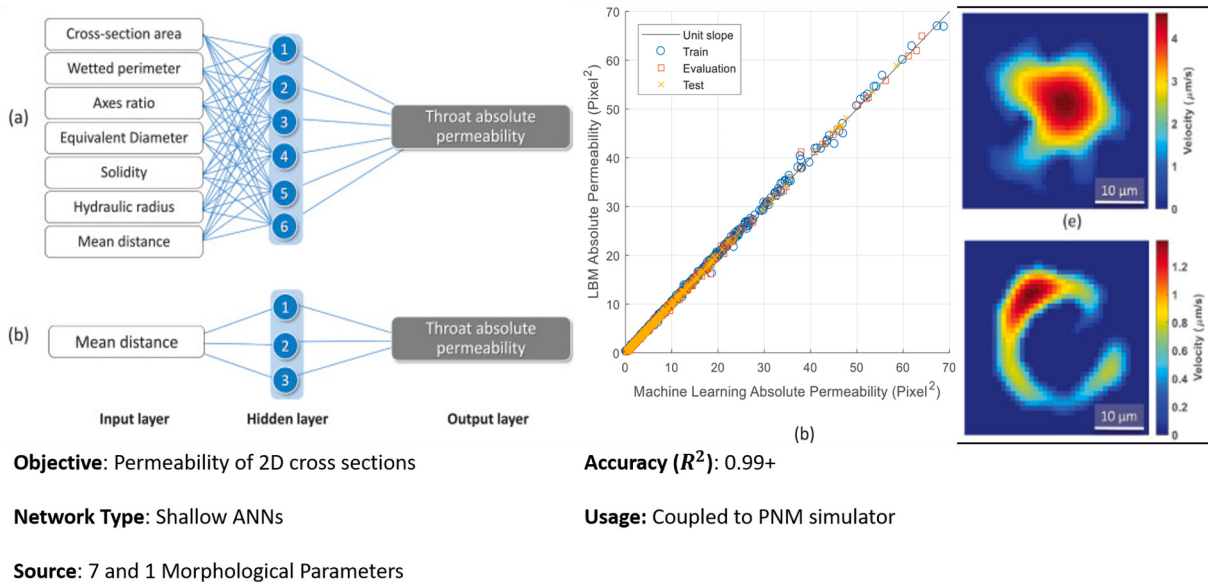


**Fig. 23.** Figures illustrating the PNM-LBM approach, where throat conductivity between pore bodies is first estimated by LBM simulation on the cross-section, and then regressed into a correlation by ANNs. From left to right: depiction of the 1-layer ANNs used with input and output; achieved accuracy over the tested throat geometries; and example of a 2D cross-sectional geometry used in PNM-LBM. Reprinted with permission (Rabbani and Babaei, 2019).

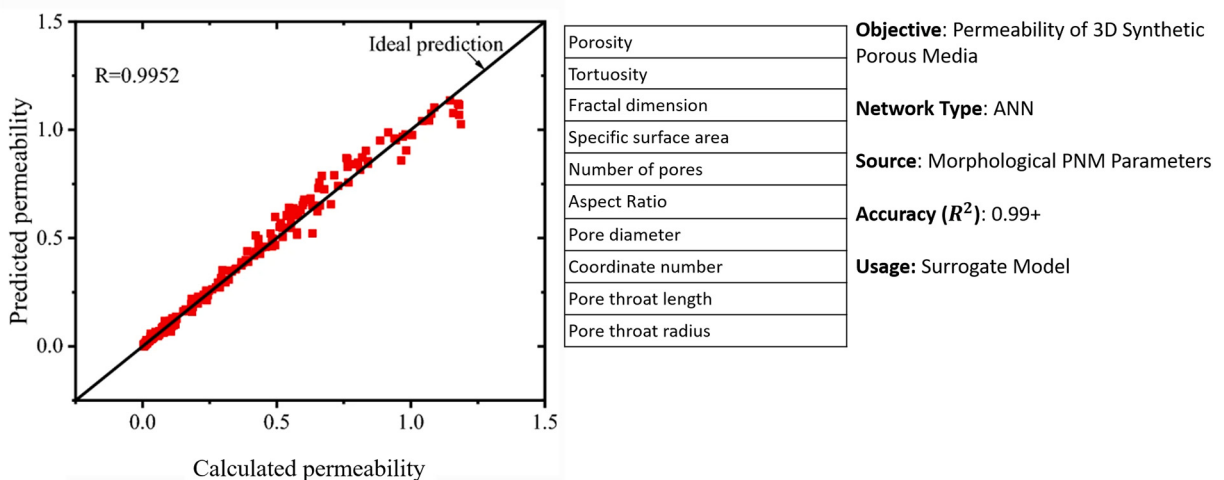


**Fig. 24.** From left to right: Testing accuracy achieved with GA-ANN on synthetic porous media; and simplified list of input parameters. Reprinted with permission (Tian et al., 2020).

Application of CNNs for regression of petrophysical properties has been performed with input 2D images, both segmented and gray-scale (Alqahtani et al., 2020). For a dataset of sandstone images, porosity, specific surface area, and mean pore size were computed, and then a 5-layer CNN with 1 dense layer was trained to predict these values for both gray-scale and binary inputs. Porosity and specific surface area were readily predicted, posting  $R^2 > 0.9$  for binary inputs, and  $R^2 > 0.75$  for gray-scale inputs, while the mean pore size was more difficult to predict, posting  $R^2 < 0.7$  for both binary and gray-scale inputs (Fig. 26).

One of the first studies of permeability prediction was performed on Voronoi Mesh-based geometries with throats (restrictions in the pore space) generated by the mesh edges, and pores generated by removing polygons (Wu et al., 2018). This creates synthetic porous media that deviates from the Kozeny-Carman correlation, and a 2D CNN with 2 convolutional layers and 3 dense layers was used to predict permeability on these geometries. Uniquely, the porosity and specific surface area were inserted into the first and last neurons of the final dense layer to provide physics-based information to the final result. Overall, an

accuracy of  $R^2 = 0.92$  was achieved for testing examples within the scope of the training data, while tests with samples outside the training dataset scope resulted in accuracies as low as  $R^2 = 0.2$ , but still notably better than the Kozeny-Carman prediction, and still within trend as shown in Fig. 27.

A pseudo 3D middle-ground study has also been performed, whereby a 2D 3-layer CNN with 2 dense layers was used to predict petrophysical properties of 3D pore-scale image volumes (Rabbani et al., 2020). This is accomplished by taking the central axis cross sections in X,Y,Z and concatenating these as color channels. A dataset of 17,700 rock samples measuring  $256^3$  was used, generated semi-synthetically by an interpolation algorithm, and a total of 30 petrophysical properties were calculated, of which 15 were scalar values, and another 15 were vectors with 100 values which also included the relative permeabilities calculated from PNM methods. In total, the CNN predicts 1515 values. The resulting accuracy for the entire testing dataset, over all values, was  $R^2 = 0.9385$ . Focusing on the resulting predictions for permeability, a range of 30 mD to 2000 mD was predicted to an accuracy of  $R^2 = 0.92$ .

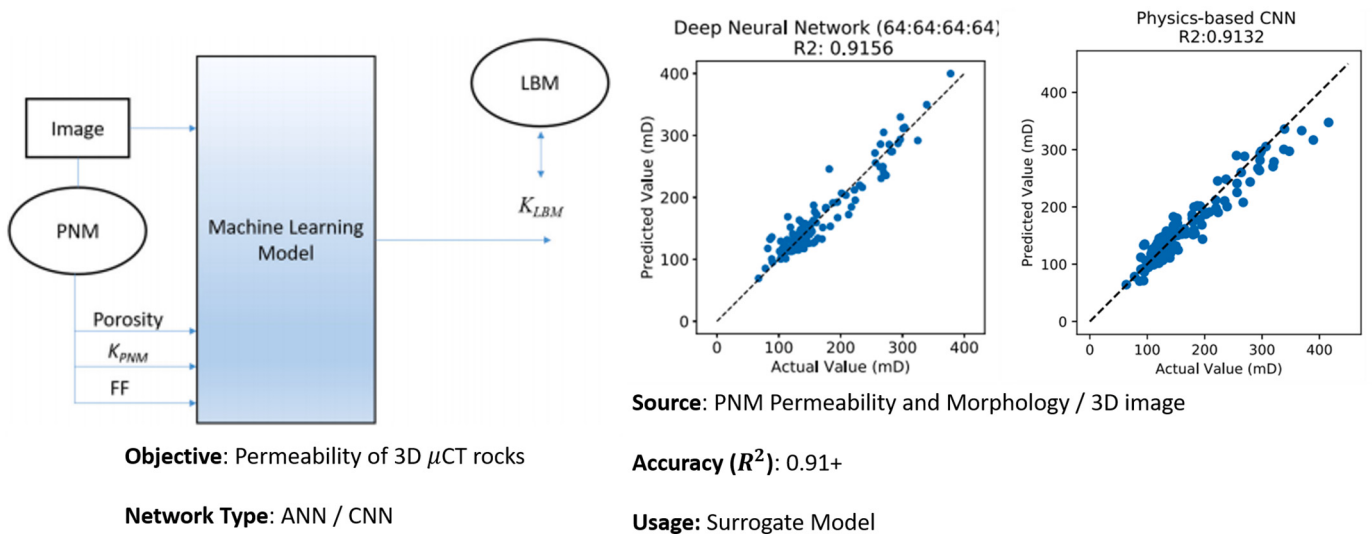


**Fig. 25.** From left to right: schematic of the input and outputs of the regression model; testing accuracy achieved with ANN; and testing accuracy achieved with CNN. Reprinted with permission (Tembely et al., 2020).

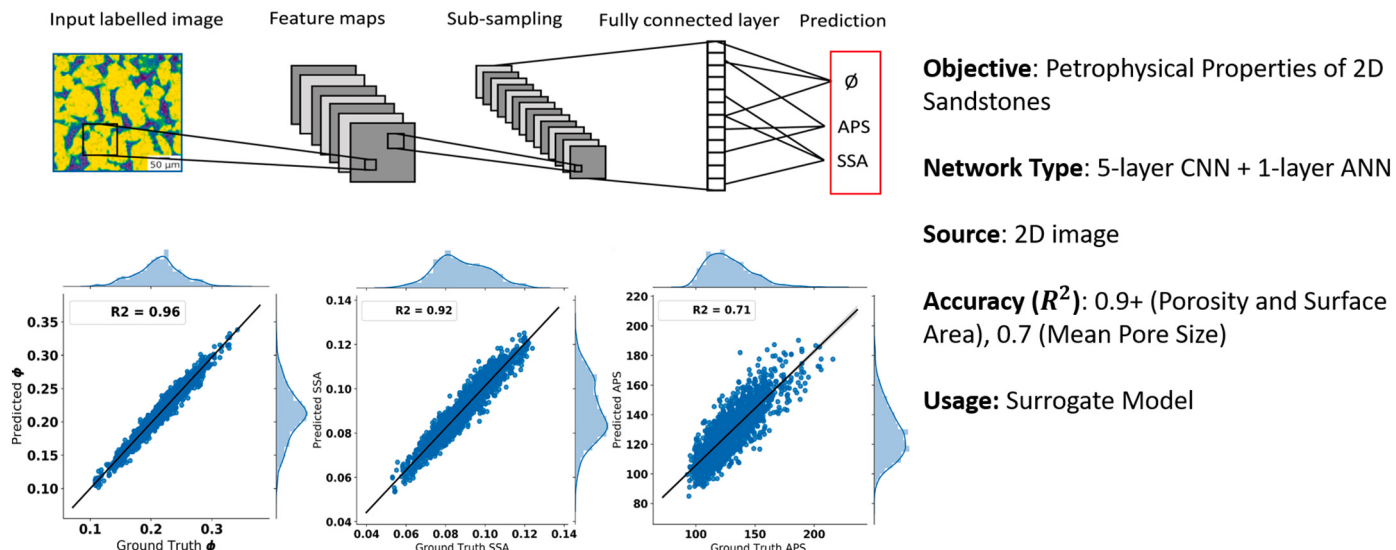


**Fig. 26.** Accuracy of results achieved for a CNN based 2D prediction of petrophysical properties. Reprinted with permission (Alqahtani et al., 2020).

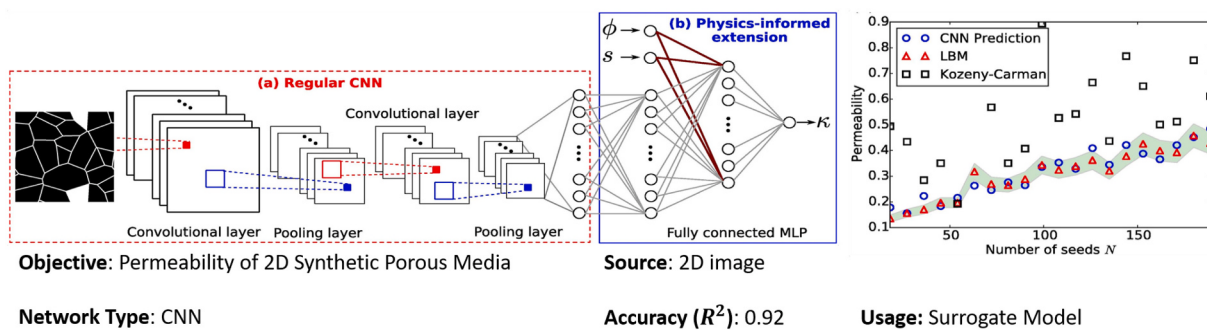


**Fig. 27.** Accuracy of results achieved for a CNN based 2D prediction of permeability. Of interest is the baseline comparison to the Kozeny-Carman relationship, which is absent from other such regression studies, making comparisons between different datasets difficult. Reprinted with permission (Wu et al., 2018).

(Fig. 28), posting similar results in accuracy to ANN regression results, but without a standardized dataset for ANN and CNN physics prediction studies, comparisons cannot be performed with confidence.

In studies of CNN regression using 3D volumes as input, the primary differences in each study are the network design, and the datasets used for training/testing. In one study (Kamrava et al., 2019b), 500

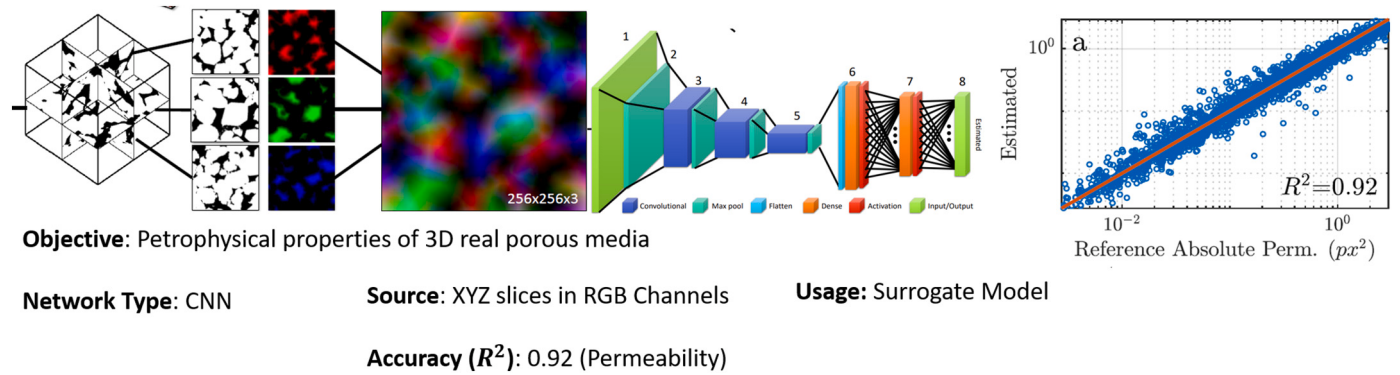


**Fig. 28.** Permeability prediction accuracy achieved with the Deepore implementation, which takes the central cross-sections as color channels in a 2D CNN to predict a wide array of properties. In this case, the permeability prediction is highlighted. Reprinted with permission (Rabbani et al., 2020).

stochastically generated  $200^3$  samples with permeabilities ranging from 100 mD to 500 mD were used for permeability prediction, resulting in an achieved testing accuracy of  $R^2 = 0.91$ . In another similar study (Hong and Liu, 2020), a dataset of 3158 sandstone image blocks of  $100^3$  was used. This was sampled from a  $650^3$  block with a stride of 50, and then eroded and dilated to augment the dataset, with only hydraulically connected subsets used. This was used on a similarly structured 3-block CNN with 2 dense layers, achieving a testing accuracy of  $R^2 = 0.91$  over a permeability range of 10 mD to 10 D, a wide range over 3 orders of magnitude. Subsequent extrapolation of the results to a separate rock sample however, returned a lower accuracy of  $R^2 = 0.69$ . Finally a study (Alqahtani et al., 2021) of 3D regression performance for permeability prediction with a more comprehensive and wider range of pore-scale sample types was done, covering multiple sandstone and carbonate samples. The architectures used in this case were the more advanced and deeper ResNet and ResNext networks that utilize skip connections for improved performance, but this required the dataset block size was reduced to  $64^3$ . Over the testing dataset of sandstone images with permeability ranging from 10 mD to 1800 mD, an accuracy of  $R^2 = 0.87$  was achieved. Due to the broader scope of the dataset, testing on a completely unseen sandstone core-plug also achieved similarly high performance of  $R^2 = 0.86$ . Plots of the testing accuracy are shown in Fig. 29 for the 3 studies mentioned.

This review of ANN and CNN regression has focused on the  $R^2$  metric due to it being a common denominator among different studies. It is important to note that this does not provide insight into outlier error and prediction distribution, which in some cases shown, is quite high, up to

50% or more. This is observable in most of the permeability accuracy figures discussed in this section. The lack of a baseline for comparing the accuracy achieved in these studies makes it difficult to identify the most important factors in improving permeability prediction of pore-scale images with Deep Learning. A benchmark dataset would be beneficial in this regard, though a baseline metric for comparison would also suffice. Like how super resolution studies explored in previous sections of this paper use the bicubic upsample as a baseline to allow comparisons of accuracy to be made between different datasets, a similar methodology can be applied to permeability prediction. The simplest method would be a Kozeny-Carman or PNM analysis of the images in the dataset, allowing the ANN/CNN results to be compared in a more universal manner. The issue is that both methods are subject to tuning parameters that are not universally agreed upon. Regardless, major trends for improving performance are likely similar to other branches and applications of Deep Learning; network architecture, custom loss functions, and broader datasets.

Overall, permeability (and petrophysical) prediction using ANNs and CNNs show promise as surrogate models for cases where speed takes priority, and accuracy tolerance is up to 10% in general and 50% in outliers. Permeability in general is a highly uncertain parameter, and even flow solvers such as Pore Network Models and Semi Analytical Laplace Solvers show similar  $R^2$  values (for lack of a better and more commonly used metric) compared to direct flow simulation. As a surrogate model for simpler cases such as 2D cross sections of arbitrary geometry, Deep Learning regression performs with near perfect accuracy. The relationship between pore morphology and permeability in

**Objective:** Permeability of 3D Sandstones

**Source:** 3D image

**Usage:** Surrogate Model

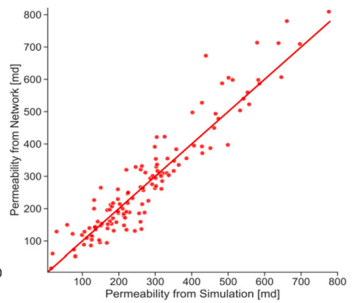
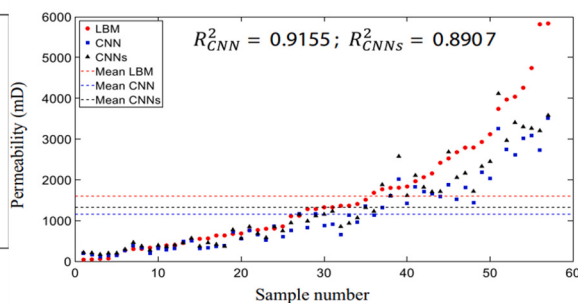
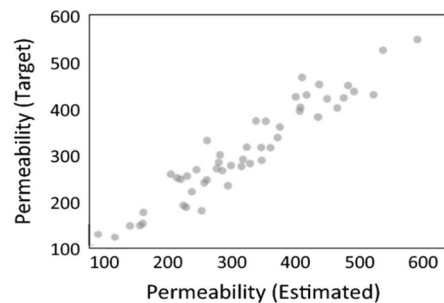


**Fig. 29.** Permeability prediction accuracy achieved with 3 different CNN regression implementations on different 3D datasets of sandstone images of different size. Reprinted with permission (Kamrava et al., 2019b; Hong and Liu, 2020; Alqahtani et al., 2021).

the complex geometries of pore-scale images remain difficult to capture even with Deep Learning. While thus far research has focussed on single-phase flow predictions of permeability, similar methodology may be applied for prediction of relative permeability curves from pore-scale images - though this remains unpublished.

#### 4.2. Deep learning in pore-scale flow simulation

While the prediction of average petrophysical properties lends itself reasonably well to approximation, with parameters such as the permeability naturally incurring uncertainty in its measurement (Chappell and Lancaster, 2007), prediction of velocity fields has been notably more difficult using CNNs. The aim in these cases is predicting steady-state flow fields from input geometries, though studies applying CNNs instead for acceleration of flow are also conducted. There have also been use-cases for CNNs that predict the conductivity field for SAS methods (Chung et al., 2020b), though this section of this paper will focus on studies that aim to predict the velocity fields. Beginning with simple 2D geometries, to complex 3D porous media, velocity field prediction has shown significant limitations in accuracy, both quantitatively and qualitatively. However, it has been shown that coupling these predictions of fluid flow (fast, limited accuracy) with direct flow simulation (slow, high accuracy) is an effective technique.

In cases of simple geometries in 2D and 3D, such as cylinders, singular spheres, and vehicle profiles (Guo et al., 2016; Hennigh, 2017; Jin et al., 2018), the accuracy is quite high, though visual discrepancies in the form of noise and velocity profile errors are common, mostly around the boundary walls of the domain. An example of such an implementation on simple geometries is shown in Fig. 30, which used a U-Net with separate decoders for each output field (Ribeiro et al., 2020). The sample domain shows boundary errors and errors in regions of high velocity in the form of convolutional artefacts. The existence of these errors in such simple 2D geometries using an advanced CNN such as this U-Net implementation suggests that efforts to predict flow fields in more complex porous media will suffer from increasing reductions in accuracy without some form of intervention or improvement in data or network.

In studies applying CNNs to more complex pore-scale domains, the accuracy degrades significantly. Discrepancies in the local velocity fields become increasingly large as the domain becomes more complex, with more pore throats and regions of high velocity causing predictions to incorrectly choose the principal flow paths and incorrectly predict local velocity magnitudes. This problem is present both in CNN implementations that are trained to advance simulations (Hennigh, 2017), and in implementations that are trained to directly predict steady-state flow fields (Santos et al., 2020; Wang et al., 2020c). In this section, the implementations of flow field prediction that this paper will focus on are in order: LatNet (Hennigh, 2017), Poreflow-Net (Santos et al., 2020), and ML-LBM (Wang et al., 2020c). All 3 of these examples use LBM to train their CNNs.

LatNet is unique in the sense that it was not simply designed to predict steady-state flow fields from input images. Rather, it was intended to take in flow fields at some arbitrary point in the simulation, and advance said simulation faster than otherwise possible. After training LatNet on 2D and 3D synthetic geometries and 2D vehicular profiles, testing of the network revealed that reasonable approximations of flow fields are obtained with LatNet. Clear discrepancies were visible in regions of high vorticity and regions of high velocity magnitude, placing the visual accuracy of the results in question, and plots of the cross-sectional flux and other quantitative metric showed that there is difficulty in capturing the finer-scale trends in the flow fields (Fig. 31).

Poreflow-Net takes an input image and predicts the steady-state velocity magnitude. The network takes the form of a modified U-Net with 4 input branches, as it has prolific use of pre-computed input features, most notably, the Time-of-Flight (TOF) (Hassouna and Farag, 2007) field calculated over the entire domain in order for the network to more effectively predict velocity fields in a patchwise method. Calculating the TOF scales comparably to solving the elliptic diffusion equation with the finite difference method (Wang et al., 2020c), and as such, was relatively computationally intensive as a pre-processing step. Nonetheless, the objective of capturing information regarding geometry unseen to local image patches allowed Poreflow-Net to be more effective on larger domains (initial computation of TOF on large domains

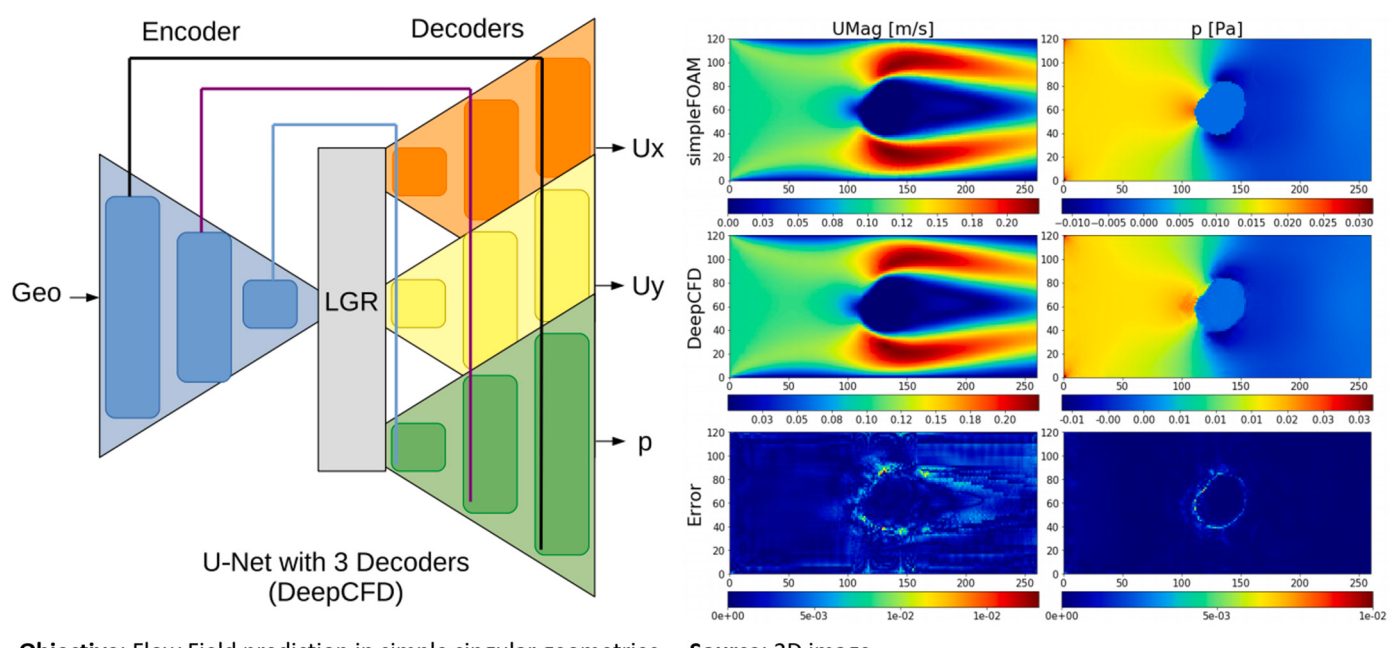
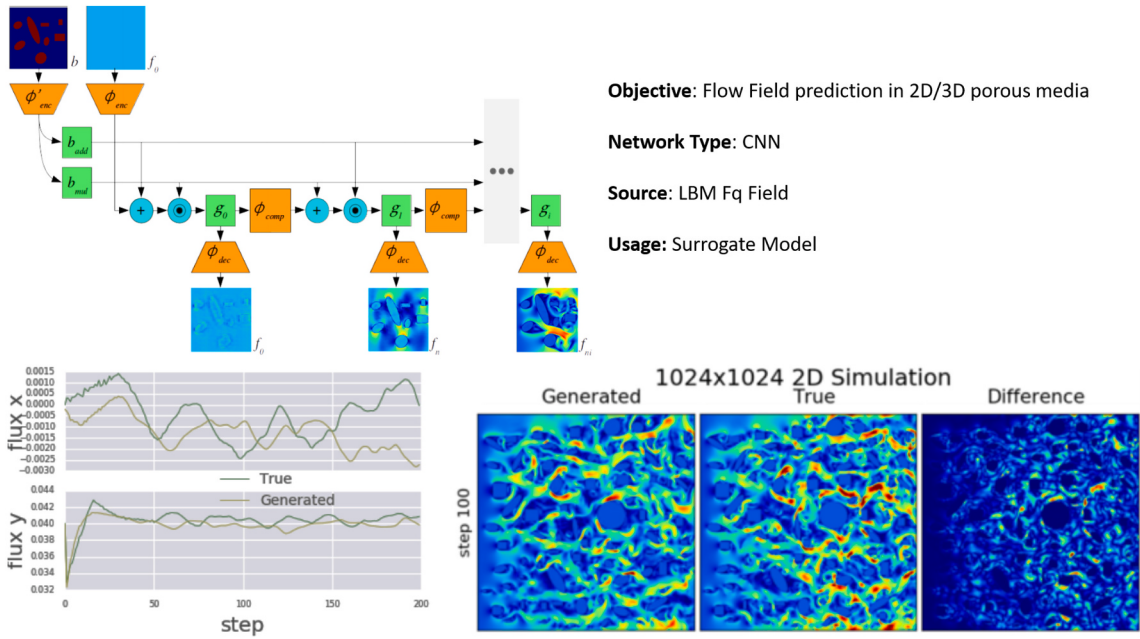


Fig. 30. Network design of this particular field predictor, with decoders for each parameter. The results show errors manifesting at the boundaries, and general convolutional artefacts in the field. Reprinted with permission (Ribeiro et al., 2020).



**Fig. 31.** LatNet architecture, visualization, and accompanying flux profiles. Visual errors show that high velocity pores incur higher errors, which result in inconsistent flux profiles. Reprinted with permission (Hennigh, 2017).

notwithstanding), as it can be used sequentially on local blocks. Because only the scalar velocity field is predicted, Poreflow-Net acts as a visual aid for velocity field estimation and for permeability prediction, similar in scope and achieved accuracy to regression models discussed previously. Errors in velocity field prediction in Poreflow-Net shown in Fig. 32 were not highlighted, rather, the permeability prediction was shown to be comparable to studies using CNN Regression models, with the added bonus of a field prediction as a visual aid.

ML-LBM aims to take an input image and predict the velocity vector field in all principal directions. Much like results obtained by LatNet and

Poreflow-Net, ML-LBM similarly suffered from unacceptably high inaccuracy in geometrically complex porous media. Because it does not attempt to include global-to-local information such as the TOF as input unlike Poreflow-Net, it must be used on an entire domain at once, limiting its computational efficiency. Similarly high accuracy was achieved for permeability estimation compared to Poreflow-Net and regression models discussed in the previous section, with an  $R^2$  value of 0.99+ in 2D and 0.97+ in 3D synthetic porous media. However, cross-sectional flux discrepancies seen in LatNet, and velocity magnitude/location prediction errors seen in both LatNet and Poreflow-Net are all

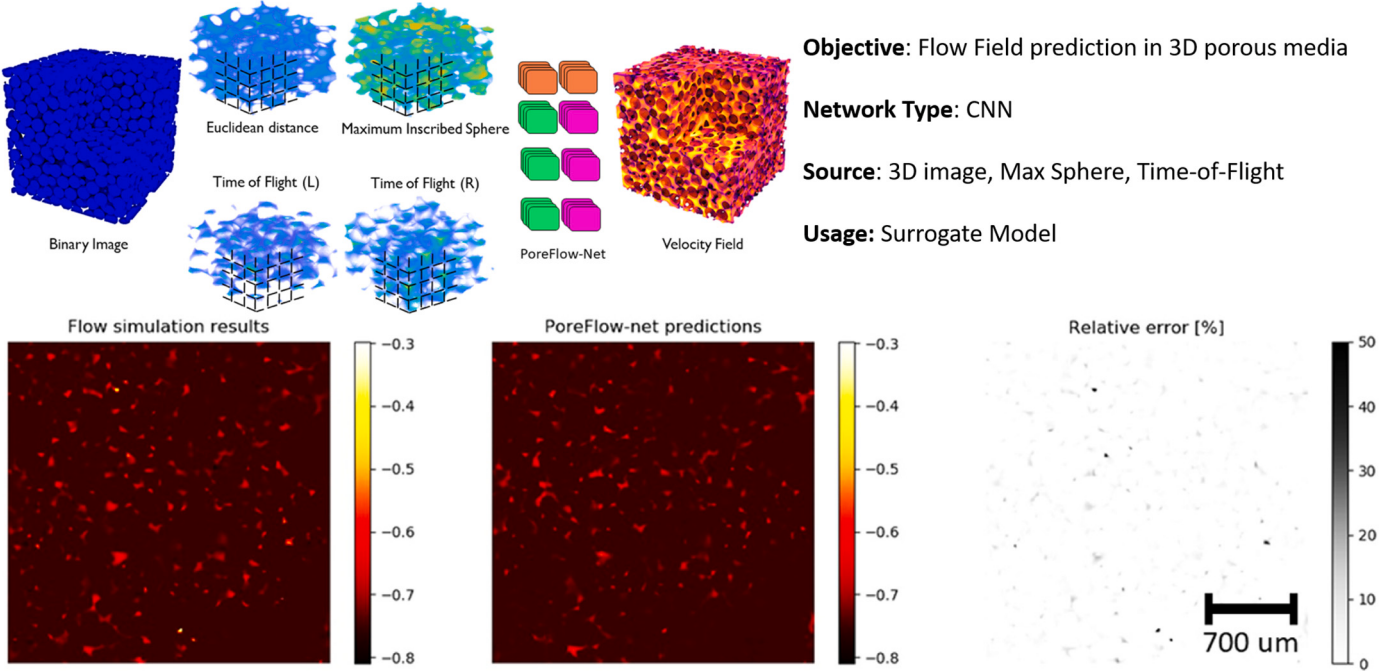


**Fig. 32.** Poreflow-Net design which uses the Time-of-Flight (related to the formation factor and tortuosity) as input, and visualization. Predicted velocity magnitudes show similar issues of incorrect velocity prediction in some pores. Reprinted with permission (Santos et al., 2020).

present in ML-LBM, and this error was explored over a wider range geometric complexities. This error was furthermore quantified in a clearer fashion by using the predicted fields as underlying velocity fields for solute transport, showing as expected, that predictions of velocity fields using CNNs are unsuitable as replacement models when the velocity field is required. As such, an efficient Machine Learning aided flow simulation method was introduced as ML-LBM, whereby combining predictions of fluid flow (fast, limited accuracy) with direct flow simulation (slow, high accuracy) was shown to accelerate direct flow simulation to steady-state conditions with an order of magnitude less compute time. These features of ML-LBM are shown in Fig. 33.

Using Deep Learning to accelerate flow simulation to steady-state in complex pore structures shows promise as a technique to push the boundaries of fluid flow modeling. However, in complex geometries using the implementations introduced thus far, even when a good result is achieved in permeability estimation (down to less than 1% error) by the prediction of velocity fields, (comparable to results achieved by regression networks), the underlying velocity field is not guaranteed to possess the necessary voxel-by-voxel accuracy required to use these velocity fields for further analysis. Advection dominant solute transport in relatively high Peclet Numbers (near the numerical diffusion limit of Explicit Finite Volume Methods) shows that local velocity errors are too large near walls and tight throats to be directly useful. In simpler geometries, this estimate can be used as-is for permeability estimation and to garner an approximate understanding of the flow paths. In complex geometries that CNNs examined in this section struggle with, the predictions can be used as preconditioned input in direct simulation to reach a fully accurate result in a fraction of the compute time. While thus far research has focused on single-phase flow/velocity field predictions, a similar methodology may be applied for prediction of phase distributions during multiphase flow from pore-scale images - though this remains unpublished.

## 5. Conclusions

This paper provides a critical review of the primary Deep Learning techniques (ANN, CNN, GAN) that are used in the workflow of pore-scale imaging and modeling. Image processing, segmentation, and petrophysical modeling have all been improved by the use of Deep Learning. Significant advances in accuracy and performance have been achieved in studies published so far with rapid progress in the last three years, but many challenges remain.

Image segmentation and mineral identification in pore-scale images becomes less biased towards user input, while also being more physically accurate with CNNs. Segmenting noisy, low quality images to achieve segmentation accuracy typically obtainable only from segmenting a higher quality image becomes possible with datasets that map low quality to high quality micro-CT, micro-CTSEM, or micro-CT-QEMSCAN data. The further advancement of pore-scale image segmentation should focus on obtaining SEM-quality multi-mineral segmentation from noisy, low quality gray-scale images (beyond human capabilities), but a major issue of dataset availability restricts the applicability of these models (see Section 6.1), but could be mitigated with stochastic generation of data (Karimpouli and Tahmasebi, 2019), synthetic generation of data (Ihle et al., 2019), or domain transfer learning with CycleGANs.

Image processing and enhancement (noise, blur, resolution, texture) has led to the implementation of the SRCNN for noise reduction, deblurring, and edge recovery, followed by the SRGAN for edge and texture recovery, and finally the SRCycleGAN (and Cyclein-CycleGAN) for flexibility with unpaired real datasets. These techniques can provide physically accurate pore-scale images with a resolution-FOV surpassing hardware limits, lowering the requirements for generating high resolution samples with the dimensions of core samples used for laboratory analysis. This is particularly important for two-phase flow where flow dynamics and phase distributions are driven by non-local forces

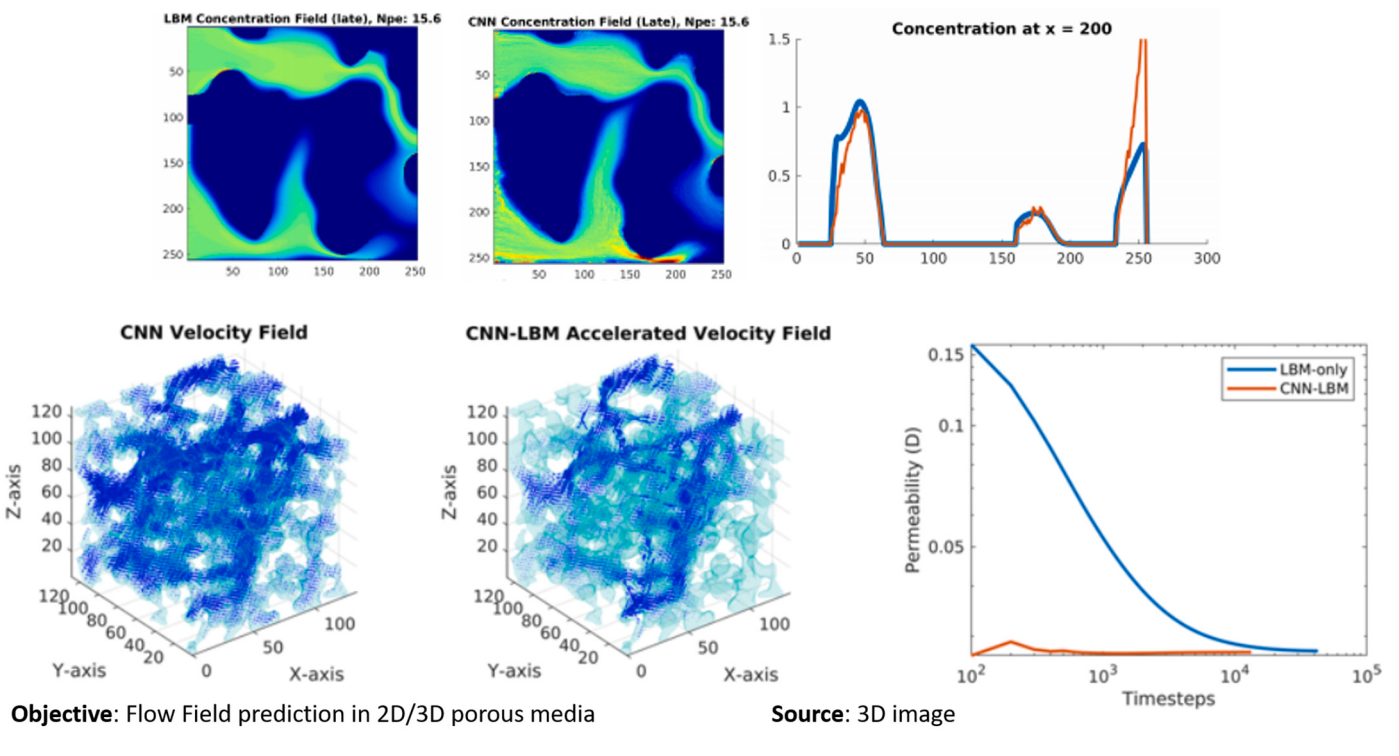


**Fig. 33.** Top: A comparison of solute transport simulations performed using velocity fields from LBM and ML-LBM, showing the issue with local velocity errors present in LatNet, Poreflow-Net, and ML-LBM. Bottom: Coupling ML-LBM predictions to an LBM implementation allows accelerated computation of steady-state fields at full simulation accuracy. Reprinted with permission (Wang et al., 2020c).

that extend beyond the typical boundaries of images used in digital rock studies (Armstrong et al., 2016). Heterogeneity and under-resolved fractures in coals, carbonates, and shales, and other multi-scale features where a larger FOV is required at high resolution to achieve a representative elementary volume (Menke et al., 2018) also become more accessible. Another challenge is how to practically use super-resolved images, as if the resolution of a typical scanned image ( $2000^3$ ) is increased by a factor of 8, a  $16,000^3$  image results. Limitations on simply importing and manipulating the image would result in a real user likely taking smaller FOV subsamples in order of  $2000^3$  for analysis. While these computing limitations naturally alleviate over time with technological advancements (see Section 6.5), more innovative methods for presenting/analyzing multiresolution images (multi-scale simulation for example with domain decomposition (Wang et al., 2019b; Rabbani et al., 2019) or voxel agglomeration/meshing (Chung et al., 2020a; Mostaghimi et al., 2015)) may assist in a smarter way than by simply increasing the amount of voxels throughout the whole 3D image.

While datasets exploring these super resolution enhancements have been applied to shales (Kamrava et al., 2019a), coals (Wang et al., 2020a), and carbonates (Wang et al., 2020a), studies using these resulting images for analysis are under-represented in the available literature. Aside from advances in network implementations for real image super resolution (Zhang et al., 2020), some major aspects in super resolving pore-scale images that should be properly explored are the integration of multiple image sources for super resolution and quality enhancement, and higher resolution factors ( $16\times$  and  $32\times$ ) in super resolution that rely more heavily on stochastic GAN generation of texture. Some examples implementing these points would be SEM-micro-CT super resolution (0.1–1  $\mu\text{m}$  to 1–10  $\mu\text{m}$ ), or SEM to Positron Emission Tomography (PET) (0.1–1  $\mu\text{m}$  to 10–100  $\mu\text{m}$ ).

Synthetic image generation/extrapolation using GANs to reconstruct segmented (or gray-scale) porous media has allowed faster generation of representative synthetic examples, shown to be reliable and verifiable with morphology and physical modeling. Instead of a fully stochastic approach (random vector to 3D image), 2D slice to 3D image generation and 3D to 3D image generation (which is analogous to super resolution, albeit with extreme scale factors) are key topics of continued study.

Petrophysical prediction in complex porous media using ANNs and CNNs acts effectively as a surrogate model when the priority is compute speed, and accuracy tolerance is relatively wide. Permeability is a highly uncertain parameter, and traditional estimation methods (faster than direct simulation) such as Pore Network Models and Semi Analytical Laplace Solvers show similar accuracy (up to 20% error) compared to direct flow simulation. Furthermore, for simpler cases such as 2D cross-sections of arbitrary geometry, Deep Learning regression performs with near perfect accuracy. Given the loss in accuracy in more complex geometries, the relationship between pore morphology and permeability in pore-scale images remains difficult to capture even with Deep Learning.

Prediction of flow fields (as opposed to petrophysical prediction of average values) would aid the analysis of complex transport phenomena involving dispersion, advection, and reactions. Using Deep Learning to accelerate flow simulation by predicting flow fields has shown similar accuracy to petrophysical prediction in permeability estimation. However, the underlying velocity field tends to be highly error-prone lacking the necessary voxel-by-voxel accuracy required for further analysis. For example, simulations of solute transport shows that velocity field errors are too high to be directly useful in complex porous media, but are acceptable in simpler geometries, where this estimate can be used as-is. In complex geometries that CNNs struggle with, the predictions can be used as preconditioned input in direct simulation to reach a fully accurate result in a fraction of the compute time. While these CNN based methods of petrophysical prediction have thus far been based on single-phase flow, there is immediate potential for extension of these CNNs into predictions of multiphase flow physics, such as steady-state two-phase flow for relative permeability, residual CO<sub>2</sub> and Hydrogen gas trapping

predictions.

The use of Deep Learning for pore-scale imaging and modeling will likely continue becoming increasingly pervasive, as potential exists to improve all aspects of the data-driven workflow, with higher image quality, automated processing, and faster simulations. However, there exists a number of difficult challenges that impede the widespread usability of Deep Learning in the pore-scale, which are detailed below.

## 6. Future challenges

Current limitations and challenges, including dataset acquisition and synthetic training, extrapolative potential, accuracy loss from soft computing, and the computational cost of 3D Deep Learning are discussed in the following sections.

### 6.1. Dataset availability and benchmarks

One of the main challenges in Deep Learning (for general purposes) is the availability of training data. Pore-scale images are generated in specialist laboratories and until recently, have mostly been held in private repositories. The introduction of the Digital Rocks Portal (Esteva and Hanlon, 2015) has facilitated some of the broader studies outlined in this paper (Wang et al., 2020a; Wang et al., 2019a), but most of the deep learning studies performed at the pore-scale have been with private datasets, making standardization, comparisons, and advancements difficult. The Digital Rocks Portal and other public domain repositories should be key resources for deep learning.

In pore-scale imaging and modeling, this issue is especially problematic as there are very few available examples of high resolution micro-CT and SEM images of appropriate configuration. Many super resolution CNN studies have used synthetically generated examples which can cause a loss in accuracy in testing and use. Segmentation by CNN studies have been limited to specific rock types and specific mineral configurations from lacking a widely labeled universal dataset and a general lack of SEM slices which are experimentally difficult to obtain. On the other hand, petrophysical and flow field prediction with neural networks suffers less from data availability due to 3D CNN resource limitations with no hardware imaging requirements (purely synthetic data generation is possible).

In the task of super resolution image interpolation, the major issue in terms of dataset is the need for registered Low Resolution (LR) and High Resolution (HR) images for SRCNN and SRGAN implementations. The mapping of real LR images to real HR images offers a better representation of the expected levels of noise and blur in real images (Chen et al., 2020; Niu et al., 2020; Janssens et al., 2020), compared to those used in synthetic training with downsampled images with augmented blur and noise (Wang et al., 2019a; Wang et al., 2020a). Since data pairing is not required for SRCycleGANs, the available data that can be used for training and testing becomes much broader but performance is reduced due to a general loss of texture due to both the increased difficulty in network minimization and the total variation loss function that is used as a crutch to remove convolution artefacts caused by poor minimization. Multiple possibilities exist for improving this issue, including a) synthetic datasets proven to represent real images, b) acquisition of more registered LR-HR images, and c) improvements in unpaired (e.g. cycleGAN) super resolution performance.

Improving segmentation accuracy with CNNs has mostly been limited by a lack of high quality data. While binary segmentation of rock images is widely available, with numerous publicly available examples, the focus of CNN segmentation has been on mapping lower quality gray-scale images to segmentations obtained from much higher quality images i.e. SEM images (Niu et al., 2019; Wang et al., 2021), and/or multi-mineral segmentation (Karimpouli and Tahmasebi, 2019; Niu et al., 2019; Wang et al., 2021). Both of these types of data are much rarer, with sparse examples available for training. SEM slices are difficult to experimentally obtain, and only represent a single 2D slice of a single

example, while multi-mineral segmentations are visually impossible from a gray-scale image, requiring complicated experimental apparatus or specialized imaging equipment that also limit the breadth of available data. Aside from simply acquiring more imaging data, stochastic generation of representative data can be beneficial (Karimpouli and Tahmasebi, 2019), unpaired training for domain transfer similarly may mitigate this issue, and simulated micro-CT scans may be particularly useful if they reproduce the X-ray physics that lead to imaging artefacts (Dhaene et al., 2015) which potentially allows a user to create a realistic ground-truth dataset specific to their problem if these simulators are sufficiently accurate.

Aside from the difficulties in simply obtaining enough data for some tasks such as super resolution and segmentation, a problem that plagues all aspects of pore-scale deep learning is the lack of specifically designed standard benchmark datasets. Some preliminary efforts have been made to create such datasets (Wang et al., 2019d; Wang et al., 2019c), but this has not spanned all tasks such as segmentation and petrophysical prediction. Some benchmark datasets are available for flow simulation in porous media (Saxena et al., 2017), but have not yet been applied to deep learning applications. Efforts should be made to create such datasets that annually evolve with advancements in deep learning (for instance, the NTIRE datasets from 2017 and 2020 are significantly different (Agustsson and Timofte, 2017; Zhang et al., 2020)).

## 6.2. Standardization of accuracy measures

In all tasks outlined in this review, standardization of performance measures is an issue, though it affects some tasks more than others. Ideally, the only variable being measured in a study of deep learning performance would be the performance of the network itself. This can only be achieved if all studies used the same dataset (see previous section) and the same set of performance metrics.

In super resolution studies the PSNR is used as the standard pixelwise accuracy, and comparison to conventional bicubic upsampling is also performed. Specifically to pore-scale imaging super resolution though, other metrics of accuracy have been introduced, such as the GLCM, gray-scale measures (Kamrava et al., 2019a; Chen et al., 2020), and petrophysical measures (Wang et al., 2020a; Niu et al., 2020; Janssens et al., 2020) (though these petrophysical measures require segmentation which is a source of bias).

In segmentation, pixelwise accuracy is commonly used (Kamrava et al., 2019a), and some measures of boundary accuracy are also applicable, such as falsity (Wang et al., 2021) and distance weighting. Petrophysical measures of permeability and connectivity are also a natural standard to use (Wang et al., 2021; Niu et al., 2019; Mosser et al., 2017a), which can also be applied to porous structure generation/extrapolation (Mosser et al., 2017a).

In petrophysical predictions of permeability, the  $R^2$  value is commonly the only measure used, and alternatives have not presented themselves. Perhaps, like comparing super resolution with conventional bicubic interpolation, permeability predictions can be compared not only against their ground truth  $R^2$ , but also against the performance achievable with conventional methods such as Kozeny-Carman (Wu et al., 2018), simple correlations (Arns et al., 2005; Richesson and Sahimi, 2019; Xu and Yu, 2008), Pore Network Models (Dong et al., 2008), and Laplace Methods (Chung et al., 2019).

In the case of flow field prediction, some studies have focused on visual analysis and pixelwise error (Ribeiro et al., 2020), some have focused on permeability error (Santos et al., 2020), others have focused on flux profile error (Hennigh, 2017; Wang et al., 2020c), while some have investigated the solute transport error (Wang et al., 2020c). Of these, the measures that are most meaningful for predictions of fluid flow would be the flux profile error and solute transport profile error, as the purpose of flow field prediction encompasses not only permeability predictions but also local velocity fields for transport phenomena analysis.

## 6.3. Extrapolative potential

Extrapolative potential is somewhat of a misconception in Deep Learning, though many studies reviewed in this paper attempt to apply some degree of extrapolation (testing network performance with samples outside the scope of the training data) to their trained networks (Wang et al., 2019a; Wang et al., 2020a; Hong and Liu, 2020; Alqahtani et al., 2021; Wu et al., 2018; Santos et al., 2020). In some cases, acceptable results are obtainable when testing a network on inputs that are not only unseen, but also contain features unlearned by the network. Examples include testing a super-resolution network by passing HR images into it to generate HR-SR images (Wang et al., 2019a; Wang et al., 2020a), or testing permeability prediction on sandstone images with a network trained only on sphere packs (Hong and Liu, 2020; Santos et al., 2020). The accuracy obtained in these cases is naturally lower, but the idea of using trained networks in an extrapolative manner does not always make sense. For example, in segmentation (and categorization in general), mapping gray-scale images to multiple mineral types is dependent on both the absolute and relative gray-scale intensities, and the morphology and shape of features in the image. Attempting extrapolation with external samples to segment images of a completely different type or contrast-level without appropriate training would be akin to attempting to identify images of dogs with a network trained on images of cats. One promising method for partially dealing with this issue is the use of domain transfer via CycleGANs to transform images of the same rock-type but scanned under different conditions (e.g. Bentheimer sandstone scanned using a laboratory instrument as compared to at a Synchrotron or just scanned separately on different occasions on the same hardware). This would potentially alleviate issues with extrapolation of similarly featured samples with different levels of gray-scale intensity distributions and texture levels.

In general, even for cases where extrapolation may be somewhat successful (and even useable in the case of super resolution (Wang et al., 2019a)), it is more prudent to evaluate network performance within a reasonably similar scope. Analogous to the simple case of non-linear curve fitting, performance outside the scope of example data is unpredictable and not guaranteed to be representative. Another such example would be attempting a 2D–3D GAN based extrapolation (Feng et al., 2020) of carbonate images using a network trained only on sandstone images, by passing a 2D carbonate slice into the network. The result would just be a sandstone-like image. This once again highlights the fundamental importance of dataset quality and scope.

## 6.4. Accuracy limitations of deep learning

Deep Learning is inherently limited in the accuracy that can be achieved, always falling short of ground truth examples in some way. Advances in the achievable accuracy of Deep Learning has come primarily through improvements in neural network architecture, of which, the most influential would be the ResNet skip connection (He et al., 2015b) and the GAN (Goodfellow et al., 2014). The evolution of Deep Learning in super resolution in particular is a good example of this advancement in achieved accuracy, with the original SRCNN (Dong et al., 2016a) replaced by EDSR (Lim et al., 2017) (based on ResNet (He et al., 2015b)), and then augmented with GANs to form the popular SRGAN and its modern ESRGAN variant (Ledig et al., 2017; Wang et al., 2018). Other factors include the complexity of the problem (e.g. binary vs multi-mineral segmentation) and the complexity of the data (e.g. real sandstone vs. sphere packs).

In all tasks outlined in this paper, accuracy limits exist i.e. texture in super resolution, physical accuracy in segmentation, morphological accuracy in synthetic image generation, petrophysical prediction accuracy in regression, and velocity field accuracy in flow field prediction (see the respective sections). In some cases, this limitation is acceptable or even beneficial, such as is the case in super resolution, whereby the loss of texture but sharply recovered edges serve to simplify

segmentation (Wang et al., 2019a), or in texture regeneration (Wang et al., 2020a) or synthetic image generation (Mosser et al., 2017a), whereby the generated image is stochastic, thus widening accuracy tolerances. In other cases, accuracy limitations can be debilitating to the point where the objective for learning is not adequately met, such as is the case in flow field prediction in complex geometries (see Section 4.2), where permeability prediction is similarly accurate compared to regression models (see Section 4.1), but the velocity fields important for transport phenomena analysis, the primary objective of flow field prediction, are unusable without correction.

Finally, it is important to emphasize the need for testing and validation metrics to focus on physical accuracy in pore-scale images. Due to the pixel/voxel based nature of pore-scale imaging tasks (super resolution, segmentation), it is simple and natural to use the default metrics of accuracy, which measure the pixel/voxelwise error between generated results and their ground truth. On the other hand, physical accuracy measurement is typically performed with topological analysis and flow simulation (Wang et al., 2020a; Niu et al., 2019; Niu et al., 2020; Wang et al., 2021; Janssens et al., 2020), and has been shown to provide greater insight and sensitivity to the network implementation. The preservation of topological accuracy and petrophysical accuracy should be equally prioritized with pixel/voxelwise accuracy, since network architectures achieving a high accuracy do not necessarily produce a physically accurate result.

### 6.5. Scalability of 3D deep learning

Deep Learning finds most of its use-cases in the realm of 2D photographic images or videos of natural photographic scenes (Yang et al., 2019), making their use for 2D deep learning on pore-scale imaging relatively straightforward, as seen in some of the simpler studies reviewed in this paper. As 3D pore-scale imaging continues to advance in its capabilities, the use of 3D-to-3D methods of deep learning should similarly grow beyond use on thin-sections and 2D slices. Volumetric 3D images such as those obtained from micro-CT imaging are significantly larger, and scale to the cube of the length, and a typical micro-CT core plug would require over 64GB of CPU RAM to even perform simple manipulations (a  $2000^3$  16-bit image would take up 16GB, and if double precision, would take up 64GB). Deep Learning has mainly been facilitated by the performance of GPUs, and since GPU parallelization for Deep Learning is usually performed by splitting apart the batch dimension and taking averages of the computed gradients, it is not conventionally possible to distribute a large 3D volume among multiple

GPUs along the x, y, and z axes and not typically supported by software. Furthermore, training time dramatically increases when using the same architecture due to increased model parameters in 3D, and memory access speed limitations. This problematic scaling of memory requirements is further exacerbated in Deep Learning by the lower memory capacities of GPUs compared to CPU memory, and the depth/complexity of the network. Modern GPUs capable of reasonable deep learning performance hold anywhere from as low as 8GB (RTX 2070) to up to 96GB (Ampere A100) of memory, which is dwarfed by CPUs which can reach 2 TB and beyond in RAM. Other than GPU memory, GPU performance plays a major role in the time taken to train a network, and 32-bit floating point operations per second (FP32) in GPUs have increased by power-law over the past decade, by approximately 26% per year (Fig. 34 of GPU performance measured in 32-bit Tera-Floating Point Operations per Second (TFLOPS FP32) vs year).

Exploiting the ability for fully convolutional networks to be used on inputs of any size allows training to be performed on small subsamples, and testing/deployment on larger individual images using CPU resources. This is a valid strategy, applicable without loss of accuracy to tasks with local influences such as super resolution and segmentation (Wang et al., 2019a; Wang et al., 2021), but tends to produce increasing errors in physics prediction due to the presence of non-local forces that affect the result in subsections, unseen to a network if trained with smaller blocks (Santos et al., 2020). Furthermore, regression type problems are not fully convolutional due to the presence of dense layers at the end, restricting the training block size to equal the testing block size, which limits the flexibility and usability of the trained model (Alqahtani et al., 2021).

It is for these reasons of memory usage, resource limits, and network design, why super resolution and/or segmentation is trained using mini-batches (Wang et al., 2020a; Wang et al., 2021) (randomly cropped subsections), and why petrophysical regression and flow field estimation tasks in 3D are limited to around  $100^3$  blocks (Hong and Liu, 2020; Alqahtani et al., 2021; Kamrava et al., 2019b), with most network architectures being relatively shallow 3D CNNs. Improvements in hardware will naturally increase the size of feasible 3D Deep Learning tasks, and networks designed specifically with significant compression (Hennigh, 2017) may also alleviate some of these scalability issues.

### Declaration of Competing Interest

The authors declare that they have no known competing financial interests or personal relationships that could have appeared to influence

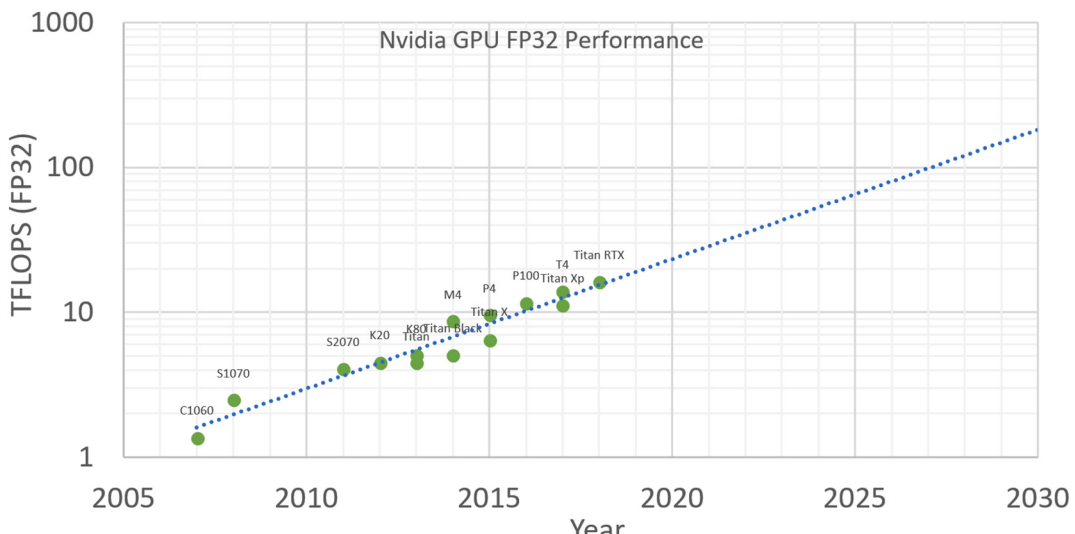


**Fig. 34.** GPU performance over time. Limitations in the physics of semiconductors aside, GPU performance is expected to continue to grow, facilitating the continued growth of deep learning applications past current limitations in memory size and training times for the large domains in pore-scale imaging and modeling.

the work reported in this paper.

## References

- Agustsson, E., Timofte, R., 2017. Ntire 2017 challenge on single image super-resolution: dataset and study. In: Proceedings of the IEEE Conference on Computer Vision and Pattern Recognition Workshops, pp. 126–135.
- Ahmadi, M.A., Ebadi, M., Shokrollahi, A., Majidi, S.M.J., 2013. Evolving artificial neural network and imperialist competitive algorithm for prediction oil flow rate of the reservoir. *Appl. Soft Comput.* 13 (2), 1085–1098.
- Akai, T., Alhammadi, A.M., Blunt, M.J., Bijeljic, B., 2019. Modeling oil recovery in mixed-wet rocks: Pore-scale comparison between experiment and simulation. *Transp. Porous Media* 127, 393–414.
- Alexander, M., Pratiwi, Harefa, J., Nanda, S., 2015. Mammograms classification using gray-level co-occurrence matrix and radial basis function neural network. *Procedia Comp. Sci.* 59, 83–91. International Conference on Computer Science and Computational Intelligence (ICCSI 2015).
- Alpak, F., Berg, S., Zacharoudiou, I., 2018. Prediction of fluid topology and relative permeability in imbibition in sandstone rock by direct numerical simulation. *Adv. Water Resour.* 122, 49–59.
- Alqahtani, N., Alzubaidi, F., Armstrong, R.T., Swietojanski, P., Mostaghimi, P., 2020. Machine learning for predicting properties of porous media from 2d x-ray images. *J. Pet. Sci. Eng.* 184, 106514.
- Alqahtani, N., Chung, T., Wang, Y.D., Armstrong, R.T., Swietojanski, P., Mostaghimi, P., 2021. Flow-Based Characterization of Digital Rock Images Using Deep Learning. *SPE Journal*.
- Andrä, H., Combaret, N., Dvorkin, J., Glatt, E., Han, J., Kabel, M., Keehm, Y., Krzikalla, F., Lee, M., Madonna, C., Marsh, M., Mukerji, T., Saenger, E.H., Sain, R., Saxena, N., Ricker, S., Wiegmann, A., Zhan, X., 2013. Digital rock physics benchmarks—part i: Imaging and segmentation. *Comput. Geosci.* 50, 25–32. Benchmark problems, datasets and methodologies for the computational geosciences.
- Ar Rushod, I., Alqahtani, N., Wang, Y.D., Shabannejad, M., Armstrong, R., Mostaghimi, P., et al., 2020. Segmentation of x-ray images of rocks using deep learning. In: SPE Annual Technical Conference and Exhibition. Society of Petroleum Engineers.
- Arganda-Carreras, I., Kaynig, V., Rueden, C., Eliceiri, K.W., Schindelin, J., Cardona, A., Sebastian Seung, H., 2017. Trainable Weka Segmentation: a machine learning tool for microscopy pixel classification. *Bioinformatics* 33, 2424–2426, 03.
- Armstrong, R.T., McClure, J.E., Berrill, M.A., Rücker, M., Schlüter, S., Berg, S., 2016. Beyond darcy's law: The role of phase topology and ganglion dynamics for two-fluid flow. *Phys. Rev. E* 94 (4), 043113.
- Armstrong, R.T., McClure, J., Berrill, M., Rücker, M., Schlüter, S., Berg, S., et al., 2017. Flow regimes during immiscible displacement. *Petrophysics* 58 (01), 10–18.
- Arns, C.H., Knackstedt, M.A., Martys, N.S., 2005. Cross-property correlations and permeability estimation in sandstone. *Phys. Rev. E* 72 (4), 046304.
- Badrinarayanan, V., Kendall, A., Cipolla, R., 2015. Segnet: A Deep Convolutional Encoder-decoder Architecture for Image Segmentation. *Arxiv*.
- Becker, M., Jardine, M., Miller, J., Harris, M., 2016. X-ray computed tomography – a geometallurgical tool for 3d textural analysis of drill core? In: The Third AusIMM International Geometallurgy Conference (GeoMet).
- Berg, S., Rücker, M., Ott, H., Georgiadis, A., Van der Linde, H., Enzmann, F., Kersten, M., Armstrong, R., De With, S., Becker, J., et al., 2016. Connected pathway relative permeability from pore-scale imaging of imbibition. *Adv. Water Resour.* 90, 24–35.
- Bijeljic, B., Muggeridge, A.H., Blunt, M.J., 2004. Pore-scale modeling of longitudinal dispersion. *Water Resour. Res.* 40 (11).
- Bijeljic, B., Mostaghimi, P., Blunt, M.J., 2011. Signature of non-fickian solute transport in complex heterogeneous porous media. *Phys. Rev. Lett.* 107 (20), 204502.
- Blunt, M.J., 2017. Multiphase Flow in Permeable Media: A Pore-Scale Perspective. Cambridge University Press.
- Blunt, M.J., Jackson, M.D., Piri, M., Valvatne, P.H., 2002. Detailed physics, predictive capabilities and macroscopic consequences for pore-network models of multiphase flow. *Adv. Water Resour.* 25 (8), 1069–1089.
- Blunt, M.J., Bijeljic, B., Dong, H., Gharbi, O., Iglesias, S., Mostaghimi, P., Paluszny, A., Pentland, C., 2013. Pore-scale imaging and modelling. *Adv. Water Resour.* 51, 197–216 (35th Year Anniversary Issue).
- Boek, E.S., Venturoli, M., 2010. Lattice-boltzmann studies of fluid flow in porous media with realistic rock geometries. *Comput. Math. Appl.* 59 (7), 2305–2314.
- Bultreys, T., Hoorebeke, L.V., Cnudde, V., 2015. Multi-scale, micro-computed tomography-based pore network models to simulate drainage in heterogeneous rocks. *Adv. Water Resour.* 78, 36–49.
- Bultreys, T., De Boever, W., Cnudde, V., 2016. Imaging and image-based fluid transport modeling at the pore scale in geological materials: A practical introduction to the current state-of-the-art. *Earth Sci. Rev.* 155, 93–128.
- Chappell, N.A., Lancaster, J.W., 2007. Comparison of methodological uncertainties within permeability measurements. *Hydrolog. Processes.* 21 (18), 2504–2514.
- Chen, L., Zhang, L., Kang, Q., Viswanathan, H.S., Yao, J., Tao, W., 2015. Nanoscale simulation of shale transport properties using the lattice boltzmann method: permeability and diffusivity. *Sci. Rep.* 5 (1), 1–8.
- Chen, H., He, X., Teng, Q., Sheriff, R.E., Feng, J., Xiong, S., Feb 2020. Super-resolution of real-world rock microcomputed tomography images using cycle-consistent generative adversarial networks. *Phys. Rev. E* 101, 023305.
- Chung, T., Wang, Y., M. P., and A. RT., 2019. Approximating Permeability of Micro-Ct Images Using Elliptic Flow Equations. *SPE Journal*.
- Chung, T., Wang, Y.D., Armstrong, R.T., Mostaghimi, P., 2020a. Voxel agglomeration for accelerated estimation of permeability from micro-ct images. *J. Pet. Sci. Eng.* 184, 106577.
- Chung, T., Wang, Y.D., Armstrong, R.T., Mostaghimi, P., 2020b. Cnn-Pvfs: Integrating Neural Networks and Finite Volume Solvers to Accelerate Flow Simulation on Pore Space Images. *Transport in Porous Media*.
- Cnudde, V., Boone, M.N., 2013. High-resolution x-ray computed tomography in geosciences: A review of the current technology and applications. *Earth Sci. Rev.* 123, 1–17.
- Coenen, J., Tchouparova, E., Jing, X., 2004. Measurement parameters and resolution aspects of micro x-ray tomography for advanced core analysis. In: Proceedings of International Symposium of the Society of Core Analysts.
- Culligan, K., Wildenschild, D., Christensen, B., Gray, W., Rivers, M., 2006. Pore-scale characteristics of multiphase flow in porous media: a comparison of air–water and oil–water experiments. *Adv. Water Resour.* 29 (2), 227–238. Experimental Hydrology: A Bright Future.
- Delerue, J.-F., Lomov, S.V., Parnas, R., Verpoest, I., Wevers, M., 2003. Pore network modeling of permeability for textile reinforcements. *Polym. Compos.* 24 (3), 344–357.
- Dhaene, J., Pauwels, E., De Schryver, T., De Muynck, A., Dierick, M., Van Hoorebeke, L., 2015. A realistic projection simulator for laboratory based x-ray micro-ct. *Nucl. Instrum. Methods Phys. Res., Sect. B* 342, 170–178.
- Dong, H., Fjeldstad, S., Alberts, L., Roth, S., Bakke, S., Ören, P.-E., et al., 2008. Pore network modelling on carbonate: a comparative study of different micro-ct network extraction methods. In: International Symposium of the Society of Core Analysts. Society of Core Analysts.
- Dong, C., Loy, C.C., He, K., Tang, X., 2016a. Image Super-Resolution Using Deep Convolutional Networks. *IEEE Transactions on Pattern Analysis and Machine Intelligence*.
- Dong, C., Loy, C.C., Tang, X., 2016b. Accelerating the super-resolution convolutional neural network. *Arxiv abs/1608.00367*.
- Dosovitskiy, A., Brox, T., 2016. Generating images with perceptual similarity metrics based on deep networks. *Arxiv abs/1602.02644*.
- Erofeev, A., Orlov, D., Ryzhov, A., Koroteev, D., 2019. Prediction of porosity and permeability alteration based on machine learning algorithms. *Transp. Porous Media* 128 (2), 677–700.
- Esteva, M., Hanlon, M., Oct 2015. Digital rocks portal.
- Fandrich, R., Gu, Y., Burrows, D., Moeller, K., 2007. Modern sem-based mineral liberation analysis. *Int. J. Miner. Process.* 84 (1), 310–320. Special Issue to Honor the Late Professor R. Peter King.
- Feng, J., Teng, Q., Li, B., He, X., Chen, H., Li, Y., 2020. An end-to-end three-dimensional reconstruction framework of porous media from a single two-dimensional image based on deep learning. *Comput. Methods Appl. Mech. Eng.* 368, 113043.
- Fenwick, D.H., Blunt, M.J., 1998. Three-dimensional modeling of three phase imbibition and drainage. *Adv. Water Resour.* 21 (2), 121–143.
- Ferrand, L.A., Celia, M.A., 1992. The effect of heterogeneity on the drainage capillary pressure-saturation relation. *Water Resour. Res.* 28 (3), 859–870.
- Flannery, B.P., Deckman, H.W., Robarge, W.G., d'Amico, K.L., 1987. Three-dimensional x-ray microtomography. *Science* 237 (4821), 1439–1444.
- Garfi, G., John, C., Berg, S., Krevor, S., 2019. The sensitivity of estimates of multiphase fluid and solid properties of porous rocks to image processing. *Transp. Porous Media* 12.
- Goodfellow, I.J., Pouget-Abadie, J., Mirza, M., Xu, B., Warde-Farley, D., Ozair, S., Courville, A., Bengio, Y., Jun 2014. Generative Adversarial Networks. *arXiv e-prints p. arXiv:1406.2661*.
- Goodfellow, I., Bengio, Y., Courville, A., 2016. Deep Learning. MIT Press. <http://www.deeplearningbook.org>.
- Gruber, M., Johnson, C., Tang, C., Jensen, M., Yde, L., Hélix-Nielsen, C., 2011. Computational fluid dynamics simulations of flow and concentration polarization in forward osmosis membrane systems. *J. Membr. Sci.* 379 (1), 488–495.
- Gunde, A., Bera, B., Mitra, S., 2010. Investigation of water and co 2 flooding using micro-ct images of Berea sandstone core using finite element simulations. *Energy* 35, 5209–5216.
- Guo, X., Li, W., Iorio, F., 2016. Convolutional neural networks for steady flow approximation. In: *Proceedings of the 22nd ACM SIGKDD International Conference on Knowledge Discovery and Data Mining, KDD '16*, (New York, NY, USA). Association for Computing Machinery, pp. 481–490.
- Hao Chen, W., Yang, Y., Xiao, T., Mayo, S., Dan Wang, Y., Wang, H., 2014. A synchrotronbased local computed tomography combined with data-constrained modelling approach for quantitative analysis of anthracite coal microstructure. *J. Synchrotron Radiat.* 21, 586–593, 05.
- Hao, L., Cheng, P., 2009. Lattice boltzmann simulations of anisotropic permeabilities in carbon paper gas diffusion layers. *J. Power Sources* 186 (1), 104–114.
- Haralick, R.M., Shanmugam, K., Dinstein, I., Nov 1973. Textural features for image classification. In: *IEEE Transactions on Systems, Man, and Cybernetics, SMC-3*, pp. 610–621.
- Hassouna, M.S., Farag, A.A., 2007. Multistencils fast marching methods: A highly accurate solution to the eikonal equation on cartesian domains. *IEEE Trans. Pattern Anal. Mach. Intell.* 29 (9), 1563–1574.
- He, K., Zhang, X., Ren, S., Sun, J., 2015a. Delving Deep into Rectifiers: Surpassing Humanlevel Performance on Imagenet Classification. *Arxiv*.
- He, K., Zhang, X., Ren, S., Sun, J., 2015b. Deep Residual Learning for Image Recognition. *Arxiv*.
- Hennigh, O., 2017. Lat-net: Compressing Lattice Boltzmann Flow Simulations using Deep Neural Networks. *arXiv preprint arXiv:1705.09036*.

- Hilpert, M., Miller, C.T., 2001. Pore-morphology-based simulation of drainage in totally wetting porous media. *Adv. Water Resour.* 24 (3), 243–255. *Pore Scale Modeling*.
- Hong, J., Liu, J., 2020. Rapid estimation of permeability from digital rock using 3d convolutional neural network. *Comput. Geosci.* 24, 1523–1539, 05.
- Iassonov, P., Gebrenegus, T., Tuller, M., 2009. Segmentation of x-ray computed tomography images of porous materials: A crucial step for characterization and quantitative analysis of pore structures. *Water Resour. Res.* 45 (9).
- Ibtihaz, N., Rahman, M.S., 2020. Multiresunet: Rethinking the u-net architecture for multimodal biomedical image segmentation. *Neural Netw.* 121, 74–87.
- Iglauer, S., Paluszny, A., Pentland, C.H., Blunt, M.J., 2011. Residual co2 imaged with x-ray micro-tomography. *Geophys. Res. Lett.* 38 (21).
- Ihle, S., Reichmuth, A., Girardin, S., Han, H., Stauffer, F., Bonnin, A., Stampaoni, M., Pattisapu, K., Vörös, J., Forro, C., 2019. Unsupervised data to content transformation with histogram-matching cycle-consistent generative adversarial networks. *Nat. Machine Intell.* 1, 09.
- Isola, P., Zhu, J.-Y., Zhou, T., Efros, A.A., 2016. Image-to-Image Translation with Conditional Adversarial Networks. Arxiv.
- Janssens, N., Huysmans, M., Rudy, S., 2020. Computed tomography 3d super-resolution with generative adversarial neural networks: Implications on unsaturated and two-phase fluid flow. *Materials* 13, 1–33, 03.
- Jardine, M., Miller, J., Becker, M., 2018. Coupled x-ray computed tomography and grey level co-occurrence matrices as a method for quantification of mineralogy and texture in 3d. *Comput. Geosci.* 111, 105–117.
- Jiang, Z., Van Dijke, M., Sorbie, K.S., Couples, G.D., 2013. Representation of multiscale heterogeneity via multiscale pore networks. *Water Resour. Res.* 49 (9), 5437–5449.
- Jin, X., Cheng, P., Chen, W.-L., Li, H., 2018. Prediction model of velocity field around circular cylinder over various reynolds numbers by fusion convolutional neural networks based on pressure on the cylinder. *Phys. Fluids* 30 (4), 047105.
- Johnson, J., Alahi, A., Li, F., 2016. Perceptual losses for real-time style transfer and super-resolution. Arxiv abs/1603.08155.
- Kamrava, S., Tahmasebi, P., Sahimi, M., 2019a. Enhancing images of shale formations by a hybrid stochastic and deep learning algorithm. *Neural Netw.* 118, 310–320.
- Kamrava, S., Tahmasebi, P., Sahimi, M., 2019b. Linking morphology of porous media to their macroscopic permeability by deep learning. *Transp. Porous Media* 1–22.
- Karimpouli, S., Tahmasebi, P., 2019. Segmentation of digital rock images using deep convolutional autoencoder networks. *Comput. Geosci.* 126, 142–150.
- Keehm, Y., Mukerji, T., Nur, A., 2004. Permeability prediction from thin sections: 3d reconstruction and lattice-boltzmann flow simulation. *Geophys. Res. Lett.* 31 (4).
- Keil, F.J., Rieckmann, C., 1994. Optimization of three-dimensional catalyst pore structures. *Chem. Eng. Sci.* 49 (24), 4811–4822. Part A. Chemical Reaction Engineering: Science and Technology.
- Ketcham, R.A., Carlson, W.D., 2001. Acquisition, optimization and interpretation of x-ray computed tomographic imagery: applications to the geosciences. *Comput. Geosci. vol.* 27 (4), 381–400, 3D reconstruction, modelling & visualization of geological materials.
- Khanafer, K., Cook, K., Marafie, A., 2012. The role of porous media in modeling fluid flow within hollow fiber membranes of the total artificial lung. *J. Porous Media* 15 (2).
- Kim, J., Lee, J.K., Lee, K.M., 2016. Accurate image super-resolution using very deep convolutional networks. In: 2016 IEEE Conference on Computer Vision and Pattern Recognition (CVPR), pp. 1646–1654.
- Kingma, D.P., Ba, J., 2017. Adam: A Method for Stochastic Optimization. Arxiv.
- Krakowska, P., Dohnalik, M., Jarzyna, J., Wawrzyniak-Guz, K., 2016. Computed x-ray microtomography as the useful tool in petrophysics: A case study of tight carbonates madrym formation from Poland. *J. Nat. Gas Sci. Eng.* 31, 67–75.
- Lai, J., Wang, G., Wang, Z., Chen, J., Pang, X., Wang, S., Zhou, Z., He, Z., Qin, Z., Fan, X., 2018. A review on pore structure characterization in tight sandstones. *Earth Sci. Rev.* 177, 436–457.
- LeCun, Y., Boser, B., Denker, J.S., Henderson, D., Howard, R.E., Hubbard, W., Jackel, L. D., 1989. Backpropagation applied to handwritten zip code recognition. *Neural Comput.* 1 (4), 541–551.
- Ledig, C., Theis, L., Huszar, F., Caballero, J., Cunningham, A., Acosta, A., Aitken, A., Tejani, A., Totz, J., Wang, Z., Shi, W., 2017. Photo-Realistic Single Image Super-Resolution Using a Generative Adversarial Network. Arxiv.
- Leu, L., Berg, S., Enzmann, F., Armstrong, R., Kersten, M., 2014. Fast x-ray microtomography of multiphase flow in Berea sandstone: A sensitivity study on image processing. *Transp. Porous Media* 105, 09.
- Li, Z., Teng, Q., He, X., Yue, G., Wang, Z., 2017. Sparse representation-based volumetric super-resolution algorithm for 3d ct images of reservoir rocks. *J. Appl. Geophys.* 144, 69–77.
- Liao, Y.-Y., Tsui, P.-H., Li, C.-H., Chang, K.-J., Kuo, W.-H., Chang, C.-C., Yeh, C.-K., 2011. Classification of scattering media within benign and malignant breast tumors based on ultrasound texture-feature-based and nakagami-parameter images. *Med. Phys.* 38 (4), 2198–2207.
- Lim, B., Son, S., Kim, H., Nah, S., Lee, K.M., 2017. Enhanced deep residual networks for single image super-resolution. In: 2017 IEEE Conference on Computer Vision and Pattern Recognition Workshops (CVPRW), pp. 1132–1140.
- Liu, M., Mostaghimi, P., 2017a. Characterisation of reactive transport in pore-scale correlated porous media. *Chem. Eng. Sci.* 173, 121–130.
- Liu, M., Mostaghimi, P., 2017b. Pore-scale simulation of dissolution-induced variations in rock mechanical properties. *Int. J. Heat Mass Transf.* 111, 842–851.
- Liu, Z., Herring, A., Arns, C., Berg, S., Armstrong, R.T., 2017a. Pore-scale characterization of two-phase flow using integral geometry. *Transp. Porous Media* 118 (1), 99–117.
- Liu, M., Shabaninejad, M., Mostaghimi, P., 2017b. Impact of mineralogical heterogeneity on reactive transport modelling. *Comput. Geosci.* 104, 12–19.
- Liu, M., Shabaninejad, M., Mostaghimi, P., 2018. Predictions of permeability, surface area and average dissolution rate during reactive transport in multi-mineral rocks. *J. Pet. Sci. Eng.* 170, 130–138.
- Madero Orozco, H., Vergara Villegas, O.O., Cruz Sánchez, V.G., Domínguez, H.D.J., Ochoa, Alfaro, M.D.J. Nandayapa, Feb 2015. Automated system for lung nodules classification based on wavelet feature descriptor and support vector machine. *Biomed. Eng. Online* 14 (9).
- Makaju, S., Prasad, P., Alsadoon, A., Singh, A., Elchouemi, A., 2018. Lung cancer detection using ct scan images. *Procedia Comp. Sci.* 125, 107–114. The 6th International Conference on Smart Computing and Communications.
- Manwart, C., Aaltosalmi, U., Koponen, A., Hilfer, R., Timonen, J., 2002. Lattice-boltzmann and finite-difference simulations for the permeability for three-dimensional porous media. *Phys. Rev. E* 66 (1), 016702.
- McClure, J., Prins, J., Miller, C., 2014. A novel heterogeneous algorithm to simulate multiphase flow in porous media on multicore cpu-gpu systems. *Comput. Phys. Commun.* 185 (7), 1865–1874.
- Menke, H., Reynolds, C., Andrew, M., Pereira Nunes, J., Bijeljic, B., Blunt, M., 2018. 4d multi-scale imaging of reactive flow in carbonates: Assessing the impact of heterogeneity on dissolution regimes using streamlines at multiple length scales. *Chem. Geol.* 481, 27–37.
- Mosser, L., Dubrule, O., Blunt, M.J., 2017a. Reconstruction of three-dimensional porous media using generative adversarial neural networks. *Phys. Rev. E* 96, 043309. Oct.
- Mosser, L., Dubrule, O., Blunt, M., 2017b. Stochastic reconstruction of an oolitic limestone by generative adversarial networks. *Transp. Porous Media* 12.
- Mostaghimi, P., Mahani, H., et al., 2010. A quantitative and qualitative comparison of coarsegrid-generation techniques for modeling fluid displacement in heterogeneous porous media. *SPE Reserv. Eval. Eng.* 13 (01), 24–36.
- Mostaghimi, P., Bijeljic, B., Blunt, M., et al., 2012. Simulation of flow and dispersion on pore-space images. *SPE J.* 17 (04), 1–131.
- Mostaghimi, P., Blunt, M.J., Bijeljic, B., 2013. Computations of absolute permeability on micro-ct images. *Math. Geosci.* 45 (1), 103–125.
- Mostaghimi, P., Percival, J., Pavlidis, D., Ferrier, R., Gomes, J., Gorman, G., Jackson, M., Neethling, S., Pain, C., 2015. Anisotropic mesh adaptivity and control volume finite element methods for numerical simulation of multiphase flow in porous media. *Math. Geosci.* 47, 417–440, 05.
- Mostaghimi, P., Liu, M., Arns, C.H., Nov 2016. Numerical simulation of reactive transport on micro-ct images. *Math. Geosci.* 48, 963–983.
- Niu, Y., Mostaghimi, P., Shabaninejad, M., Swietojanski, P., Armstrong, R.T., 2019. Digital rock segmentation for petrophysical analysis with reduced user bias using convolutional neural networks. *Water Resour. Res.* 56 (2), 1–11.
- Niu, Y., Wang, Y.D., Mostaghimi, P., Swietojanski, P., Armstrong, R.T., 2020. An innovative application of generative adversarial networks for physically accurate rock images with an unprecedented field of view. *Geophys. Res. Lett.* 47 (23).
- Odena, A., Dumoulin, V., Olah, C., 2016. Deconvolution and Checkerboard Artifacts. Distill.
- Okabe, H., Blunt, M.J., 2007. Pore space reconstruction of vuggy carbonates using microtomography and multiple-point statistics. *Water Resour. Res.* 43 (12).
- Pan, C., Hilpert, M., Miller, C., 2004. Lattice-boltzmann simulation of two-phase flow in porous media. *Water Resour. Res.* 40 (1).
- Rabbani, A., Babaei, M., 2019. Hybrid pore-network and lattice-boltzmann permeability modelling accelerated by machine learning. *Adv. Water Resour.* 126, 116–128.
- Rabbani, A., Mostaghimi, P., Armstrong, R.T., 2019. Pore network extraction using geometrical domain decomposition. *Adv. Water Resour.* 123, 70–83.
- Rabbani, A., Babaei, M., Shams, R., Wang, Y.D., Chung, T., 2020. Deepore: A deep learning workflow for rapid and comprehensive characterization of porous materials. *Adv. Water Resour.* 146, 103787.
- Raeini, A.Q., Blunt, M.J., Bijeljic, B., 2012. Modelling two-phase flow in porous media at the pore scale using the volume-of-fluid method. *J. Comput. Phys.* 231 (17), 5653–5668.
- Raeini, A.Q., Blunt, M.J., Bijeljic, B., 2014. Direct simulations of two-phase flow on micro-ct images of porous media and upscaling of pore-scale forces. *Adv. Water Resour.* 74, 116–126.
- Ramstad, T., Ören, P.-E., Bakke, S., et al., 2010. Simulation of two-phase flow in reservoir rocks using a lattice boltzmann method. *SPE J.* 15 (04), 917–927.
- Ren, X., Guo, Z., Ning, F., Ma, S., 2020. Permeability of hydrate-bearing sediments. *Earth Sci. Rev.* 202, 103100.
- Ribeiro, M.D., Rehman, A., Ahmed, S., Dengel, A., 2020. Deepcfd: Efficient Steady-State Laminar Flow Approximation with Deep Convolutional Neural Networks. Arxiv.
- Richesson, S., Sahimi, M., 2019. Hertz-mindlin theory of contacting grains and the effective-medium approximation for the permeability of deforming porous media. *Geophys. Res. Lett.* 46 (14), 8039–8045.
- Ronneberger, O., Fischer, P., Brox, T., 2015. U-Net: Convolutional Networks for Biomedical Image Segmentation. Arxiv.
- Santos, J.E., Xu, D., Jo, H., Landry, C.J., Prodanović, M., Pyrcz, M.J., 2020. Poreflownet: A 3d convolutional neural network to predict fluid flow through porous media. *Adv. Water Resour.* 138, 103539.
- Saxena, N., Hofmann, R., Alpak, F.O., Berg, S., Dietderich, J., Agarwal, U., Tandon, K., Hunter, S., Freeman, J., Wilson, O.B., 2017. References and benchmarks for pore-scale flow simulated using micro-ct images of porous media and digital rocks. *Adv. Water Resour.* 109, 211–235.
- Schlüter, S., Sheppard, A., Brown, K., Wildenschild, D., 2014. Image processing of multiphase images obtained via x-ray microtomography: a review. *Water Resour. Res.* 50 (4), 3615–3639.
- Sezgin, M., Sankur, B., 2004. Survey over image thresholding techniques and quantitative performance evaluation. *J. Elect. Imag.* 13, 146–168.

- Shabro, V., Torres-Verdín, C., Javadpour, F., Sepehrnoori, K., 2012. Finite-difference approximation for fluid-flow simulation and calculation of permeability in porous media. *Transp. Porous Media* 94 (3), 775–793.
- Shi, W., Caballero, J., Huszár, F., Totz, J., Aitken, A.P., Bishop, R., Rueckert, D., Wang, Z., 2016. Real-time single image and video super-resolution using an efficient sub-pixel convolutional neural network. Arxiv abs/1609.05158.
- Singh, A., Armstrong, R.T., Regenauer-Lieb, K., Mostaghimi, P., 2019. Rock characterization using gray-level co-occurrence matrix: an objective perspective of digital rock statistics. *Water Resour. Res.* 55 (3), 1912–1927.
- Singh, A., Regenauer-Lieb, K., Walsh, S.D.C., Armstrong, R.T., van Griethuysen, J.J.M., Mostaghimi, P., 2020. On representative elementary volumes of grayscale micro-ct images of porous media. *Geophys. Res. Lett.* 47 (15).
- Sivaramakrishna, R., Powell, K.A., Lieber, M.L., Chilcote, W.A., Shekhar, R., 2002. Texture analysis of lesions in breast ultrasound images. *Comput. Med. Imaging Graph.* 26 (5), 303–307.
- Smith, W.E., Barrett, H.H., Paxman, R.G., Apr 1983. Reconstruction of objects from coded images by simulated annealing. *Opt. Lett.* 8, 199–201.
- Soulaine, C., Gjetvaj, F., Garing, C., Roman, S., Russian, A., Gouze, P., Tchelépi, H.A., 2016. The impact of sub-resolution porosity of x-ray microtomography images on the permeability. *Transp. Porous Media* 113 (1), 227–243.
- Spaid, M.A., Phelan Jr., F.R., 1997. Lattice boltzmann methods for modeling microscale flow in fibrous porous media. *Phys. Fluids* 9 (9), 2468–2474.
- Stewart, M.L., Ward, A.L., Rector, D.R., 2006. A study of pore geometry effects on anisotropy in hydraulic permeability using the lattice-boltzmann method. *Adv. Water Resour.* 29 (9), 1328–1340.
- Sudakov, O., Burnaev, E., Koroteev, D., 2019. Driving digital rock towards machine learning: predicting permeability with gradient boosting and deep neural networks. *Comput. Geosci.* 127, 91–98.
- Taha, A.A., Hanbury, A., 2015. Metrics for evaluating 3d medical image segmentation: analysis, selection, and tool. *BMC Med. Imaging* 15.
- Tahmasebi, P., Kamrava, S., Bai, T., Sahimi, M., 2020. Machine learning in geo- and environmental sciences: from small to large scale. *Adv. Water Resour.* 142, 103619.
- Tembely, M., Alsumaiti, A., Alameri, W., 2020. A deep learning perspective on predicting permeability in porous media from network modeling to direct simulation. *Comput. Geosci.* 05.
- Tian, J., Qi, C., Sun, Y., Yaseen, Z., Pham, B., 2020. Permeability prediction of porous media using a combination of computational fluid dynamics and hybrid machine learning methods. *Eng. Comput.* 03.
- Torskaya, T., Shabro, V., Torres-Verdín, C., Salazar-Tio, R., Revil, A., 2014. Grain shape effects on permeability, formation factor, and capillary pressure from pore-scale modeling. *Transp. Porous Media* 102 (1), 71–90.
- Varfolomeev, I., Yakimchuk, I., Safonov, I., 2019. An application of deep neural networks for segmentation of microtomographic images of rock samples. *Computers* 8 (4).
- Wang, Y., Wang, L., Wang, H., Li, P., 2016. End-to-end image super-resolution via deep and shallow convolutional networks. Arxiv abs/1607.07680.
- Wang, X., Yu, K., Wu, S., Gu, J., Liu, Y., Dong, C., Loy, C.C., Qiao, Y., Tang, X., 2018. ESRGAN: enhanced super-resolution generative adversarial networks. Arxiv abs/1809.00219.
- Wang, Y.D., Armstrong, R.T., Mostaghimi, P., 2019a. Enhancing resolution of digital rock images with super resolution convolutional neural networks. *J. Pet. Sci. Eng.* 182, 106261.
- Wang, Y.D., Chung, T., Armstrong, R.T., McClure, J.E., Mostaghimi, P., 2019b. Computations of permeability of large rock images by dual grid domain decomposition. *Adv. Water Resour.* 126, 1–14.
- Wang, Y.D., Mostaghimi, P., Armstrong, R., 2019c. A Diverse Super Resolution Dataset of Sandstone, Carbonate, and Coal (Deeprock-Sr).
- Wang, Y.D., Mostaghimi, P., Armstrong, R., 2019d. A Super Resolution Dataset of Digital Rocks (drsrd1): Sandstone and Carbonate.
- Wang, Y.D., Mostaghimi, P., Armstrong, R., 2019e. A Diverse Super Resolution Dataset of Sandstone, Carbonate, and Coal (Deeprock-Sr). Digital Rocks Portal.
- Wang, Y.D., Shabaninejad, M., Armstrong, R.T., Mostaghimi, P., 2021. Physical Accuracy of Deep Neural Networks for 2d and 3d Multi-Mineral Segmentation of Rock Micro-Ct Images. *Applied Soft Computing*.
- Wang, Y., Teng, Q., He, X., Feng, J., Zhang, T., 2019f. Ct-image of rock samples super resolution using 3d convolutional neural network. *Comput. Geosci.* 133, 104314.
- Wang, Y.D., Armstrong, R.T., Mostaghimi, P., 2020a. Boosting resolution and recovering texture of 2d and 3d micro-ct images with deep learning. *Water Resour. Res.* 56 (1), 1–21.
- Wang, Y., Chung, T., Armstrong, R., McClure, J., Ramstad, T., Mostaghimi, P., 2020b. Accelerated computation of relative permeability by coupled morphological and direct multiphase flow simulation. *J. Comput. Phys.* 401, 108966.
- Wang, Y.D., Chung, T., Armstrong, R.T., Mostaghimi, P., 2020c. Mi-lbm: Machine Learning Aided Flow Simulation in Porous Media. Arxiv.
- Wu, J., Yin, X., Xiao, H., 2018. Seeing permeability from images: fast prediction with convolutional neural networks. *Sci. Bull.* 63 (18), 1215–1222.
- Xu, P., Yu, B., 2008. Developing a new form of permeability and kozeny–carman constant for homogeneous porous media by means of fractal geometry. *Adv. Water Resour.* 31 (1), 74–81.
- Yang, J., 2013. Multi-Scale Simulation of Multiphase Multi-Component Flow in Porous Media Using the Lattice Boltzmann Method. Thesis, Imperial College London.
- Yang, X., Tridandapani, S., Beitzler, J.J., Yu, D.S., Yoshida, E.J., Curran, W.J., Liu, T., 2012. Ultrasound glcm texture analysis of radiation-induced parotid-gland injury in head-and-neck cancer radiotherapy: an in vivo study of late toxicity. *Med. Phys.* 39 (9), 5732–5739.
- Yang, W., Zhang, X., Tian, Y., Wang, W., Xue, J.-H., Liao, Q., Dec 2019. Deep learning for single image super-resolution: A brief review. *IEEE Trans. Multimedia* 21, 3106–3121.
- Yi, Z., Lin, M., Jiang, W., Zhang, Z., Li, H., Gao, J., 2017. Pore network extraction from pore space images of various porous media systems. *Water Resour. Res.* 53 (4), 3424–3445.
- You, C., Li, G., Zhang, Y., Zhang, X., Shan, H., Ju, S., Zhao, Z., Zhang, Z., Cong, W., Vannier, M.W., Saha, P.K., Wang, G., 2018. CT Super-Resolution Gan Constrained by the Identical, Residual, and Cycle Learning Ensemble(GAN-CIRCLE). arXiv e-prints, p. arXiv:1808.04256, Aug.
- Yu, J., Fan, Y., Yang, J., Xu, N., Wang, Z., Wang, X., Huang, T., 2018. Wide activation for efficient and accurate image super-resolution. Arxiv, abs/1808.08718.
- Yuan, Y., Liu, S., Zhang, J., Zhang, Y., Dong, C., Lin, L., 2018. Unsupervised image superresolution using cycle-in-cycle generative adversarial networks. In: 2018 IEEE/CVF Conference on Computer Vision and Pattern Recognition Workshops (CVPRW), pp. 814–81409.
- Zhang, K., Gu, S., Timofte, R., Shang, T., Dai, Q., Zhu, S., Yang, T., Guo, Y., Jo, Y., Yang, S., Kim, S.J., Zha, L., Jiang, J., Gao, X., Lu, W., Liu, J., Yoon, K., Jeon, T., Akita, K., Ooba, T., Ukita, N., Luo, Z., Yao, Y., Xu, Z., He, D., Wu, W., Ding, Y., Li, C., Li, F., Wen, S., Li, J., Yang, F., Yang, H., Fu, J., Kim, B.H., Baek, J., Ye, J.C., Fan, Y., Huang, T.S., Lee, J., Lee, B., Min, J., Kim, G., Lee, K., Park, J., Mykhailych, M., Zhong, H., Shi, Y., Yang, X., Yang, Z., Lin, L., Zhao, T., Peng, J., Wang, H., Jin, Z., Wu, J., Chen, Y., Shang, C., Zhang, H., Min, J., Hirshikesh, P.S., Puthussery, D., Jiji, C.V., 2020. Ntire 2020 challenge on perceptual extreme super-resolution: Methods and results. In: 2020 IEEE/CVF Conference on Computer Vision and Pattern Recognition Workshops (CVPRW), pp. 2045–2057.
- Zhao, J., Qin, F., Derome, D., Carmeliet, J., 2020. Simulation of quasi-static drainage displacement in porous media on pore-scale: Coupling lattice boltzmann method and pore network model. *J. Hydrol.* 588, 125080.
- Zhu, J., Park, T., Isola, P., Efros, A.A., 2017. Unpaired image-to-image translation using cycle-consistent adversarial networks. Arxiv vol. abs/1703.10593.